UNIVERSITY OF SÃO PAULO
SÃO CARLOS SCHOOL OF ENGINEERING
DEPARTMENT OF MATERIALS ENGINEERING

JACQUELINE PEREIRA ROCHA

Mechanical properties of polyamide 12 parts produced by Multi Jet Fusion 3D printing technology

Bachelor's Thesis

São Carlos
2019

JACQUELINE PEREIRA ROCHA

Mechanical properties of polyamide 12 parts produced by Multi Jet Fusion 3D printing technology

Bachelor's thesis shown to the program of Materials and Manufacturing engineering, from São Carlos School of Engineering, University of São Paulo, as a way of obtaining the title of Materials and Manufacturing engineer.
Advisor: Doctor Vera Lúcia Arantes.

São Carlos
2019

Ficha catalográfica elaborada pela Biblioteca Prof. Dr. Sérgio Rodrigues Fontes da EESC/USP com os dados inseridos pelo(a) autor(a).

P672m

Pereira Rocha, Jacqueline
Mechanical properties of polyamide 12 parts produced by Multi Jet Fusion 3D printing technology / Jacqueline Pereira Rocha; orientadora Vera Lúcia Arantes. São Carlos, 2019.

Monografia (Graduação em Engenharia de Materiais e Manufatura) -- Escola de Engenharia de São Carlos da Universidade de São Paulo, 2019.

1. 3D printing. 2. Multi Jet Fusion. 3. Mechanical Properties. 4. Printing orientation. 5. Lattice structures. I. Título.

Eduardo Graziosi Silva - CRB - 8/8907

FOLHA DE APROVAÇÃO

Candidato: Jacqueline Pereira Rocha
Título do TCC: Mechanical properties of polyamide 12 parts produced by Multi Jet Fusion 3D printing technology
Data de defesa: 13/11/2019

Comissão Julgadora	**Resultado**
Professor Doutor Vera Lúcia Arantes (orientador)	Aprovada
Instituição: EESC - SMM	
Professor Doutor Iris Bento da Silva	APROVADA
Instituição: EESC - SEM	
Professor Doutor Márcia Cristina Branciforti	Aprovada
Instituição: EESC - SMM	

Presidente da Banca: **Professor Doutor Vera Lúcia Arantes**

Vera Lúcia Arantes
(assinatura)

I dedicate this work to the memory of Pingo, and the best 17 years of a dog's company anyone could have hoped for.

ACKNOWLEDGMENTS

I would like to thank the Laboratory of prototyping technologies and processes, from Technical University of Liberec, in special Jiří Šafka, Michal Ackermann, Filip Véle and Jakub Macháček. As well as the UNIGOU Academic Internship Program, offered by the INCBAC Institute. Without them this bachelor's thesis would not have been possible, I greatly appreciate all the help.

In the same manner, to thank professors in Sao Carlos School of Engineering for being an important part in my academic education, and the University of São Paulo for providing my bachelor's degree. My advisor Vera Lúcia Arantes for all the guide and support, and professors Iris Bento da Silva and Márcia Cristina Branciforti for evaluating and helping me in the end of the process. Likewise, to my friends made in university Jônatas Viscaino, Vinicius Ballista Galetti, and Vitória Dias.

As well as to all my family members. My brother and my sister, who always help me when I need it. Especially to my husband for all these 11 years of support and companionship. Also, to the dogs that have been in our life for making everything lighter and happier.

Finally, to all friends and anyone who helped me on my way in life.

Thank you very much.

ABSTRACT

Rocha, J. P. **Mechanical properties of polyamide 12 parts produced by Multi Jet Fusion 3D printing technology.** 2019. 115 f. Monografia (Trabalho de Conclusão de Curso) - Escola de Engenharia de São Carlos, Universidade de São Paulo, São Carlos, 2019.

Additive manufacturing used to be applied mainly to prototyping, however recent technologies have been increasingly used in product manufacturing. This can be explained by the fact that 3D printing allows production of parts with complex geometry, impossible to make otherwise. Also, with excellent quality and performance. One of these technologies is the Multi Jet Fusion, a powder bed fusion process, that has made possible to obtain a small series production of final parts, besides from functional prototypes. Parts produced with this method are considered strong, with fine detail and dimensional accuracy, and obtained at a low cost. In this work, this method was used to produce polyamide 12 specimens in order to investigate its mechanical properties. The first aspect analysed about this 3D printing method was the influence of the printing orientation in tensile properties. Hence, 150 regular tensile test specimens were printed and positioned in fifteen printing orientations. Specimens of different printing orientations did not have outstanding increase in tensile strength, but presented varied results for strain at break. The printing orientation with the highest result for maximum stress also had high strain values. The second aspect analysed was the viability and mechanical performance of lightweight parts made with lattice structures. A new geometry for tensile test specimen was developed, which enable it to be filled with three different geometry of lattice structures, which were named Cross, BCC and Octet-truss. These structures had four possible percentages of volume occupied by material, thus allowing the comparison of their behaviour for each volume. They were printed in a few orientations, and results were obtained for maximal force and displacement at break. Generally, parts can withstand higher values of force, the higher the volume is filled with material.

Keywords: 3D printing. Multi Jet Fusion. Mechanical Properties. Printing orientation. Lattice structures.

Resumo

Rocha, J. P. **Propriedades mecânicas de peças em poliamida 12 produzidas pela tecnologia de impressão 3D Multi Jet Fusion.** 2019. 115 f. Monografia (Trabalho de Conclusão de Curso) - Escola de Engenharia de São Carlos, Universidade de São Paulo, São Carlos, 2019.

A manufatura aditiva era aplicada principalmente à prototipagem rápida, porém tecnologias recentes são cada vez mais usadas na manufatura de peças finais. Isso deve-se ao fato de que a impressão 3D permite a produção de peças com geometrias complexas, impossíveis de serem obtidas de outra forma. Além disso, elas têm excelente qualidade e desempenho. Dentre essas, pode-se citar *Multi Jet Fusion*, é um processo que usa camadas de material em pó, e possibilita uma pequena produção em série, além de protótipos funcionais. As peças produzidas por esse método são resistentes, com ótimo detalhamento e precisão dimensional, e obtidas a um baixo custo. Neste trabalho, este método foi utilizado para produzir corpos de prova feito em poliamida 12, a fim de investigar suas propriedades mecânicas. O primeiro aspecto analisado foi a influência da orientação de impressão nas propriedades mecânicas. Assim, 150 amostras de teste de tração foram impressas e posicionadas em quinze orientações. As diferentes orientações não apresentaram um aumento notável quanto a resistência à tração, mas sim resultados variados para deformação na ruptura. A orientação de impressão com o máximo resultado para tensão também apresentou alto valor de deformação. O segundo aspecto analisado foi o desempenho mecânico de peças leves feitas com estruturas *lattice*. Uma nova geometria de corpo de prova foi desenvolvida, em que ele foi preenchido com três diferentes de estruturas, denominadas *Cross*, *BCC* e *Octet-truss*. Eles receberam quatro possíveis porcentagens de volume ocupado por material, permitindo a comparação de resultados em cada volume. Eles foram impressos em algumas orientações e os resultados obtidos foram a força máxima e o deslocamento na ruptura. Geralmente, as peças podem suportar valores altos de força, quanto maior é o volume preenchido com material.

Palavras-chave: Impressão 3D. Multi Jet Fusion. Propriedades mecânicas. Orientação de impressão. Estruturas do tipo lattice.

LIST OF FIGURES

Figure 1- Schematic of MJF principles. 25
Figure 2 - The window guide rail for BMW i8 Roadster. 26
Figure 3 - The bearing cage made with PA11 and MJF technology. 27
Figure 4 - Example of layer orientation on parts printed horizontally and vertically. .. 28
Figure 5 - PA12 monomer structure. 30
Figure 6 - The engineering stress-strain for an aluminium alloy. 34
Figure 7 - The stress-strain curve for 6,6-nylon. 36
Figure 8 - HP Jet Fusion 4200 3D Printer. 37
Figure 9 - HP Jet Fusion 4200 3D Processing Station with Fast Cooling. 39
Figure 10 - HP Jet Fusion 3D Built Unit. 40
Figure 11 - Solid tensile test specimen. 41
Figure 12 - Illustration for A, B and C specimens directions. 42
Figure 13 - Illustration of rotations for D and E specimens. 43
Figure 14 - Illustration of the defined fifteen printing orientations. 44
Figure 15 - Solid specimens' nomenclature. 45
Figure 16 - Cross structure with 10% of occupied volume. 46
Figure 17 - BCC structure with 25% of occupied volume. 47
Figure 18 - Octet structure with 50% of occupied volume. 48
Figure 19 - Lattice structure tensile test specimen. 49
Figure 20 - Illustration of orientations and rotations for lattice structures specimens. 50
Figure 21 - Tensile test specimen with BCC structure positioned in testing machine 53
Figure 22 - Printed tensile test specimens. 54
Figure 23 - Solid specimens after tensile test. 54
Figure 24 - E1V2 specimens after tensile testing. 60
Figure 25 - Stress-strain curves for A1V1 specimens. 63
Figure 26 - A1V1 specimens after tensile testing. 64
Figure 27 - Stress-strain curves for D3V2 specimens. 65
Figure 28 - D3V2 specimens after tensile testing. 66
Figure 29 - Tensile test specimens with lattice structures. 67
Figure 30 - Tensile specimen after test. 68

LIST OF TABLES

Table 1 - PA12 properties processed by traditional methods. 30
Table 2 - PA12 properties from supplier. 41
Table 3 - Cylindrical rod diameters and volumes of Cross structure. 46
Table 4 - Cylindrical rod diameters and volumes of BCC structure. 47
Table 5 - Cylindrical rod diameters and volumes of Octet structure. 48
Table 6 - Average values for maximum stress, strain at break, modulus of elasticity, yield strength, and ductility. 55
Table 7 - Comparison of resulting properties values with literature. 62

LIST OF EQUATIONS

Equation 1 - Equation for modulus of elasticity.. 51

LIST OF GRAPHS

Graph 1 - Average maximum stress values. 56
Graph 2 - Average strain at break values. 57
Graph 3 - Average values for modulus of elasticity. 59
Graph 4 - Average yield strength values. 61
Graph 5 - Average values for ductility. 62
Graph 6 - Force and displacement values for Cross 10% specimens. 69
Graph 7 - Force and displacement values for Cross 25% specimens. 70
Graph 8 - Force and displacement values for Cross 50% specimens. 71
Graph 9 - Force and displacement values for Cross 70% specimens. 72
Graph 10 - Force and displacement values for BCC 10% specimens. 73
Graph 11 - Force and displacement values for BCC 25% specimens. 74
Graph 12 - Force and displacement values for BCC 50% specimens. 75
Graph 13 - Force and displacement values for BCC 70% specimens. 76
Graph 14 - Force and displacement values for Octet 25% specimens. 77
Graph 15 - Force and displacement values for Octet 50% specimens. 78
Graph 16 - Comparison of structures at 25% and A0° orientation. 79
Graph 17 - Comparison of structures at 50% and A0° orientation. 80

LIST OF ACRONYMS

FDM	Fusion deposition modeling
MJF	Multi jet fusion
Octet	Octet-truss structure
PA12	Polyamide 12
PBF	Powder bed fusion
SLM	Selective laser melting
SLS	Selective laser sintering
T_g	Glass-transition temperature

Table of contents

1. Introduction 22
   1.1 Objectives 22
2. Literature review 23
   2.1 Additive manufacturing 23
      2.1.1 Multi Jet Fusion 24
      2.1.2 Printing orientations 27
   2.2 Polyamide 12 29
   2.3 Lattice structures 31
   2.4 Mechanical testing 33
      2.4.1 Tensile test 33
3. Materials and methods 37
   3.1 HP Jet Fusion 4200 3D 37
   3.2 Materials 40
   3.3 Printing of solid tensile test specimens 41
   3.4 Printing of lattice structures tensile test specimens 45
   3.4 Tensile test 51
      3.4.1 Solid specimens 51
      3.4.2 Lattice structures specimens 52
4. Results and discussions 53
   4.1 Printing orientation of solid parts 53
   4.2 Lattice structures 66
5. Conclusions 81

References 83

Appendix 86
   Appendix A - Lattice structures 86
   Appendix B - Engineering stress-strain curves for solid parts 87
   Appendix C - Force-displacement curves for lattice structure parts 101

1. Introduction

Additive manufacturing used to be applied mostly for prototyping. However, recent developed technologies have been increasingly used for final parts production. One of these newer technologies is the Multi Jet Fusion, developed by HP company. This technology is based in the powder bed fusion process, that produces primarily parts made of polyamide 12 powder. These produced parts have outstanding mechanical properties, comparable to products obtained by traditional manufacturing methods such as injection molding. In this manner, this characteristic can emphasize the relevance of this subject, and the importance of a better understanding of this printing process.

In order to analyse the influence of the printing orientation in the resulting mechanical properties of parts, regular solid tensile test specimens were printed in fifteen orientations, and submitted to tensile testing. It was also investigated specimens filled with lattice structures, through tensile testing, with the purpose to compare the mechanical behaviour of different structures.

The tensile test specimens, both solid and filled with lattice structures, were developed together with the Laboratory of prototype technologies and processes, from Technical University of Liberec, situated in the Czech Republic. They were responsible for printing and testing all specimens related to this study.

1.1 Objectives

The present research intents to evaluate mechanical properties of polyamide 12 specimens produced by Multi Jet Fusion 3D printing technology. Accordingly, properties were measured through tensile test specimens positioned in fifteen specifics printing orientations, in order to evaluate the influence of orientation used to print solid parts. In this work, it was also analysed the mechanical performance of lightweight parts made with lattice structures, by testing tensile specimens filled with three different structure geometries. Hence, it was sought to obtain the performance comparison between these structures.

2. Literature review

2.1 Additive manufacturing

In 2013, Mckinsey report's defined 3D printing, or additive manufacturing, as having potential for being a disruptive technology, one that could impact all steps of product manufacturing. This is possible given its advantages over traditional methods, such as fewer manufacturing steps, reduced material waste, and the creation of objects that would be hard or impossible to produce otherwise. Therefore, it is possible to achieve a complex, low volume and highly customizable products. They mention examples like in the case of metal manufacturing, where it is possible to obtain lightweight objects with internal structures as the honeycomb, whereas bioprinting allows organs with blood vessels to be created. Nonetheless, the observed disadvantages among the different processes, found at that time, could be resumed to relative slow building speed, restricted object size, detail or resolution, high material cost, and sometimes limited product strength (MCKINSEY GLOBAL INSTITUTE, 2013).

New technologies have been dealing with overcoming these limitations, what could make additive manufacturing a main manufacturing method. According to the Wohlers Report of 2018, in the year of 2017 additive manufacturing had a remarkable 21% growth, and its industry exceeded 7.3 billion, regarding all products and services worldwide. However, it did not consider internal investments that have been made in research and development for additive manufacturing, from hundreds of companies such as Airbus, Ford, and Toyota (FORBES, 2018).

According to ASTM International additive manufacturing can be defined as a process of joining materials in a layer by layer manner, in order to create products originated by a 3D model. As such, is opposed to subtractive methods like machining. It also established a classification for additive manufacturing processes that can be separated into seven categories known as binder jetting, directed energy deposition, material extrusion, material jetting, powder bed fusion, sheet lamination, and vat photopolymerization (ASTM F2792-12a, 2012). 3D printing products are made from a variety of materials such as polymers, metals, ceramics, glasses, papers, and even living cells. Normally they can be used as powders, filaments, liquids, and sheets (MCKINSEY GLOBAL INSTITUTE, 2013).

Powder bed fusion (PBF) is a category that uses materials in the form of powder, and can be mentioned as one of the first commercialized additive manufacturing processes. The first commercial technology operating with this process was Selective Laser Sintering (SLS), which was developed by The University of Texas. Even though there were since developed different technologies from PBF method, they all share common characteristics, such as at least one type of thermal source used for fusion of powder particles; a powder fusion controlling technique that is applied to a determined specific region on each layer created; and procedures designated for the adding and smoothing of these powder layers. The most common type of thermal source is still laser, which is used on SLS technology. Other sources like electron beam melting or infrared light demand a different machine configuration. Most types of materials are used, in this case polymers, metals, ceramics and composites. One of the advantages of this process is the lack of need for support structures, since that role is done by all deposited powder surrounding parts in each layer (GIBSON; ROSEN; STUCKER, 2015).

PBF technologies have potential for direct manufacturing method of end-use products, and have been gradually more used, since its materials properties are similar to ones in parts manufactured by traditional methods (GIBSON; ROSEN; STUCKER, 2015).

2.1.1 Multi Jet Fusion

Multi jet fusion (MJF) is a new technology developed by HP, made available at the market in 2016. The first 3D printer models were HP Jet Fusion 3D 3200 and 4200, which allowed production of only black colored products (3DPRINTING, 2016). In 2018, they launched two models capable of printing in full color (JET FUSION 500/300 SERIES, 2019). This technology promised at its launch a printing time ten times faster than the average for fused deposition modeling (FDM) and SLS technologies, and at the lowest cost. The two models are intended to industrial prototyping and final part production, however the HP Jet Fusion 3D 4200 is designed for environments that aim to produce more products per week than the first model, given its higher building speed (HP JET FUSION 3D PRINTING SOLUTIONS, 2017). In this process a powder bed of polyamide is used, where in each layer a fusing and detailing agents are also deposited. The thermal source used is infrared lamps, that apply the necessary heat for fusing target particles together, creating pieces (MOLITCH-HOU, 2018).

Figure 1- Schematic of MJF principles.

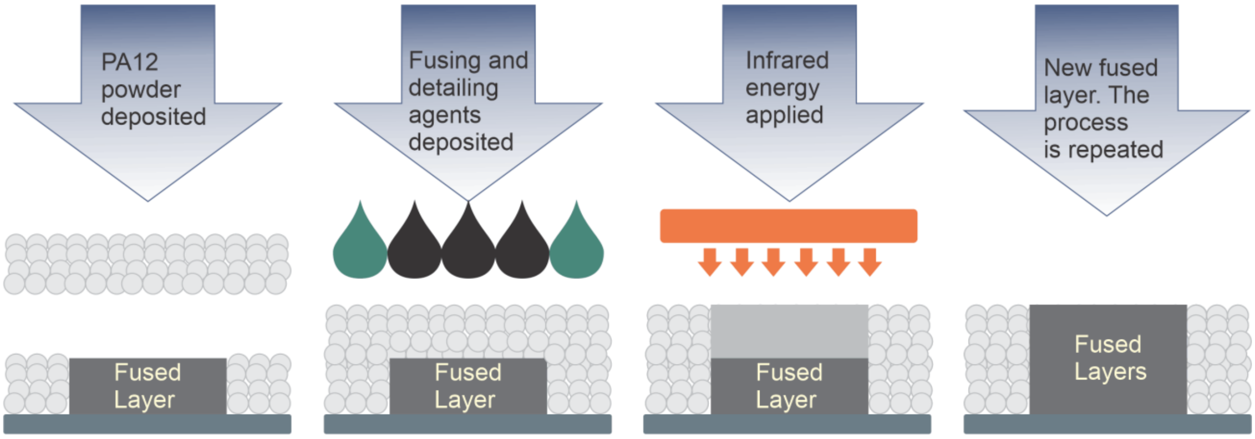

Source: adapted from O'Connor, Dickson, and Dowling (2018).

The beginning of this process is given by deposition of polyamide powder layer onto the building platform. The fusing agent is then applied selectively to this layer, mixed only with powder intended to compose products. In the case of printers with just black color available, the fusing agent is a black ink with a high carbon black content capable of absorbing infrared light. The detailing agent is applied only around contours of products, and is composed mainly of water, which can lower the temperature to avoid fusion of particles not included in products designs, and help improve their resolution (O'CONNOR; DICKSON; DOWLING, 2018; RIEDELBAUCH; RIETZEL; WITT, 2019). It is through the operation of infrared lamps that fusion agent manages to absorb the radiation and transform it into thermal energy, which in turn is used to sintering and fusing powder material. The first layer is made by initial fused materials, in sequence each step is repeated for every applied layer, and as the build platform lowers products are build up (O'CONNOR; DICKSON; DOWLING, 2018).

MJF is considered a process that builds faster than other powder bed fusion technologies, such as SLS, given the fact that it uses a planar source of radiation, capable of heating a larger area than other techniques (O'CONNOR; DICKSON; DOWLING, 2018). The technology is also known for its polyamide powder reusability, since it allows the reuse of up to 80% of used leftover powder, that are mixed with 20% of new, unused material for every printing (HP JET FUSION 3D PRINTING SOLUTIONS, 2017).

MJF has diverse applications for functional prototyping, manufacturing aids, and final parts production. These applications can be found in various industries such as aerospace, consumer goods, education, healthcare, manufacturing services, and transportation (HP 3D APPLICATIONS, 2019). Two examples in the automotive sector can be cited. The BMW Group, who used the HP Jet Fusion 3D 4200 to manufacture the window guide rail for its model BMW i8 Roadster. They remarked that with this technology it was possible to produce durable and reliable final parts (HP ACCELERATES 3D PRINTING MASS PRODUCTION WITH NEW CUSTOMERS, APPLICATIONS, AND PARTNERS, 2018). They were able to produce up to a hundred parts in twenty-four hours. Furthermore, over the last decade the company has produced a million parts with 3D printing technologies (BMW GROUP, 2018). Figure 2 displays the window guard rail part made for the BMW car.

Figure 2 - The window guide rail for BMW i8 Roadster.

Source: HP accelerates 3d printing mass production with new customers, applications, and partners (2018).

Similarly, the Volkswagen Group has been using the MJF technology to produce metal and polymers parts. Their goal was to have all tools used to manufacture the new model T-Cross SUV 3D printed. Another example is the Bowman International, that with the new HP 3D high-reusability PA11 material produced a bearing cage. This part uses rolling elements to hold together cage sections. The application of this material and MJF technology resulted in a product with 70% increase in the loading bearing capacity of its split bearings, and an increase in the working life of up to 500%. They had as well as equal strength on the X, Y and Z axes (HP ACCELERATES 3D PRINTING MASS PRODUCTION WITH NEW CUSTOMERS, APPLICATIONS, AND PARTNERS, 2018). Figure 3 shows the bearing cage produced by Bowman International.

Figure 3 - The bearing cage made with PA11 and MJF technology.

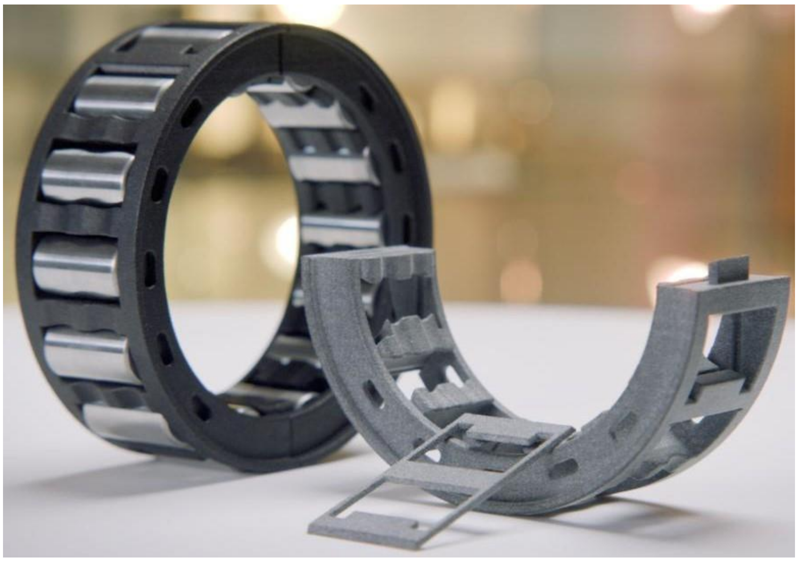

Source: HP accelerates 3d printing mass production with new customers, applications, and partners (2018).

2.1.2 Printing orientations

Printing orientation is one factor that can influence mechanical properties and accuracy of parts produced by 3D printing. Choosing different orientations results in layers being positioned distinctly inside parts. The direction in which layers are orientated defines how parts react to a given loading. In the printing process, the machine always creates horizontal layers. Hence, if a part is positioned horizontally all layers will be parallel to its length. Likewise, if a part is positioned vertically all layers will be perpendicular to its length.

Figure 4 - Example of layer orientation on parts printed horizontally and vertically.

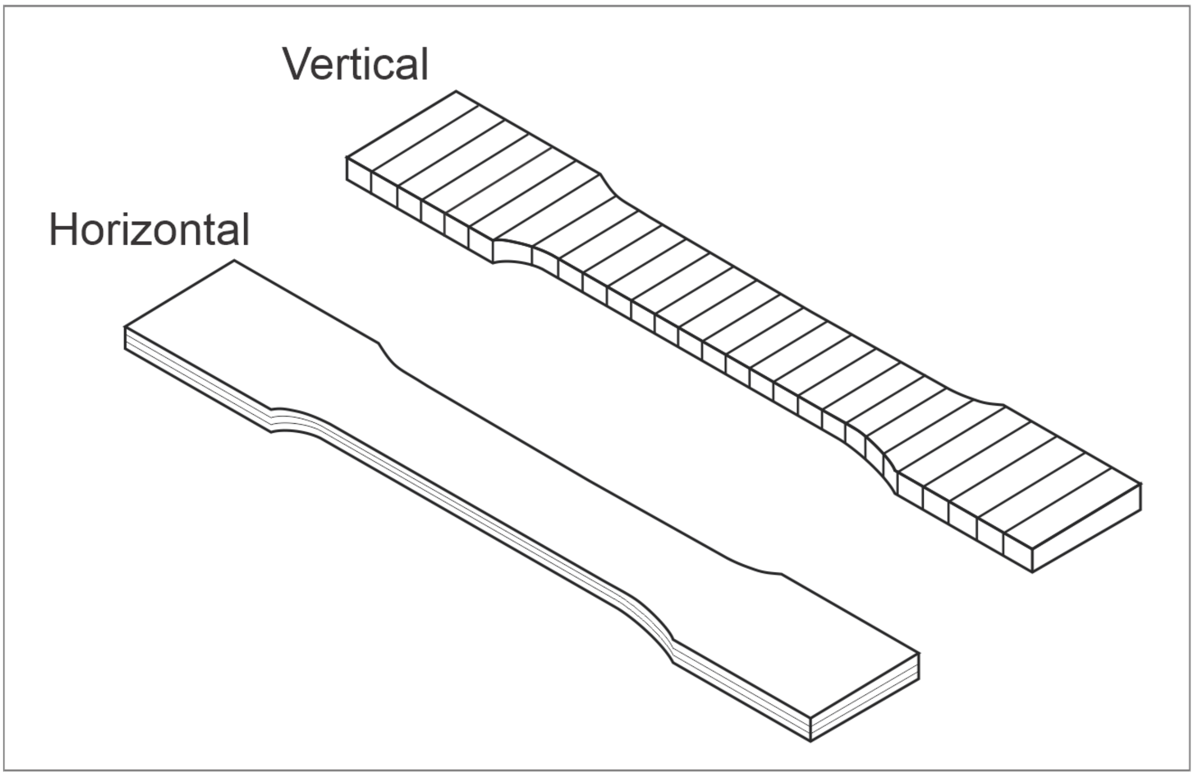

Source: adapted from Palma et al. (2019).

According to Palma et al. (2019), various works in literature have been analysing the behaviour of 3D printed parts, qualitatively and quantitatively through different characterization techniques. However, the majority of those studies have been made based on older technology, such as FDM and SLS. Considering that MJF is a newer technology and has been less studied, it can benefit greatly from such work, leaving a significant impact on its engineering applications.

Palma et al. (2019) analysed the influence of printing orientation on mechanical properties and tribological behaviour of polyamide 12 parts produced by MJF. Tensile test specimens were printed in two orientation, horizontally and vertically, along the X and Z axes, respectively. The vertical orientation had an average fracture stress of 47.77 MPa, and an average fracture strain of 17.4%. While the horizontal orientation displayed average fracture stress of 45.15 MPa, and an average of 23.2% for fracture strain. Generally, vertically printed samples failed at a higher stress but lower strain than horizontally printed samples. The resulting stress-strain curves were found to be consistent with other studies for 3D printed polyamide 12, in which a brittle fracture mode can be observed, instead of expected plastic ductile mode, caused by the multi-layer characteristic of this process. Differences in results between orientations were attributed to the distinct number of layer interfaces existing in each position. Vertical specimens have more layer interfaces, that can enhance strength. However, the load was applied normally to layers, that do not have resistance to elongation since interfaces are stronger but brittle.

Similarly, O’Connor, Dickson, and Dowling (2018) studied the mechanical performance of polyamide 12 parts, produced by MJF, highlighting the influence of building orientation on tensile and flexural properties. Specimens were printed in three orientations, along the X, Y and Z axes. However, specimens in Y axis were rotated 90 degrees, and had the biggest surface area side parallel to Y-Z plane. Each orientation had at least five samples tested. Regarding the tensile strength, no significant difference was found among the three orientations. The average for maximum tensile strength resulted in 47, 48 and 49 MPa, for X, Y and Z directions respectively. While, percentage of elongation at break was found to be higher for Y direction, with a result of 27%. The X and Z orientations registered only 19% and 16% each. The Y orientation had the lowest tensile modulus of 1,147 MPa, while specimens in X and Z orientation registered 1,242 and 1,246 MPa, respectively. Following the tensile test, micrographs of the fracture surface were analysed by scanning electron microscope. Ductile deformation was observed at the surface, and the ductility level of polyamide was considered substantially higher than in other PBF processes. After flexural measurements it was also found that there was a general trend in strength enhancement from X to Z (X < Y < Z). Even though the Z orientation is generally the weakest in SLS parts, for MJF the Z orientation might have a higher strength given the additional weight created by each new layer, which could contribute with denser and less porous parts. The degree of particle melting is also related to the mechanical properties. Since it was not observed a great variation in part’s strength, it was concluded that a relatively homogenous fusion happened at different locations in the volume bed.

2.2 Polyamide 12

The main material used by this new HP technology is polyamide 12 (PA12). Polyamide, a type of thermoplastic also known as Nylon, was discovered by DuPont in 1930, and first produced by them as textile fibers in 1939 (DUPONT). The number 12 present in its name comes from the fact that the monomer unit structure is composed by twelve carbon atoms, as shown in figure 5 (WOLFGANG; RUESTEM, 1970).

Figure 5 - PA12 monomer structure.

$$-[NH_2-(CH_2)_{11}-CO]_n-$$

Source: adapted from Rohde-Liebenau, 1999.

Rohde-Liebenau (1999), listed information and various properties, in a polymer data handbook, for PA12 obtained through regular extrusion. A few of these properties can be observed in the table below.

Table 1 - PA12 properties processed by traditional methods.

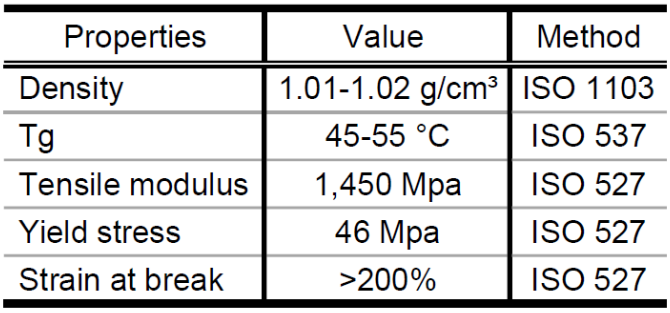

Properties	Value	Method
Density	1.01-1.02 g/cm³	ISO 1103
Tg	45-55 °C	ISO 537
Tensile modulus	1,450 Mpa	ISO 527
Yield stress	46 Mpa	ISO 527
Strain at break	>200%	ISO 527

Source: adapted from Polymer Data Handbook, 1999.

PA12 is one of the most commonly used polymers for PBF additive manufacturing process. Since the melting temperature is reasonably higher than the crystallization temperature, there is enough time for chainlike molecules to rearrange during cooling, and crystallization occurs. Hence, the crystallization is delayed during the build process, which reduces the accumulation of residual stress and distortions (ASKELAND; FULAY; WRIGHT, 2010; O'CONNOR; DICKSON; DOWLING, 2018). For this reason, HP recommends that the difference in temperature from the onset of the crystallization and melt to be preferably over 30°C, for PA12 powders used in the MJF process (TECHNICAL GUIDELINE FOR MATERIAL DEVELOPMENT WITH HP 3D OPEN MATERIALS PLATFORM, 2018). Melt temperatures of PA12 for powder bed fusion process like SLS have been reported to vary between 180.3°C and 186.1°C. While crystallization varied between 144.5°C and 151.8°C (SCHMID; WEGENER, 2016). The glass-transition temperature (T_g) is another important property shown in table 1, in which bellow this temperature amorphous polymers tend to behave like brittle and above like ductile materials (ASKELAND; FULAY; WRIGHT, 2010).

Mechanical properties of PA12 printed parts have been reported by various authors, using different PBF processes. In SLS process it was found a linear correlation between the increase of part density and its tensile strength. Similarly, increasing the crystallinity resulted in an increased tensile strength and decreased elongation (O'CONNOR; DICKSON; DOWLING, 2018). Generally, polyamide crystallize more easily compared to other thermoplastics. Crystallization helps to increase density, and mechanical properties, given the existence of strong secondary bonds between the polymer's molecules chains in crystalline region (ASKELAND; FULAY; WRIGHT, 2010).

2.3 Lattice structures

Cellular structures can be defined by the notion of having material merely in their vital regions, in order to obtain lightweight parts, while still preserving mechanical properties, such as high strength and energy absorption. These mechanical advantages can make them ideal for engineering applications. This type of structures includes foams, honeycomb, lattices, and other similar constructions. However, their complex geometry can prevent them from being manufactured through traditional methods, like casting, molding, and machining. On the other hand, additive manufacturing methods allows the production of these complex structures, that would not be technically or economically achievable otherwise. Improvements have been made to 3D printing techniques, enabling engineers and designers to easily fabricate cellular structures with the desired properties (GORGULUARSLAN et al., 2015), high precision (WANG et. al, 2019) and dimensions near to micrometer scale (RASHED et. al, 2016).

Lattice structures are periodic cellular structures, and this periodical characteristic allows them to be defined by a unit cell. A volume occupied by this structure is obtained by copying and multiplying the unit cell in all three dimensions (ARAUJO, 2018). Lattice structures have the advantage of being lighter and stronger than foam structures. This can be explained by lattice having highly hierarchical orientation and high strength-to-weight ratio, while foams have irregular structure resulting in overdesign (GORGULUARSLAN et al., 2015; RASHED et. al, 2016).

Wang et al. (2019) conducted the failure and energy absorption evaluation of four lattice structures under dynamic compression loading. Two of them had a diamond-based crystal structure. While the other two had the same geometry as in this study, the BCC and FCC (Octet-truss in this study). These structures were manufactured by selective laser melting (SLM) technique, using a titanium alloy Ti-6Al-4V. The behaviour of these structures was analysed under uniaxial dynamic compression, with experimental tests and numerical simulation. In the numerical simulation, the four lattice structures had different relative density, thus rods in their structures were given different diameter sizes. Each structure had at least seven diameter sizes, with their respective relative density. In the case of experimental compressive testing, only one relative density was used, with a rod diameter of 0.8 mm.

Numerical and experimental results were compared for all structures with rod diameter of 0.8 mm. The properties analysed were divided by the apparent density (given by mass divided by volume), resulting in specific modulus, specific strength and energy absorption per unit mass. In this case the FCC structure had the highest results for all properties, compared with BCC structure it had a 2.68 times higher specific strength, and a 3.33 times higher specific modulus. For the FCC structure the failure starts in the face-truss junction, while for BCC besides from the same point of stress concentration, the junction of intermediate rods also contributes for starting the failure. In this way, the stress distribution for FCC is more uniform, and not concentrated in joint points between rods in the middle of part like for the other three structures. Furthermore, the geometry of FCC is more complex, and all rods provide a stronger support for others, since there is more quantity of them connected at the same joints. From simulation of structures with different diameter, it was possible to observe that as the diameter size, or relative density, increases the better the compressive properties becomes, as expected (WANG et al., 2019).

In the study, it was compared as well the modulus and strength of the four lattices with other porous metallic materials, such as foam, honeycomb, and different lattices. Lattices structures have excellent mechanical properties, especially for lower relative densities structures, when compared to the other options. As the relative density decreases, its modulus and strength decrease more slowly. Even though materials that have diamond crystal structure usually have better mechanical properties than the ones made with BCC or FCC structures, for lattice materials based on these structures the opposite trend was observed (WANG et al., 2019).

2.4 Mechanical testing

Mechanical properties of materials can be determined using different tests. Usually these tests are destructives, since they cause fracture or make the material unusable. In this category are the tensile, compression, hardness, fatigue, impact, and bending and torsion tests. Nondestructive tests are also used to evaluate a few physical properties, as well as to detect internal defects in parts. Among the nondestructive category are x-ray, ultrasonic, and electromagnetic tests (SOUZA, 1982).

Materials properties depend on their composition and microstructure, and can be changed by materials processing methods. These properties are used to select engineered materials for load-bearing applications, combining them with the design specifications and service conditions required for the part (ASKELAND; FULAY; WRIGHT, 2010). One way to determine the most adequate mechanical testing to evaluate a specific material’s properties depend on its application, the type of loading it is supposed to withstand, and which properties are expected to be measured (SOUZA, 1982).

2.4.1 Tensile test

A common mechanical test used to determine materials properties is the tensile test. It measures the resistance of a given material to a static or slowly applied force. Through it is possible to obtain a variety of mechanical properties, such as tensile strength, yield strength, modulus of elasticity, stiffness, Poisson’s ratio, modulus of resilience, tensile toughness, and ductility. In this test a universal testing machine is applied, on which both tensile and compressive tests can be done. Usually the strain rates are small, between 10^{-4} to 10^{-2} s^{-1}. To measure the resulting amount of the specimens that stretches among gage marks, a strain gage or extensometer is used. Hence, what is measured is the final length of the specimen, or its change compared to initial length. The data recorded in the tensile test comprises of the load or force applied, as a function of the change in length. In sequence, these data have to be transformed into stress and strain values, in order to obtain a stress-strain curve (ASKELAND; FULAY; WRIGHT, 2010). This fact can be explained if it is considered that specimens might have different cross-sectional areas, and fail at higher forces when these areas are larger. Similarly, specimens that have a larger length will result in larger length change after testing. Therefore, using stress and strain values guarantees that a given material will have the same yield, maximum, and fracture values, for stress and strain, with samples of any cross-section and length (DOWNLING, 2006). The stress and strain calculated in this manner will result in the engineering stress-strain curve. The units commonly used for stress is MPa, and strain is centimeter/centimeter or percent. In the following figure it is possible to observe an example of engineering stress-strain curve, for a typical ductile metal, an aluminium alloy (ASKELAND; FULAY; WRIGHT, 2010).

Figure 6 - The engineering stress-strain for an aluminium alloy.

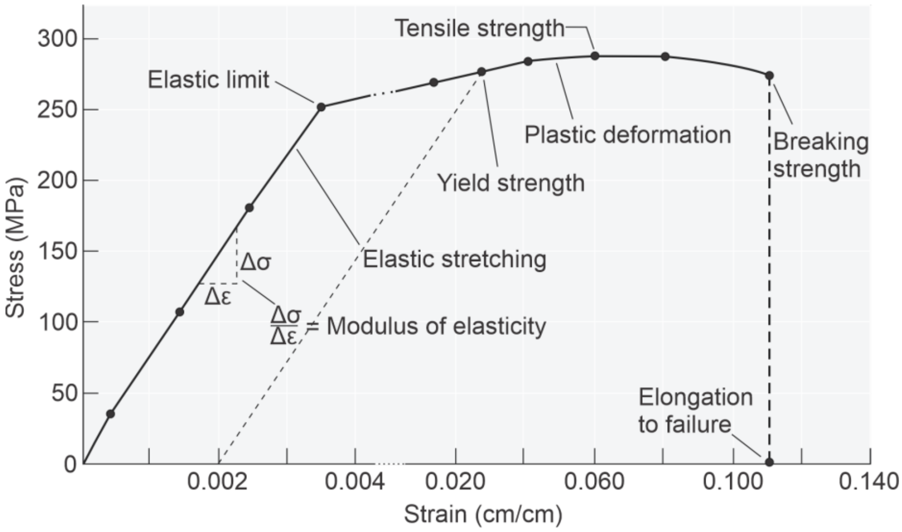

Source: adapted from Askeland; Fulay, 2009.

The engineering stress-strain curve displays a parallel line at the offset strain value of 0.2%, used to define the yield strength, at its intersection with the curve. This offset was defined to substitute elastic or proportional limits, since they cannot be determined precisely. Hence, yield strength can represent the stress value above which plastic deformation also occurs, in addition to elastic deformation. For polymeric materials the stress needed to begin plastic deformation refers to the disentanglement of molecule chains, or the sliding of these chains past one another. Typical values for polymeric materials range from 10 to 100 MPa (ASKELAND; FULAY; WRIGHT, 2010).

The tensile strength, or ultimate tensile strength, is the maximum stress obtained in the engineering stress-strain curve. For many ductile materials a phenomenon known as necking occurs, because some regions start to deform more than others, causing a higher local decrease in cross-sectional area. A smaller cross-sectional area requires a lower force for its deformation to continue. Consequently, the engineering stress decreases, since it is calculated using the initial area value. In ductile materials, as the example in figure 6, the necking begins at tensile strength, hence stress declines from that point forward (ASKELAND; FULAY; WRIGHT, 2010).

Modulus of elasticity, Young's modulus or tensile modulus, is defined by the slope described on figure 6, in the elastic region of the curve. It is related to the binding energies of atoms, so a steep slope denotes the necessity of higher forces to separate these atoms, and allow the material to deform elastically. This indicates a material with a high modulus of elasticity, that deforms less elastically than ones with lower moduli. Given the strength of atomic bonds in metals and ceramics, they display much higher values than polymers. As an example, the modulus of elasticity of a nylon material is 2.7 GPa (ASKELAND; FULAY; WRIGHT, 2010).

Another property obtained in tensile test, is ductility, which represents the capacity of a material to withstand a force while deforming permanently without breaking. This property can be measured by the percentage of elongation, that quantifies only the permanent plastic deformation, excluding the elastic deformation recovered after the fracture happens. It is measured by the distance between gage marks made on specimens before and after the test. The strain at break point considers the elastic deformation, hence it is larger than the strain after failure (ASKELAND; FULAY; WRIGHT, 2010).

The majority of thermoplastics such as polyamide, display a viscoelastic mechanical behaviour around T_g, which means that for most part of the stress-strain curve its response to a load is not linearly related. Also, under load the material has both elastic and plastic deformation, and this process depends on time and rate of the applied load. This behaviour is highly connected to the way in which the polymer's molecules chains slide past one another. Mechanical properties also depend on temperature, many polymers become more brittle when below their T_g, and more ductile when above it. The next figure displays a stress-strain curve for 6,6-nylon material produced by conventional methods (ASKELAND; FULAY; WRIGHT, 2010).

Figure 7 - The stress-strain curve for 6,6-nylon.

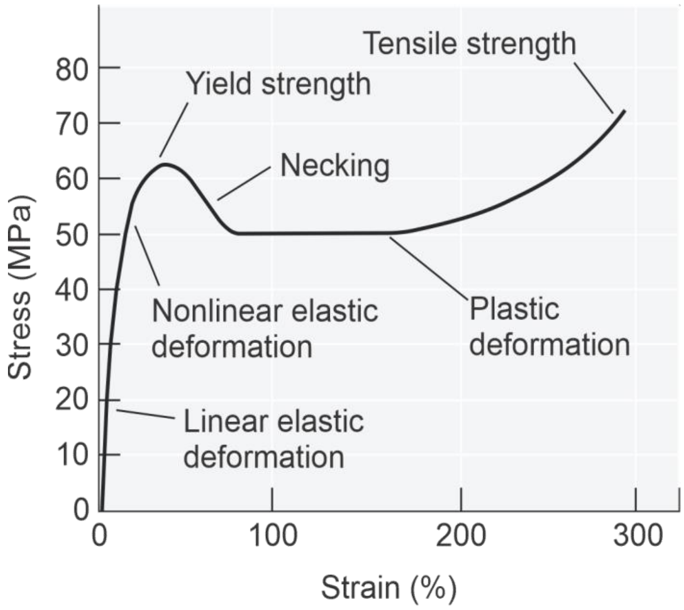

Source: adapted from Askeland; Fulay, 2009.

In this stress-strain curve of 6,6-nylon material is possible to observe both elastic and plastic deformations, typical of thermoplastics. The elastic deformation is caused by the stress that stretches and distorts covalent bonds existing inside chains, allowing them to elongate elastically. After the stress is removed, the deformation is recovered almost immediately. The polymer can also have entire sections of chain distorted, but after the stress is removed they recover to initial positions after a period of time (hours or months). If the stress applied is higher than the yield strength, then the plastic deformation happens. In this case, chains can stretch, rotate, slide, and disentangle. The sudden decrease in stress observed in the curve is caused by untangling and straightening of chains, as well as possible necking which allows chains to slide continually at lower stresses. The neck propagates along the length of the specimen, instead of staying in one region. However, when chains align parallel to load and get closer to one another, stronger secondary bonds emerge between chains, and higher stresses are required to finish the deformation and fracture occur. This strengthening is a result of crystallization due to orientation, and such characteristic helped establish nylon as an option for creating strong fibers (ASKELAND; FULAY; WRIGHT, 2010).

3. Materials and methods

3.1 HP Jet Fusion 4200 3D

The printer with MJF technology used in this project was the model HP Jet Fusion 4200 3D. This printer model is composed with a processing station and built units, which perform necessary functions in this process beyond the printing step. Fusing and detailing agents are stored in the printer and provided in the printing moment. While polyamide powder is provided by the processing station and loaded inside a build unit, which is then connected to the printer.

In the printing process of specimens, it was used the balanced mode, which produced a layer with thickness of 0.09 mm, and the temperature used for melting was 189 °C. Each layer made took nine seconds to be completed. The figure 8 displays the printer model used to produce specimens for this project.

Figure 8 - HP Jet Fusion 4200 3D Printer.

Source: author.

The processing station has an essential part in printing process. It allows printing preparations and finalization, which include steps made for using build units, such as loading, cooling, and unpacking.

Initially in the process, a built unit is connected to the processing station, making it possible to load the unit with polyamide powder. The volume can be filled and measured at the station, then the built unit is handled and connected to the printer to start the manufacturing process. After the printing is done the built unit is taken from the printer to the processing station again. In the sequence, there is the cooling step, it can be done naturally with a considered waiting time, or it can be speed up with the station's fast cooling option. The last step involves unpacking of printed parts, with the assistance of available vacuum cleaner. In this technology all the used leftover powder is vacuumed and stored in a barrel, that later can be reused, mixed with new powder in the loading step. All parts printed in this study were made with 80% of reused powder, mixed with 20% of the new one, and with natural cooling process. Even though the leftover powder is vacuumed, some still stay attached to parts surfaces, so it is necessary that an abrasive process be applied in order to remove every remained powder not fused in printing. All these steps are repeated for a new printing process. Figure 9 displays the processing station.

Figure 9 - HP Jet Fusion 4200 3D Processing Station with Fast Cooling.

Source: author.

The built unit’s top platform is where parts are printed. While platform’s building area moves down, layers of powder coming from the inside is added to the created working space. Hence at the end of the process there is a building volume of 380 x 284 x 380 mm. It is essential to have at least two built units available in place, in order to maintain a continuous printing process of products. Printed parts always occupy a built unit during the whole cooling period, that can amount to more than an entire day. During this time another built unit can be used to continue the printing work. Figure 10 displays one built unit.

Figure 10 - HP Jet Fusion 3D Built Unit.

Source: author.

3.2 Materials

Materials used to build specimens include polyamide 12, which constitutes parts, fusing agent and detailing agent, that are employed in the process. According to Palma et al. (2019, p. 2), “These agents are water-based latex with proprietary compositions, and almost entirely evaporate during the rest of the process”. The PA12 powder is supplied by HP, and have the following properties shown in table 2.

Table 2 - PA12 properties from supplier.

	Measurement	Value	Method
General properties	Powder melting point (DSC)	187 °C	ASTM D3418
	Particle size	60 µm	ASTM D3451
	Bulk density of powder	0.425 g/cm^3	ASTM D1895
	Density of parts	1.01 g/cm^3	ASTM D792
Mechanical properties	Tensile strength	48 Mpa	ASTM D638
	Tensile modulus	1,800 MPa	ASTM D638
	Elongation at break (XY, XZ, YX, YZ)	20%	ASTM D638
	Elongation at break (ZX, ZY)	15%	ASTM D638

Source: adapted from HP 3D High Reusability PA 12, 2019.

3.3 Printing of solid tensile test specimens

Solid tensile test specimens were developed using the CAD software Autodesk Inventor Professional 2019, as well as following guidelines of the standard ISO 527-2 (ISO, 2012) for specimens' geometry and dimensions. There were printed 150 specimens, in two different occasions, by Laboratory of prototype technologies and processes. It was planned the production of 75 specimens, however given a mistake in defining dimensions of drawing, the first tensile specimen had its length 0.5 mm bigger than recommended by the standard, and its width in the middle part 0.4 mm smaller. Hence another drawing was made with the specified dimensions, and 75 more specimens were printed again in a second batch. Figure 11 illustrates the solid tensile test specimen and its dimensions.

Figure 11 - Solid tensile test specimen.

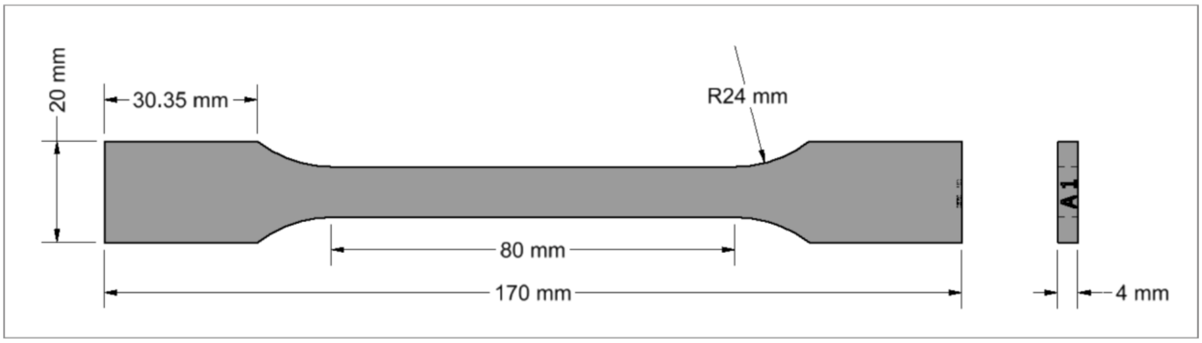

Source: author.

Specimens received the nomenclature of letters from A to E, representing the possible five printing directions. Each of the five printing direction was given three different angles, 0°, 45° and 90°. These angles received the denomination of 1, 2 and 3, respectively. Letters A, B and C represents specimens positioned parallel along three axes X, Y and Z. Figure 12 illustrates A, B, and C directions.

Figure 12 - Illustration for A, B and C specimens directions.

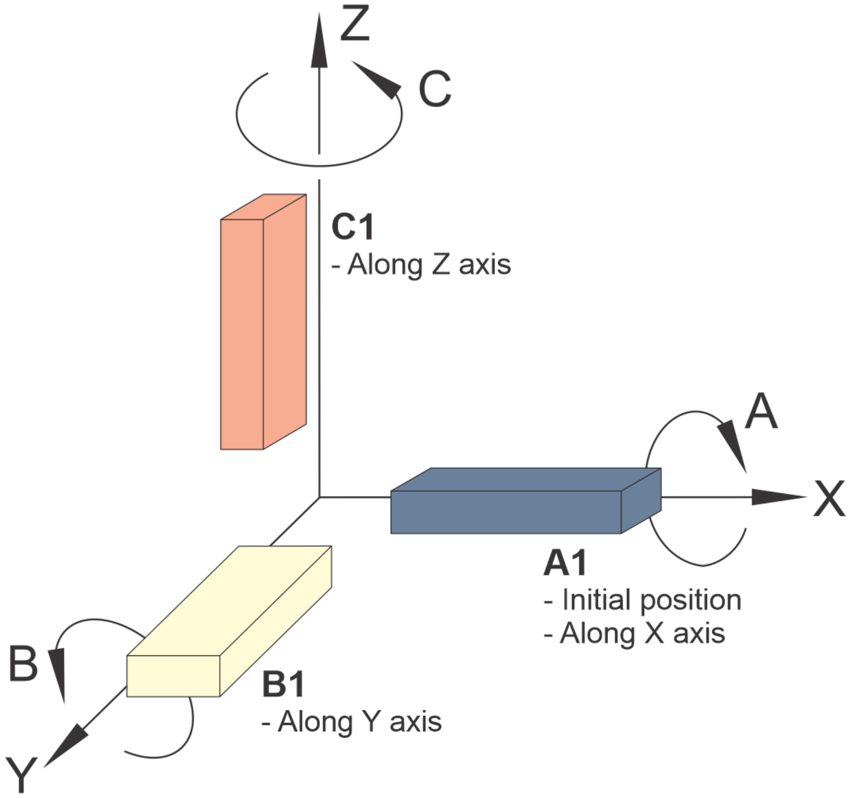

Source: author.

Letters D and E represents specimens that were rotated in the Cartesian coordinate system from an initial position. It was taken A1 as the initial position, of specimens along the X axis, with an angle of 0°, and in X-Y plane, for reference. From this initial position specimens D were rotated 45° around the Z axis, and remained in X-Y plane. While specimens E were rotated 45° around the Y axis, and rotated again -45° around the Z axis, ending in a position in space. Specimens D and E were also in the mentioned three angles 0°, 45° and 90°. Rotations around X, Y and Z were denominated A, B and C, respectively. The schematics of rotations to obtain D and E positions are illustrated in the next figure.

Figure 13 - Illustration of rotations for D and E specimens.

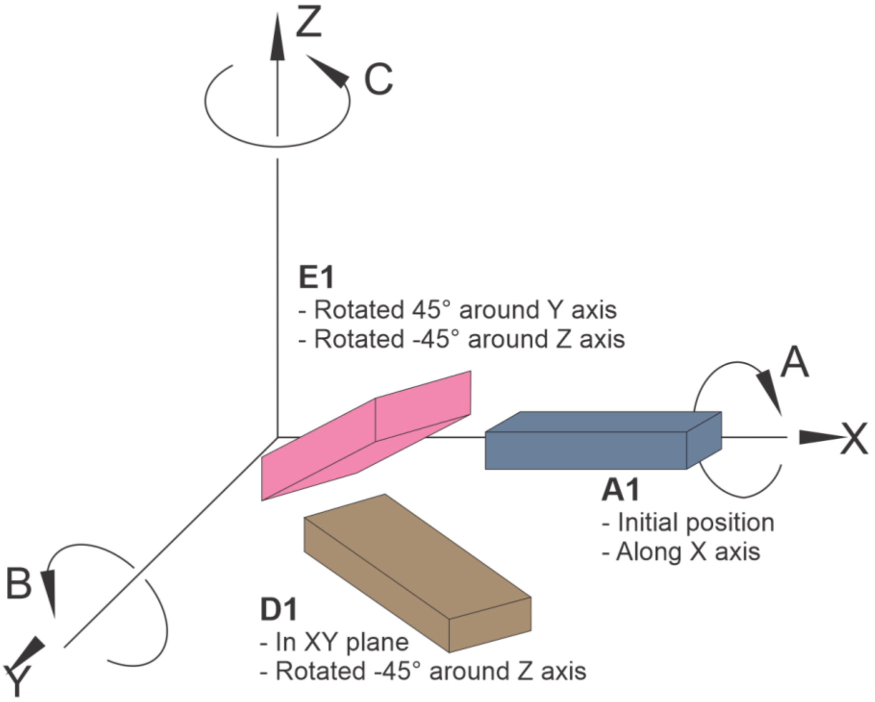

Source: author.

In order to identify all specimens, letters A, B, C, D and E, and numbers 1, 2 and 3 were printed in each one of them. All these arrangements resulted in fifteen printing orientations, that can be observed in the next figure.

Figure 14 - Illustration of the defined fifteen printing orientations.

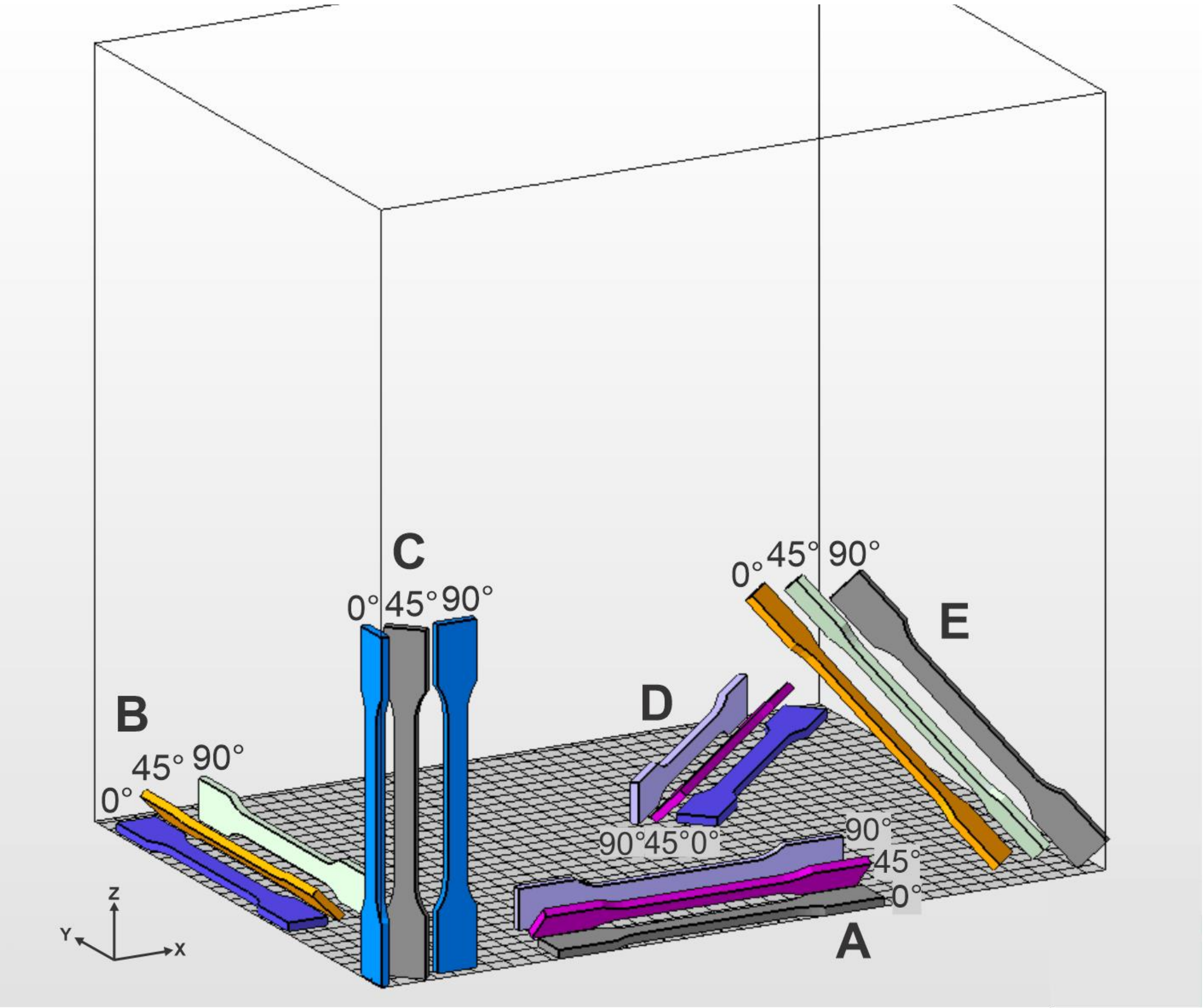

Source: author.

These printing orientations were produced five times each, for statistical reasons. Resulting in a production of 75 printed specimens, repeated in a second printed version which created a group nomenclature with 30 elements. As explained before the letter in the first position of a name refers to print direction; the second position is occupied by numbers from 1 to 3, representing angles options; and the last two positions refers to either first printing version (V1), in which specimens had small different dimensions, or second printing version (V2). The explanation of nomenclature is illustrated in the next figure.

Figure 15 - Solid specimens’ nomenclature.

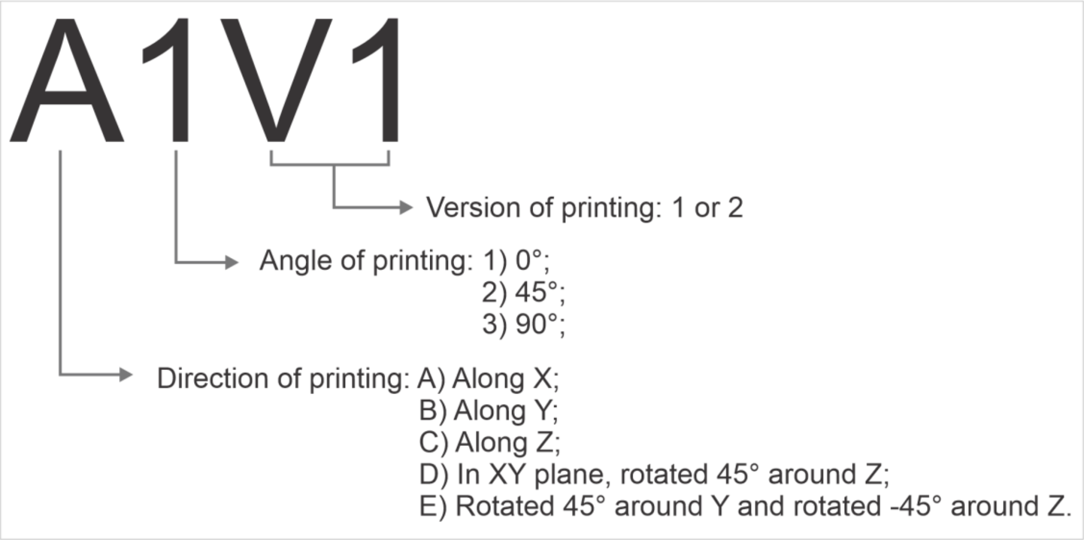

Source: author.

Parts resulting from the printing process still display unfused powder attached to its surface, even after being vacuumed cleaned in the processing station. For this reason, an abrasive process needed to be applied to obtain the necessary surface finish in all parts. A sand blasting machine was used to clean the parts.

3.4 Printing of lattice structures tensile test specimens

A total of three lattice structures were developed for this project, with the aid of CAD software Autodesk Inventor Professional 2019. For each one of these structures a basic cubic unit was used to define the final design, having a volume of 125 mm³, in a 5 mm side cube. Different levels of volume fill were given to each design, meaning the volume occupied by material were 10, 25, 50 and 70% of the available 125 mm³ space. These levels of filling were obtained by modifying and raising size of diameters existing in every structure.

The first unit structure designed had simple geometry of cylindrical rods positioned in the direction of three Cartesian axes, intercepting each other in its middle positions. Edges caused by interception were rounded for better results. It was named Cross, and an image with 10% of occupied volume can be seen in the next figure.

Figure 16 - Cross structure with 10% of occupied volume.

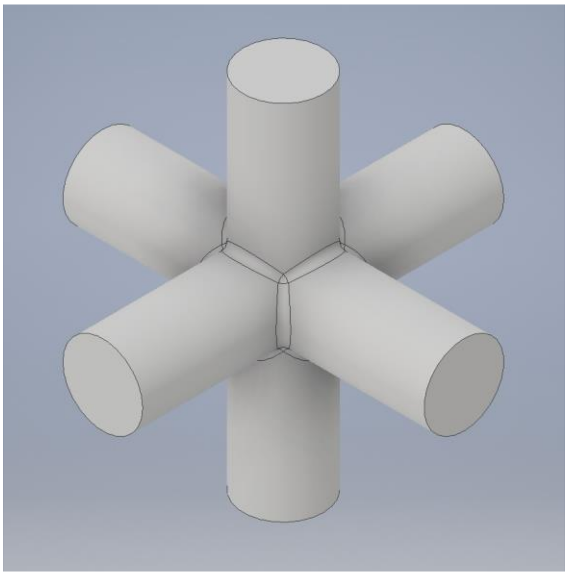

Source: author.

Table 3 displays values for cylindrical rod diameters existing in Cross structure, and their respective structure volumes, for each percentage of volume filled.

Table 3 - Cylindrical rod diameters and volumes of Cross structure.

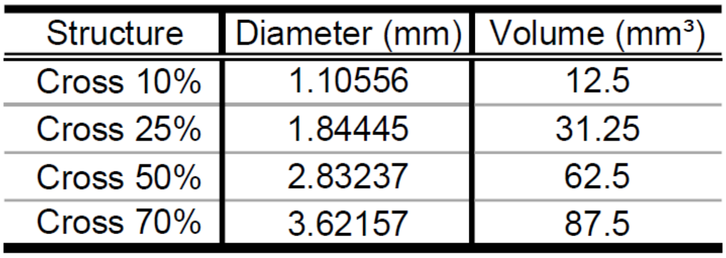

Structure	Diameter (mm)	Volume (mm³)
Cross 10%	1.10556	12.5
Cross 25%	1.84445	31.25
Cross 50%	2.83237	62.5
Cross 70%	3.62157	87.5

Source: author.

The second structure named BCC, as allusion to geometry of body- centered cubic unit cell present in crystalline structures, where one atom occupies each vertex of a cube and its center position. In this case, cylinders were positioned connecting the center to each vertex. Just like before edges present in the center of structure were left rounded. An image of this unit structure with 25% of occupied volume can be observed in figure 17.

Figure 17 - BCC structure with 25% of occupied volume.

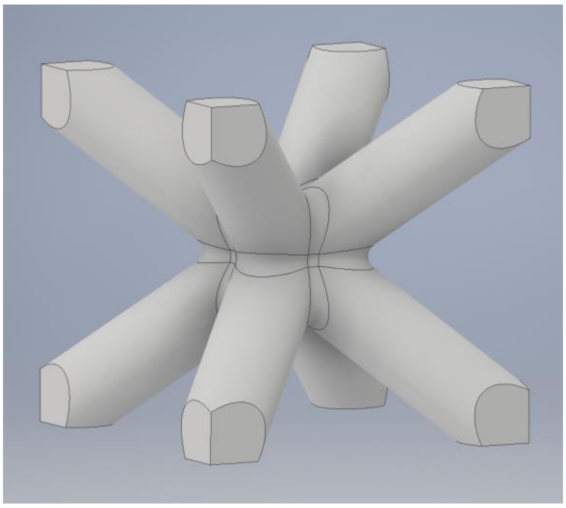

Source: author.

Table 4 displays values for cylindrical rod diameters existing in BCC structure, and their respective structure volumes, for each percentage of volume filled.

Table 4 - Cylindrical rod diameters and volumes of BCC structure.

Structure	Diameter (mm)	Volume (mm^3)
BCC 10%	0.73074	12.5
BCC 25%	1.21745	31.25
BCC 50%	1.86675	62.5
BCC 70%	2.37842	87.5

Source: author.

In the case of third structure named Octet-truss (Octet), it was based upon a face-centered cubic unit cell structure, which can be described as having one atom at each vertex of a cube, and also one at each face center. Following the previously idea, cylinders were positioned as if connecting atoms at each face center position to others, without any cylinder crossing in the center of the structure. This structure had a problem during the design with 70% of occupied volume, it was not possible to round the edges around cylinders interceptions. Hence, this level of filling was not printed, and this structure had only three variations of occupied volume manufactured. An example of this design can be observed in figure 18, which portrays a unit structure with 50% of occupied volume.

Figure 18 - Octet structure with 50% of occupied volume.

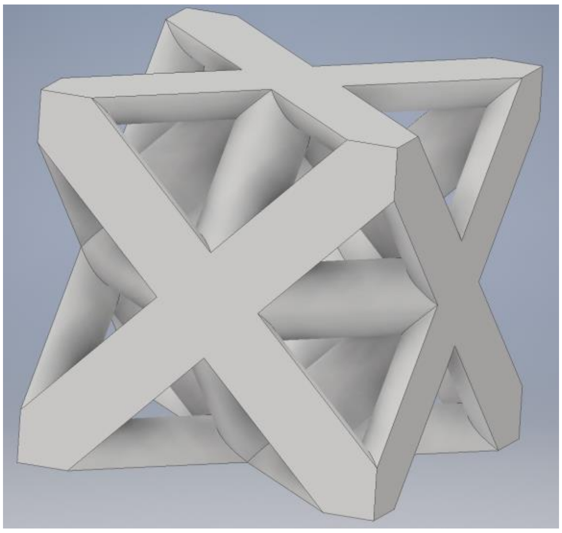

Source: author.

Table 4 displays values for cylindrical rod diameters existing in Octet structure, and their respective structure volumes, for each percentage of volume filled.

Table 5 - Cylindrical rod diameters and volumes of Octet structure.

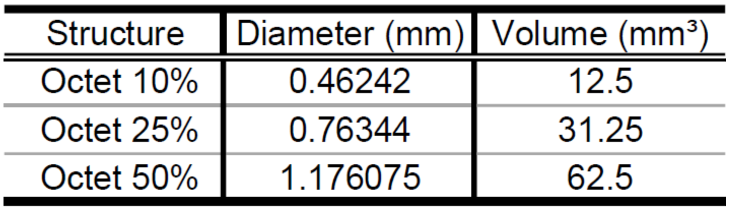

Structure	Diameter (mm)	Volume (mm³)
Octet 10%	0.46242	12.5
Octet 25%	0.76344	31.25
Octet 50%	1.176075	62.5

Source: author.

A new tensile test specimen was developed based on the geometry of specimens found in Gorguluarslan et al., (2015). This geometry was defined to accommodate lattice structures in its middle part, without creating a fragile specimen, as it happens with regular ones defined by tensile testing standards. For this reason, the center of specimen was increased in volume, reaching the size capable of containing a pattern made with any structure unit. All these units were used to create tensile test specimens containing structures in their middle part, that occupies a space with 50 mm in length, 20 mm in width, and 20 mm in depth. Images of all developed units can be found in the appendix A section, as well as the tensile test specimen used with its dimensions. The next figure illustrates the geometry of test specimen made to contain structures.

Figure 19 - Lattice structure tensile test specimen.

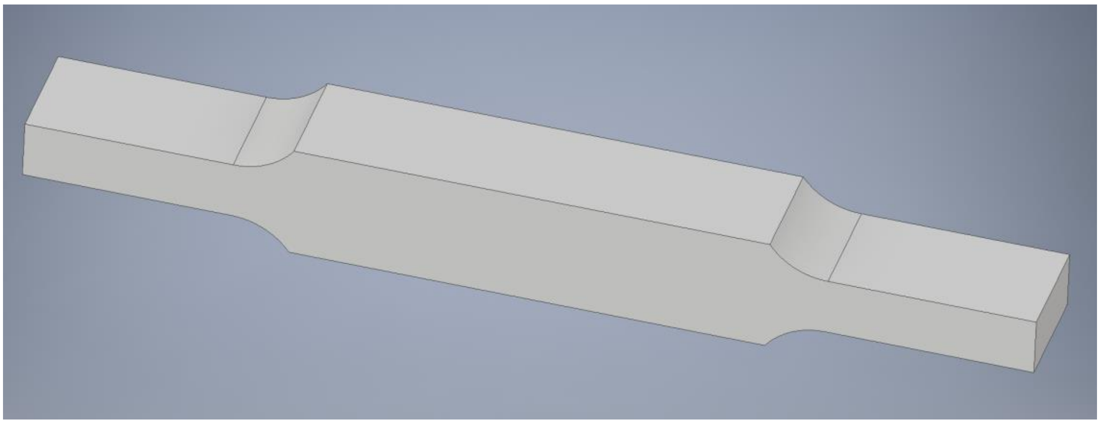

Source: author.

In addition to varying structures types and their percentage of volume filling, these specimens were printed in four possible different orientations. The definition of printing orientations used an initial position as reference, the same described for solid specimens. That is a specimen positioned along the X axis, with an angle of 0°, and in X-Y plane. Rotations used around X, Y and Z were again denominated A, B and C, respectively. The four defined orientations are illustrated in the next figure.

Figure 20 - Illustration of orientations and rotations for lattice structures specimens.

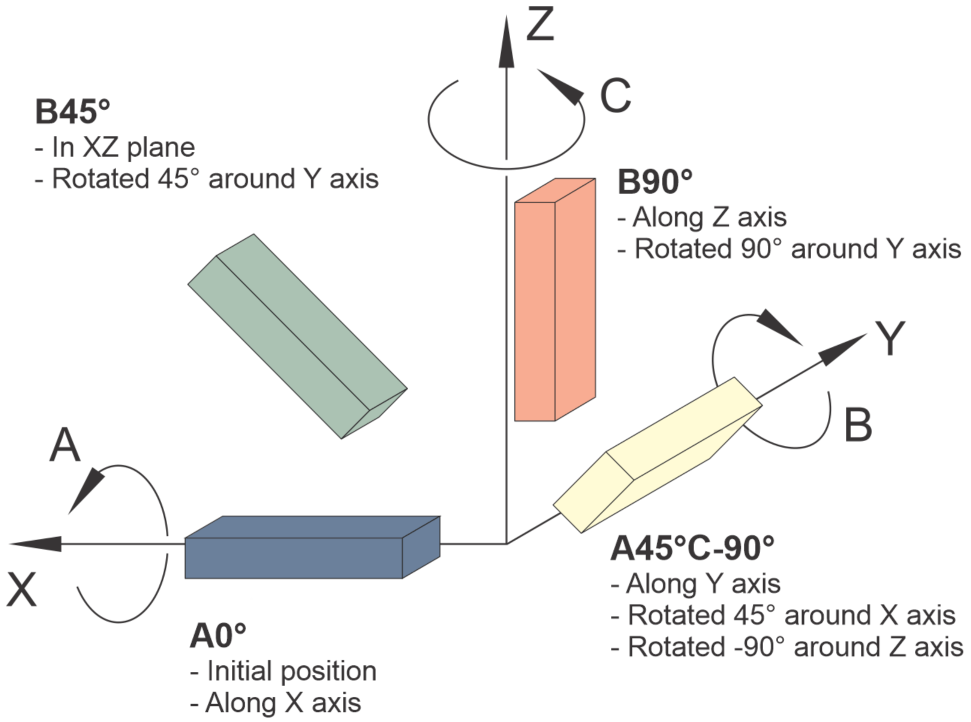

Source: Laboratory of prototype technologies and processes, 2019.

Cross specimens were printed in A0°, B45° and B90° orientations, for each one of the four percentages of filling. BCC specimens were printed in three orientations as well, A0°, A45°C-90° and B90°, for the four percentages. However, BCC structure was not tested in B45° because resulted specimens in this orientation became too fragile to undergo an abrasive process to remove the powder from its surface. Hence, it was not possible for them to be post-processed or mechanical tested. Whereas Octet specimens were printed in two orientations, A0° and B45°. This last structure had very fragile specimens when printed with 10% of volume filling, also preventing them to be post-processed or tensile tested. Therefore, Octet structure specimens were printed and tested for 25% and 70% of occupied volume, and in A0° and B45° orientations. All steps of printing process were made by the Laboratory of prototype technologies and processes.

In order to obtain the necessary surface finish after printing and remove all remaining loosely bonded powder, an abrasive process was applied in all parts. A sand blasting machine was used to clean the parts surfaces.

3.4 Tensile test

The same tensile test was applied to analyse the behaviour of all solid, and structure filled parts. These tests were performed by the Laboratory of prototype technologies and processes, in the Technical University of Liberec. The machine used to perform tests was a TIRAtest Universal testing machine from TIRA GmbH, a German company of testing and measuring technologies. In tests it was applied a load rate of 1 mm/min, and a force transducer KAF 100 kN. Tests were performed according to ISO 527-2.

3.4.1 Solid specimens

Tensile tests of solid specimens resulted in data set on force and displacement for each specimen evaluated. These results were used to plot stress-strain curves, separated in thirty graphs for each orientation and two versions of printing. Every graph contains five curves of existing samples, and from them it was determined a few mechanical properties of material, such as modulus of elasticity, yield strength, and ductility.

The maximum tensile strength and strain at break of every specimen were obtained directly as a result from the tensile test, and did not need to be calculated. For each orientation it was calculated its corresponding average values, and bar charts were plotted separately for these two properties.

From the stress-strain curves it was possible to determine the other three mentioned properties. The modulus of elasticity was calculated as the slope of elastic region in each curve for all specimens. The average values were determined for each orientation, and a bar chart was plotted. This property was defined by the following equation, where S is the engineering stress and e the engineering strain.

Equation 1 - Equation for modulus of elasticity

$$E = \frac{S}{e}$$

Source: adapted from Askeland; Fulay; Wright, 2010.

In order to determine yield strength from the stress-strain curves, a line was drawn parallel to the linear section of each curve, at 0.2% offset of strain. The offset yield strength, or just yield strength, is defined as the stress value corresponding to the intersection of the drawn line and the curve. After the values were determined, its average values were calculated for each orientation and organized in a bar chart.

The ductility differs from strain at break because it does not consider the elastic deformation contribution, instead is a measure of permanent plastic deformation. Hence, from the stress-strain curves it was determined values for strain in the elastic portion, and those were subtracted from the maximum strain values. In sequence, for each orientation average values were calculated and organized in a bar chart.

3.4.2 Lattice structures specimens

Tensile tests of lattice structure specimens resulted in data set on force and displacement for each specimen evaluated. Given the complexity of every structure cross-sectional area and the difficulty to determine its value, it became impracticable to calculate the stress, since it involves dividing resulting force values by initial area. Consequently, it was not possible to obtain the stress-strain curves. Hence, it was used the values of force and displacement to plot curves for each specimen. These curves were used to illustrate the performance of each structure, regarding every printing orientation used, and different volume filling or percentage of occupied volume. In order to obtain better comparison between structures results, bar charts were also made. In this case, it was analysed the same structure considering the same occupied volume but different orientations. As well as, different structures but having the same orientation and occupied volume. Therefore, it was possible to compare which structure had the best performance for each volume of filling, and which orientation was the best to print them. In the next figure it is possible to observe a BCC structure specimen positioned for tensile testing.

Figure 21 - Tensile test specimen with BCC structure positioned in testing machine.

Source: Laboratory of prototype technologies and processes, 2019.

4. Results and discussions

4.1 Printing orientation of solid parts

The 150 specimens were subjected to tensile testing, which resulted in information about the material’s properties. In the test, it was determined the maximum values for stress and strain. Likewise, values for force and displacement were also obtained, and were used to plot stress-strain curves for each specimen. In sequence, from these curves it was determined the maximum tensile strength, strain at break, modulus of elasticity (Young’s modulus), yield strength, and ductility. These properties allow comparison with values found in literature. Figure 22 shows printed solid tensile test specimens before the testing.

Figure 22 - Printed tensile test specimens.

Source: author.

Examples of specimens after the tensile test are shown in figure 23. In this figure it is possible to observe that these specimens had small elongation after fracture, and no necking was developed.

Figure 23 - Solid specimens after tensile test.

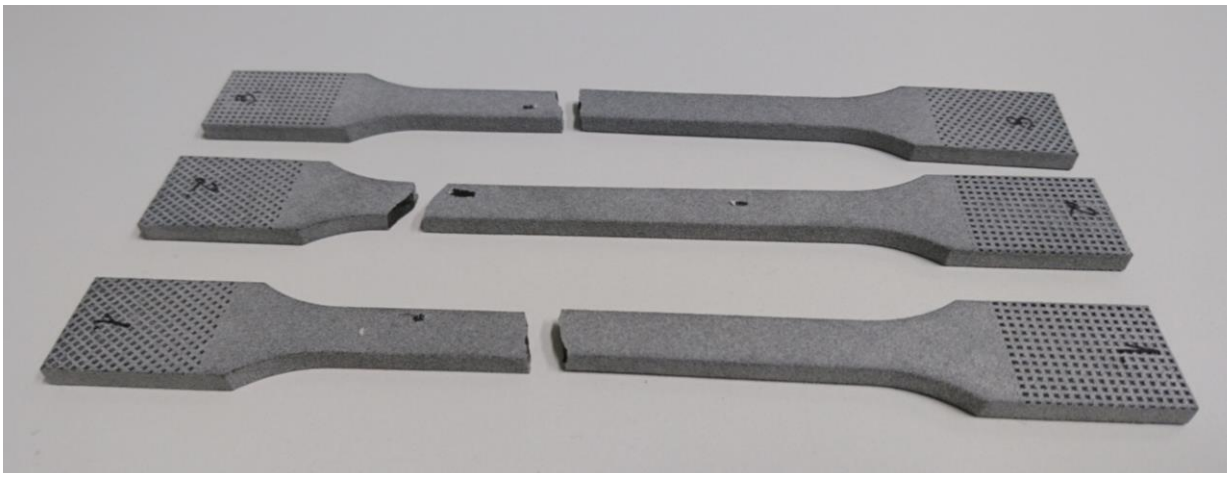

Source: author.

Average values for all results analysed were organized in the table 6, shown below. For each property listed in the table, a bar chart was plotted with average values of five samples per orientation, as well as its relative standard deviation, and they will be presented in the sequence.

Table 6 - Average values for maximum stress, strain at break, modulus of elasticity, yield strength, and ductility.

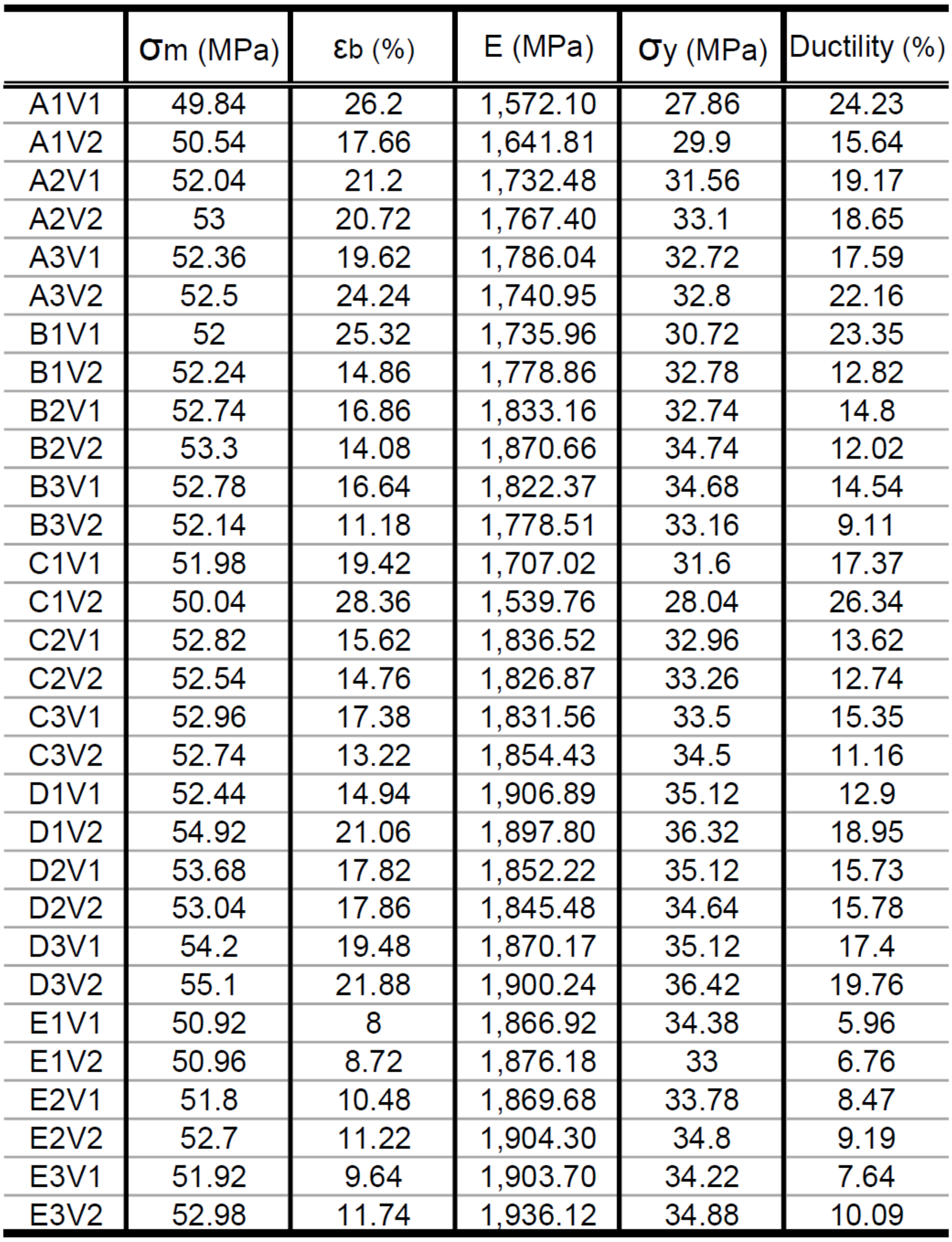

	σ_m (MPa)	ε_b (%)	E (MPa)	σ_y (MPa)	Ductility (%)
A1V1	49.84	26.2	1,572.10	27.86	24.23
A1V2	50.54	17.66	1,641.81	29.9	15.64
A2V1	52.04	21.2	1,732.48	31.56	19.17
A2V2	53	20.72	1,767.40	33.1	18.65
A3V1	52.36	19.62	1,786.04	32.72	17.59
A3V2	52.5	24.24	1,740.95	32.8	22.16
B1V1	52	25.32	1,735.96	30.72	23.35
B1V2	52.24	14.86	1,778.86	32.78	12.82
B2V1	52.74	16.86	1,833.16	32.74	14.8
B2V2	53.3	14.08	1,870.66	34.74	12.02
B3V1	52.78	16.64	1,822.37	34.68	14.54
B3V2	52.14	11.18	1,778.51	33.16	9.11
C1V1	51.98	19.42	1,707.02	31.6	17.37
C1V2	50.04	28.36	1,539.76	28.04	26.34
C2V1	52.82	15.62	1,836.52	32.96	13.62
C2V2	52.54	14.76	1,826.87	33.26	12.74
C3V1	52.96	17.38	1,831.56	33.5	15.35
C3V2	52.74	13.22	1,854.43	34.5	11.16
D1V1	52.44	14.94	1,906.89	35.12	12.9
D1V2	54.92	21.06	1,897.80	36.32	18.95
D2V1	53.68	17.82	1,852.22	35.12	15.73
D2V2	53.04	17.86	1,845.48	34.64	15.78
D3V1	54.2	19.48	1,870.17	35.12	17.4
D3V2	55.1	21.88	1,900.24	36.42	19.76
E1V1	50.92	8	1,866.92	34.38	5.96
E1V2	50.96	8.72	1,876.18	33	6.76
E2V1	51.8	10.48	1,869.68	33.78	8.47
E2V2	52.7	11.22	1,904.30	34.8	9.19
E3V1	51.92	9.64	1,903.70	34.22	7.64
E3V2	52.98	11.74	1,936.12	34.88	10.09

Source: author.

The first bar chart plotted display the average values for maximum stress, or tensile strength. Values varied between 49.84 MPa and 55.1 MPa, representing an increase of 10.55% in strength, comparing the lowest to the highest values. The maximum tensile stress reported by HP is 48 MPa, which is 12.88% lower than the maximum average value obtained in this study, and 3.69% lower than the minimum average value found.

Graph 1 - Average maximum stress values.

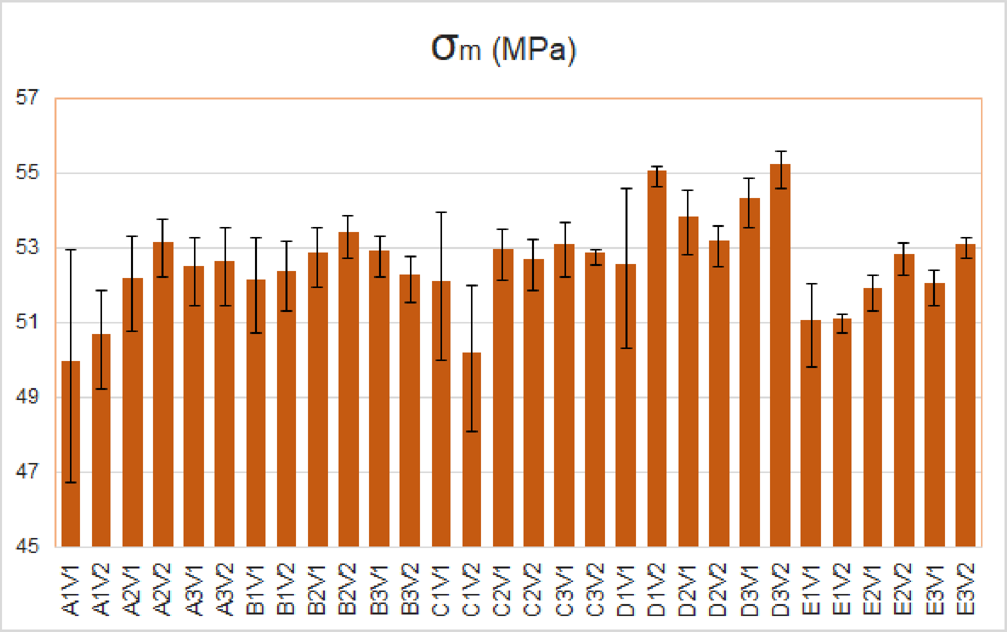

Source: author.

It is possible to observe the trend reported by Palma et al. (2019), and O'Connor, Dickson, and Dowling (2018), where the strength increases from X direction to Z direction, with Y direction having intermediate values. Likewise, in this study, the strength increases from A to C specimens, with B showing intermediate values. There are a few exceptions, like the case of C1V2 specimens, that despite being positioned in Z orientation resulted in one of the smallest tensile strength values. Comparing C1V2 with its version 1 of printing (C1V1), the second version had a reduction of 3.73% in maximum stress.

Another two directions were tested besides common ones (along X, Y, and Z direction). They are represented by D and E specimens, in which to obtain those directions 45 degrees rotations, around the Z axis, and around Y and Z axes, respectively, were applied. D specimens had the highest stress values, with the exception of D1V1, which had the second biggest standard deviation, after A1V1. D1V1 values varied between 48.4 MPa and 54.1 MPa. The highest average stress value was reached by D3V2 specimens, followed by D1V2 at 54.92 MPa. In general, E specimens had a relative inferior mechanical performance, with results between the lowest stress values.

Graph 2 represents average values for strain, obtained at specimens failure. These values correspond to the maximum resulted elongation, considering elastic and plastic deformations. Values varied between 8% and 28.36%, representing an increase of 254.5% in strain at break, comparing the lowest to the highest values. The elongation at break reported by HP is 20% for most printing orientations, and 15% for specimens in ZX and ZY planes. Both values obtained by the supplier lie between the resulting average values in this study. The maximum found value is 41.8% higher than the maximum value obtained by supplier. However, this maximum value is from C1V2 specimens that withstood unusual low stress compared to other C specimens.

Graph 2 - Average strain at break values.

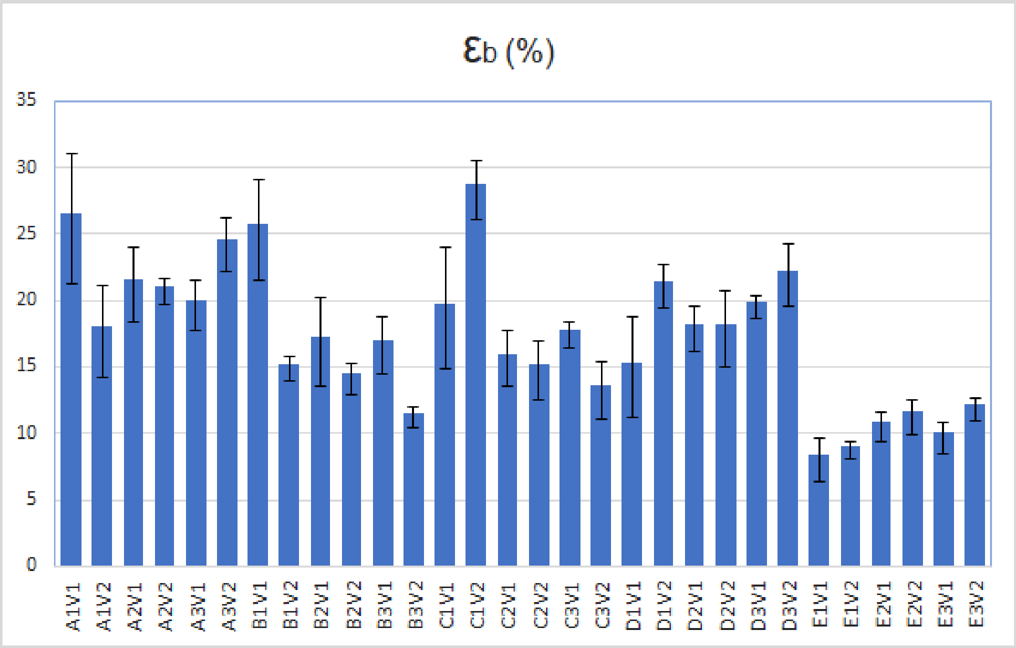

Source: author.

As expected, specimens from A to C showed the opposite behaviour for strain, when compared to stress. In general, the ones that had higher stress values resulted in lower strain values. Therefore, strain tends to decrease from X to Z orientation, the same trend observed by Palma et al. (2019), where it was reported 23.2% and 17.4% strain at break for specimens along X and Z axes, respectively. In O'Connor, Dickson, and Dowling (2018), specimens along X and Z axes, followed this trend with 19% and 16%, respectively. However, specimens along the Y axis had the highest average value for strain at break, with 27%. In this study, specimens oriented along the Y axis had slightly lower strain values than the ones along the Z axis. Given that C1V1, and specially C1V2, did not withstand high stress, it is possible to observe higher values for strain than expected for this orientation.

Contrary to the trend, D specimens presented considerably high strain values, even though they also withstood high stress values. This fact contradicts the expected result for specimens that reached the highest tensile strength, especially considering that D3V2 had the fifth highest average value of 21.88% strain at break. Normally, specimens with high tensile strength display low strain values, because they have stronger bonds between molecule chains, preventing deformation of the material. In addition to low stress values, E specimens had again an inferior mechanical performance, with the lowest values of strain.

The third bar chart represents average values for modulus of elasticity. These values were calculated from the stress-strain curves plotted for each specimen. Calculated values varied from 1,539.76 MPa to 1,936.12 MPa, which represents an increase of 25.74% from the lowest to the highest average value.

Graph 3 - Average values for modulus of elasticity.

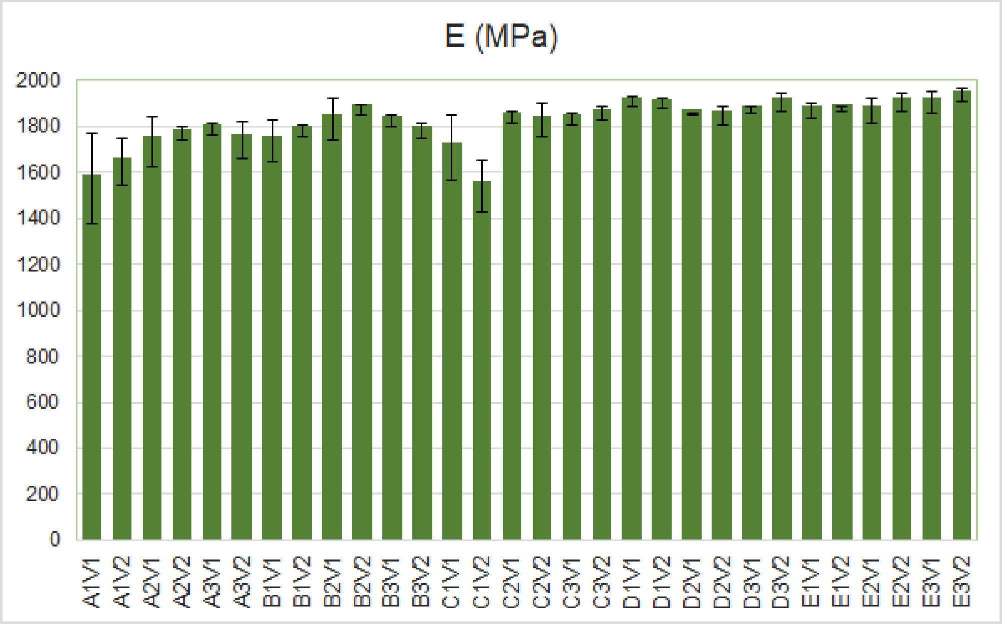

Source: author.

The modulus of elasticity reported by HP was 1,800 MPa, which is 16.9% higher than the minimum average value and 7% lower than the maximum average value found in this study. Hence, it is possible to observe an increase of 7.56% from E3V2 specimens average results compared with the result from supplier. Specimens from D3V2 had also a similar performance, with a modulus of elasticity value of 1,900.24 MPa, which represents an increase of 5.56%, compared with supplier's value. However, E3V2 specimens failed at low strain values, while D3V2 had good results for both stress and strain.

O'Connor, Dickson, and Dowling (2018), evaluated the tensile modulus of specimens printed along X, Y and Z axes, which resulted respectively in 1,242, 1,147 and 1,246 MPa. Their specimens along Y axis had a slightly lower modulus of elasticity than the other two directions. Whereas in this study, the modulus increases from A to E orientations, with a few exceptions, and the values varied considerably more. The lowest and highest average values found are respectively 23.57% and 55.38% higher than their highest value.

The behaviour of E specimens can possibly be explained by its resulting modulus of elasticity, that were among the highest values. A high elastic modulus is related to more brittle materials that display low values for both stress and strain. Polymers tend to be more brittle under its T_g (ASKELAND; FULAY; WRIGHT, 2010).

The layers inside parts are deposited horizontally but since specimens are inclined at 45 degrees, so are their layers. Since it was the only orientation to display these results for all its samples, this printing position likely results in more fragile parts. As it can be observed in figure 24, E1V2 specimens failed without much elongation, and lost pieces of material from the fracture surface, indicating fragile parts.

Figure 24 - E1V2 specimens after tensile testing.

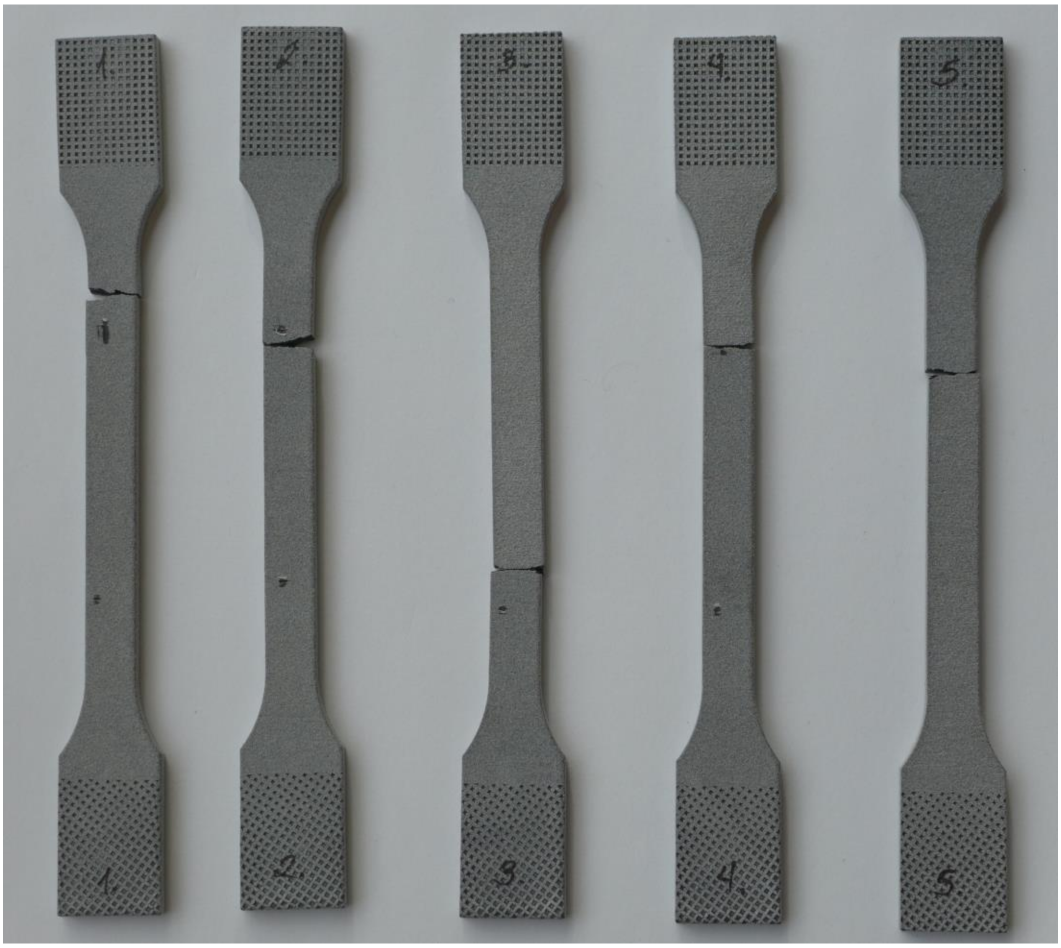

Source: Laboratory of prototype technologies and processes, 2019.

The yield strength was defined with an offset strain value of 0.2%, for each specimen’s stress-strain curve. Resulting average values varied from 27.86 MPa to 36.42 MPa, which represents an increase of 30.72% from the lowest to the highest value. The supplier HP does not have information about yield strength value.

Graph 4 - Average yield strength values.

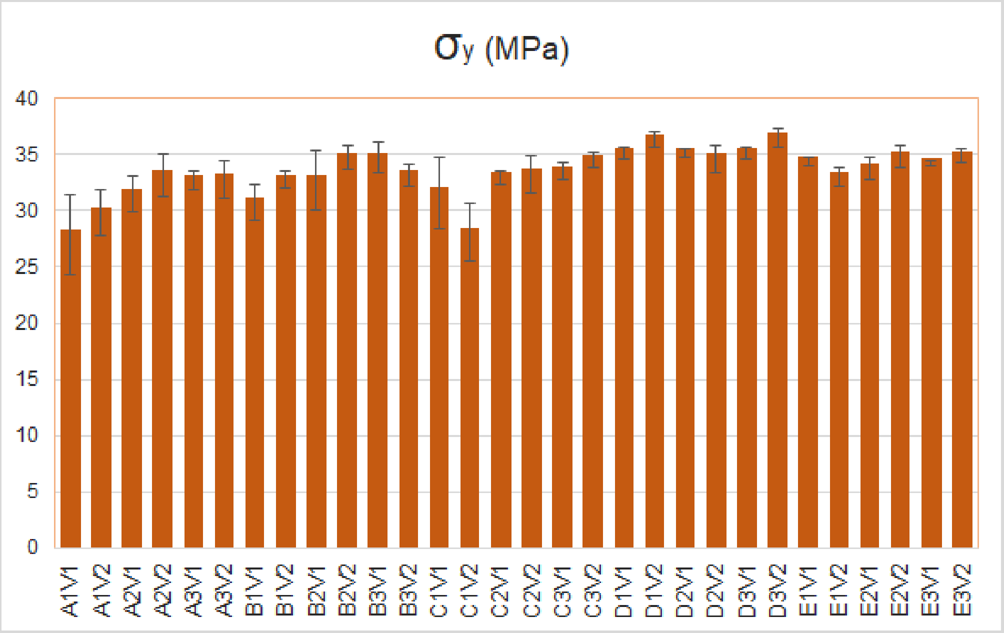

Source: author.

According to Rohde-Liebenau (1999), the value for extruded PA12 yield strength is 46 MPa. Hence traditional manufacturing methods, like extrusion have 26.3% higher yield strength value than the highest average value found in this study for MJF. In this Polymer Data Handbook (1999), there are listed as well values for tensile modulus and strain at break, which are 1,450 MPa and more than 200%. Comparing these values with the ones found in this study, printed specimens have higher modulus but are less ductile than extruded parts.

Graph 5 represents average values for ductility. This property follows the similar trend observed for strain at break results, but its calculation disconsidered the elastic deformation contribution. Hence, results for ductility are smaller, and represent specimens after the elastic deformation was recovered. The resulting average values varied from 5.96% to 26.34%, which represents an increase of 341.94% from the lowest to the highest value.

Graph 5 - Average values for ductility.

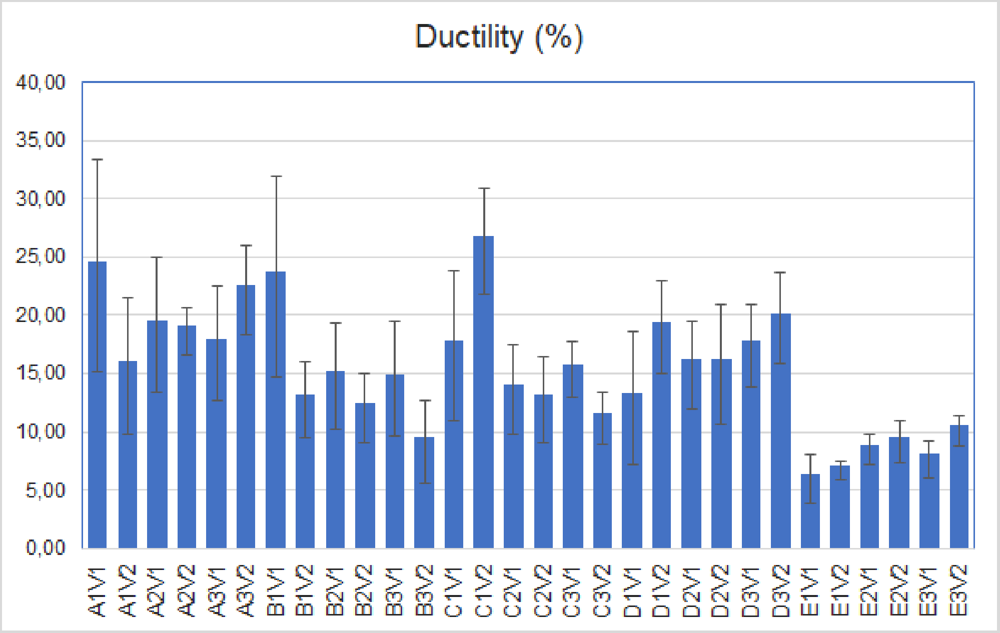

Source: author.

Table 7 displays the comparison of mechanical properties found in literature from three references, with the maximum and minimum values obtained in this study with their respective orientations.

Table 7 - Comparison of resulting properties values with literature.

References	Details	σm (MPa)	εb (%)	E (MPa)	σy (MPa)	Ductility (%)
Polymer Data Handbook	Extruded	-	>200	1,450	46	-
Palma et. al (2019)	Horizontal	45.15*	23.2	-	-	-
	Vertical	47.77*	17.4	-	-	-
O'Connor, Dickson, and Dowling (2018)	Along X	47	19	1,242	-	-
	Along Y	48	27	1,147	-	-
	Along Z	49	16	1,246	-	-
Author	Maximum	55.1 (D3V2)	28.36 (C1V2)	1,936.12 (E3V2)	36.42 (D3V2)	26.34 (C1V2)
	Minimum	49.84 (A1V1)	8 (E1V1)	1,539.76 (C1V2)	27.86 (A1V1)	5.96 (E1V1)

*Fracture stress = maximum stress

Source: author.

The engineering stress-strain curves for the five samples in each printing orientation were gathered in one graph. This arrangement resulted in thirty graphs. The first graph representing curves for specimens of A1V1 orientation, and D3V2 graph can be observed in the following figures. Remaining graphs for other thirteen orientations can be found in appendix B section. Generally, specimens behaved similarly for each orientation, with more significant differences regarding the strain values at break, whereas stress values did not vary as much.

Figure 25 - Stress-strain curves for A1V1 specimens.

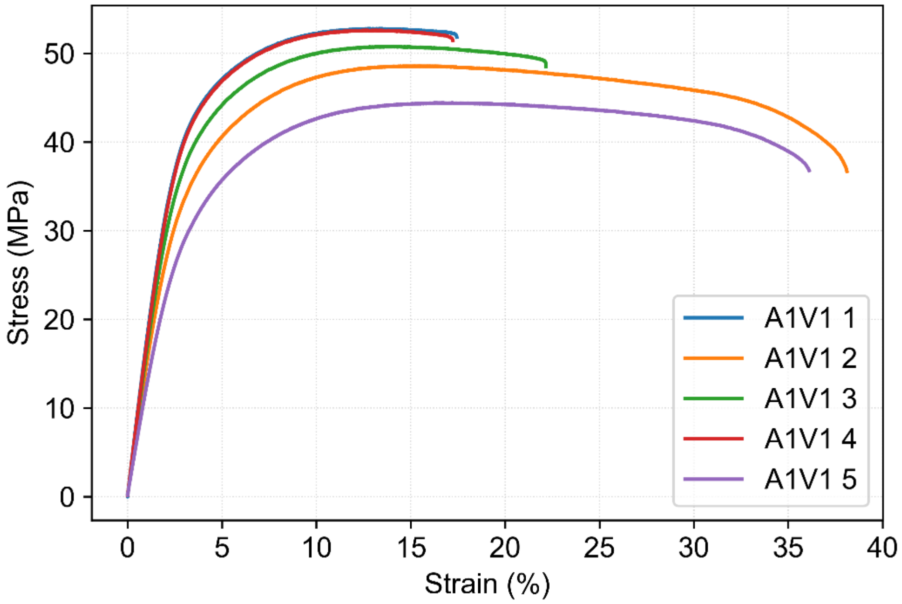

Source: author.

According to curves images, specimens in A1V1 orientation had substantially variation in strain values, and it was the orientation with the biggest standard deviation for maximum stress and strain at break. As it can be observed in figure 26, two samples were more ductile and had a lot of elongation until break, especially sample 2 with 38.1% of strain at break, and sample 5 with 36.1%. They also developed necking near the fracture. The other three samples, 1, 3 and 4 were more brittle, withstood higher stress values, but lower strain at break values, with 17.4%, 22.2% and 17.2%, respectively.

Figure 26 - A1V1 specimens after tensile testing.

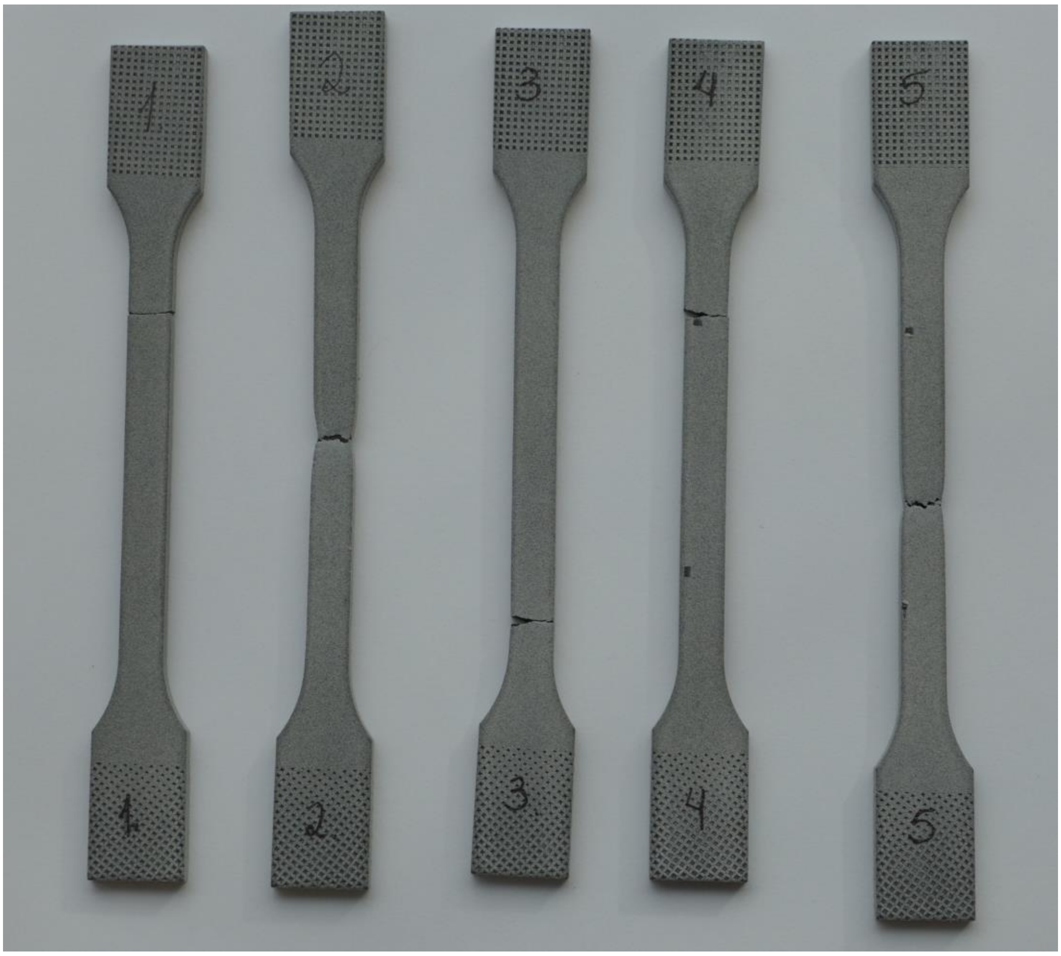

Source: Laboratory of prototype technologies and processes, 2019.

Figure 27 shows the engineering stress-strain curves from specimens of D3V2 orientation.

Figure 27 - Stress-strain curves for D3V2 specimens.

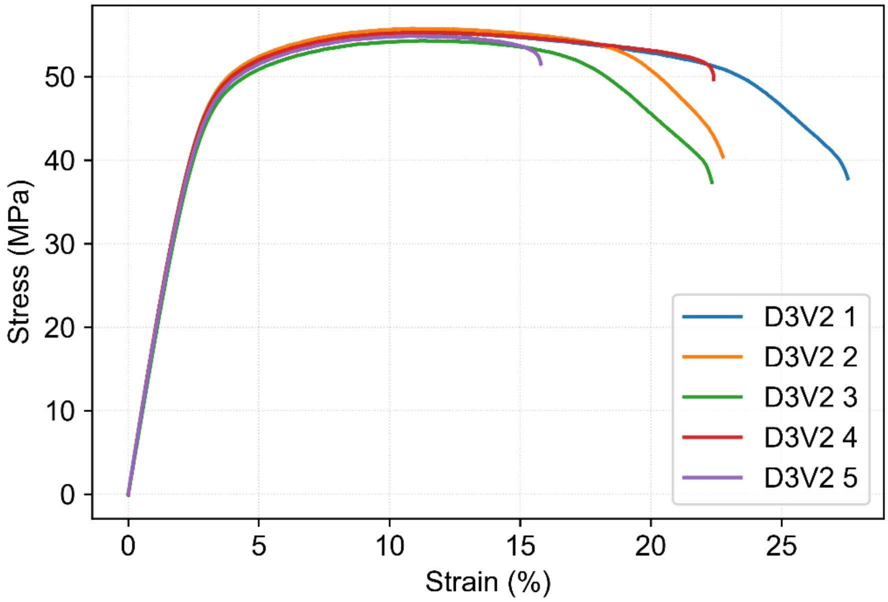

Source: author.

Specimens in D3V2 orientation had very similar curves for all five samples almost up to maximum stress values. After this point samples displayed different performances and higher variation of strain at break. Nevertheless, specimens from this orientation had a good performance for both stress and strain, with the highest average value for maximum stress, and the fifth highest average for strain at break.

As it can be observed in figure 28, for all five samples printed in D orientation fractured after necking occurred. The decrease in stress observed in curves is probably related to this fact, as explained in Askeland, Fulay, and Wright (2010). Hence, all specimens displayed a more ductile behaviour.

Figure 28 - D3V2 specimens after tensile testing.

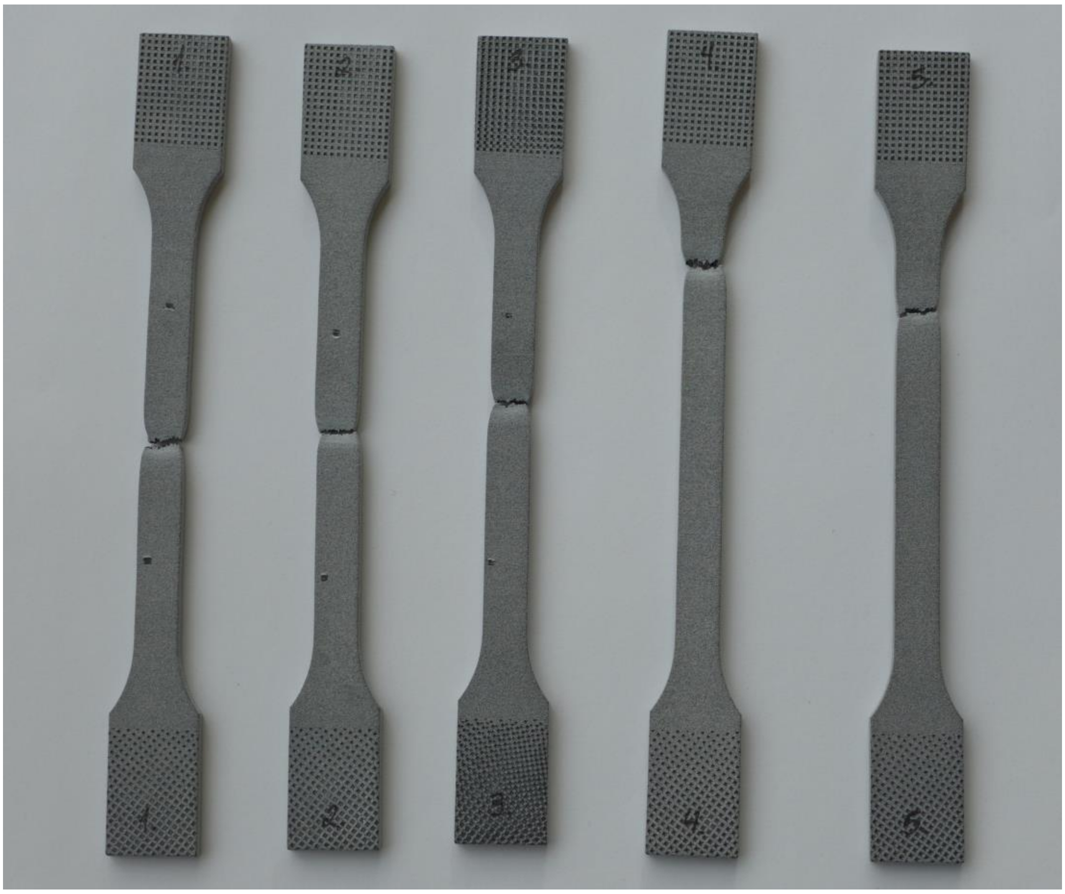

Source: Laboratory of prototype technologies and processes, 2019.

4.2 Lattice structures

Three types of lattice structures were submitted to tensile testing, resulting in force and displacement values for each sample. However, given the complexity of their geometry, different cross-sectional areas are found along the length of structures. This condition makes it difficult to determine the initial cross-sectional area, needed in order to obtain engineering stress-strain curves. Hence, it was evaluated the results of specimens regarding force and displacement values only. In this manner, it was plotted force versus displacement curves, that can be found in the section of appendix C. These data were organized as well in bar graph containing average values for maximal force and average displacement at break, from each structure at the same percentage of volume fill but for different orientations. Furthermore, two bar graphs were plotted for comparison between different structures at 25% and 50%, with the same orientation A0°. Figure 29 illustrates printed tensile test specimens with different lattice structures before testing.

Figure 29 - Tensile test specimens with lattice structures.

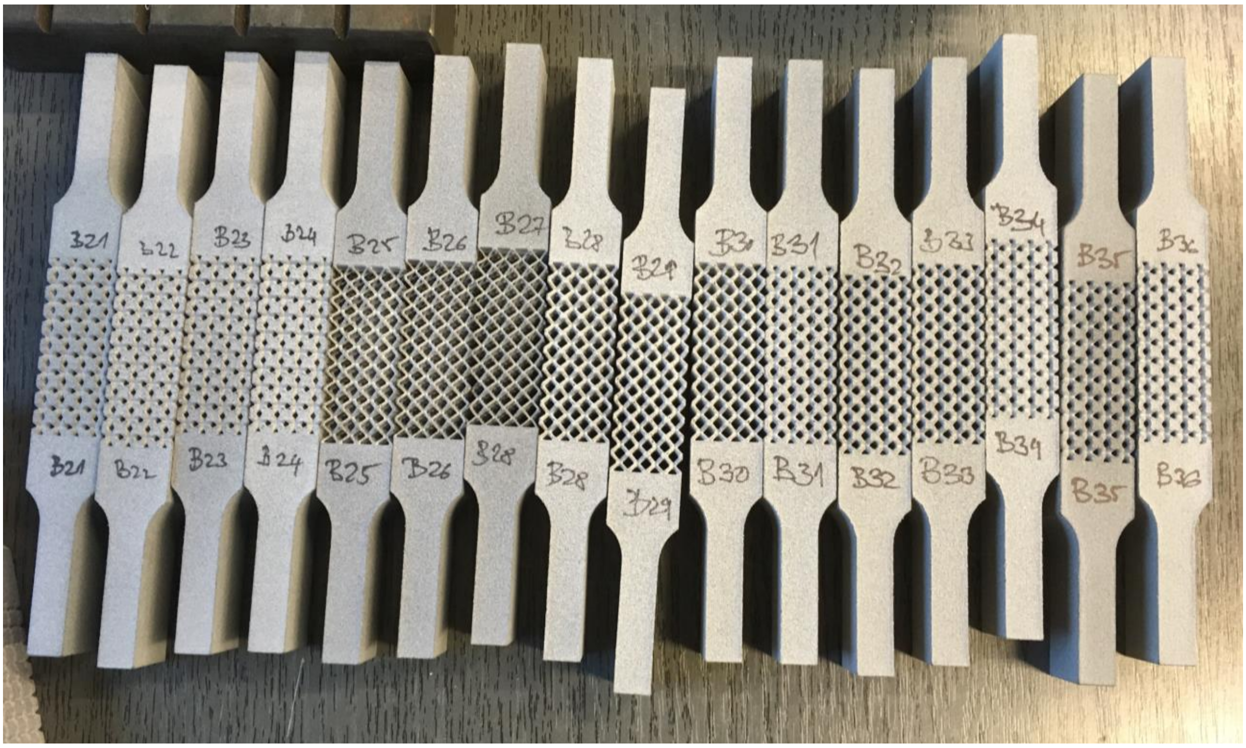

Source: Laboratory of prototype technologies and processes, 2019.

In the figure 30, is possible to observe an Octet lattice structure specimen, fractured after the tensile test was performed.

Figure 30 - Tensile specimen after test.

Source: Laboratory of prototype technologies and processes, 2019.

All Cross specimens were tested in the same three orientations A0°, B45°, and B90°, regardless of their percentage of volume occupied by material.

The first bar graph for maximal force and displacement at break average values, was made for samples of Cross structure with 10% of volume filled by material. Their resulting values are compared in the graph 6.

Graph 6 - Force and displacement values for Cross 10% specimens.

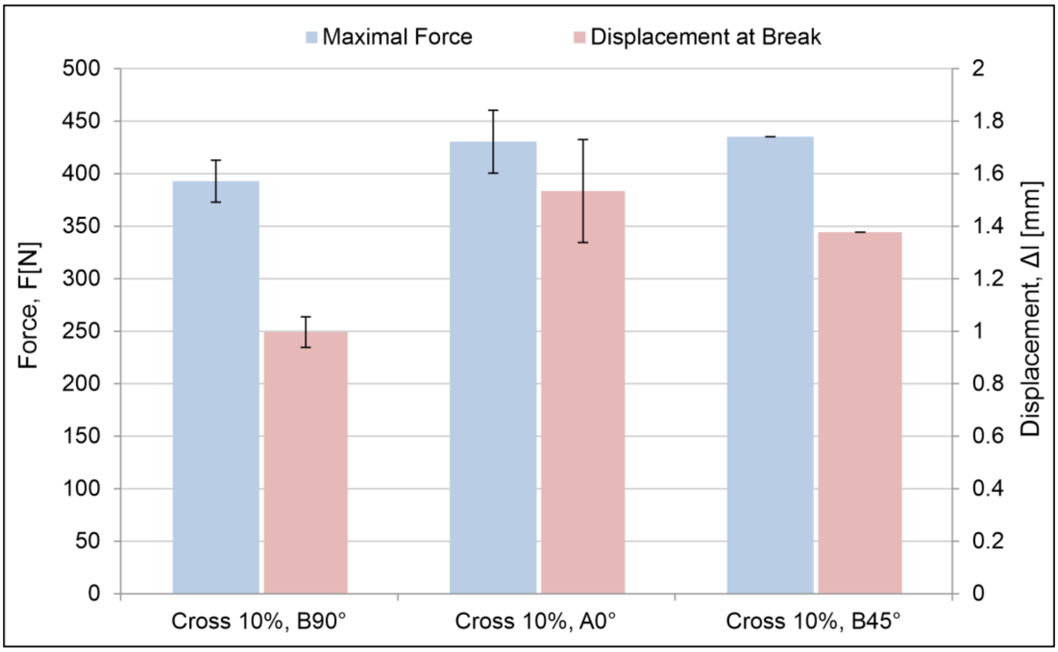

Source: Laboratory of prototype technologies and processes, 2019.

It is possible to observe in graph 6 that results for maximal average force increase from B90° to B45°, with A0° results being intermediate. Thus, regarding force the specimen in B45° orientation can withstand a higher value, but have a similar result with specimens from A0° orientation. However, when considering displacement results, specimens in A0° orientation had an increase of 7.14% compared to specimen in B45°. While specimens in B90° orientation displayed an inferior performance for both force and displacement. This percentage of volume filling had the lowest values between Cross structures, for both parameters.

Graph 7 displays the average values of maximum force and displacement at break for Cross 25% specimens. Their resulting values are compared for different orientations.

Graph 7 - Force and displacement values for Cross 25% specimens.

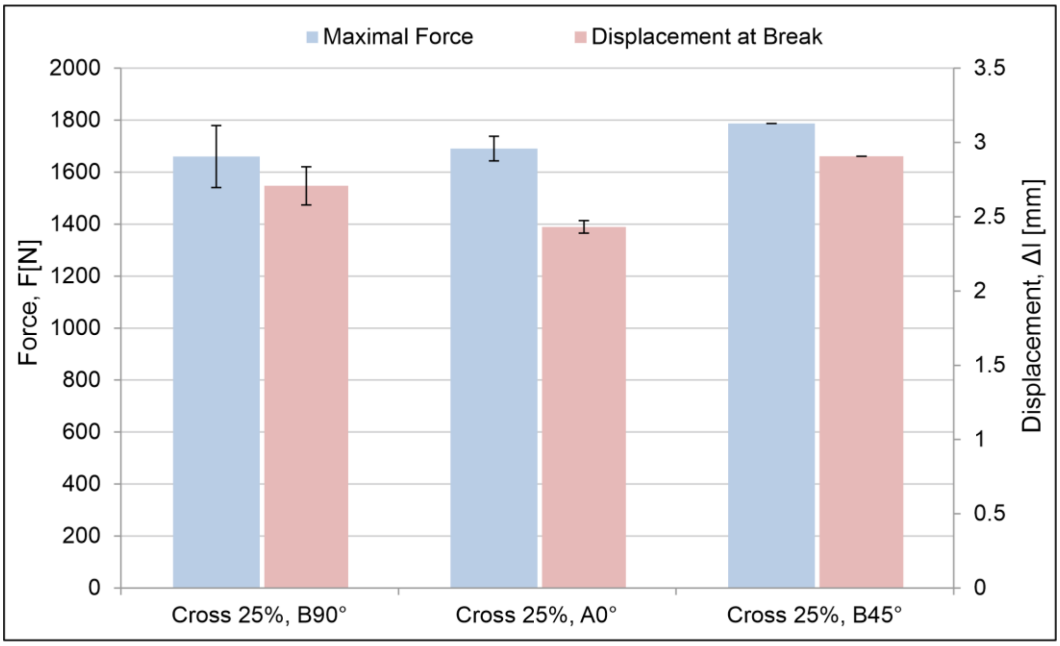

Source: Laboratory of prototype technologies and processes, 2019.

In the case of Cross 25% specimens, it is possible to observe the same comparison for maximal force values between orientations, as the one made for Cross 10%. However, for 25% of occupied volume, A0° and B90° orientations had close values. Furthermore, specimens in B90° orientation had higher average displacement values than A0° specimens.

Graph 8 displays the average values of maximum force and displacement at break for Cross 50% specimens, and their resulting values are shown for different orientations.

Graph 8 - Force and displacement values for Cross 50% specimens.

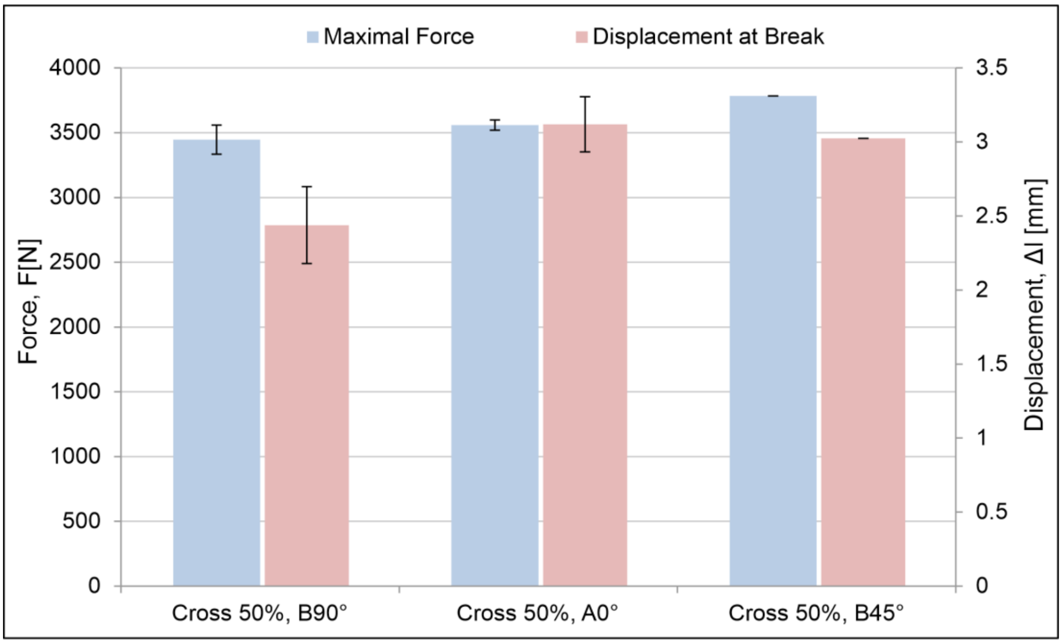

Source: Laboratory of prototype technologies and processes, 2019.

In the case of Cross 50%, specimens have the exact same comparison between results as the one made for Cross 10%. However, the range of values for Cross 50% is much higher than Cross 10%, for both parameters, with a maximum force of 3,750 N, and 3.15 mm of displacement. While Cross 10% results did not surpass 450 N and 1.55 mm, respectively for force and displacement.

Graph 9 displays the average values of maximum force and displacement at break for Cross 70% specimens, and their resulting values are shown for different orientations.

Graph 9 - Force and displacement values for Cross 70% specimens.

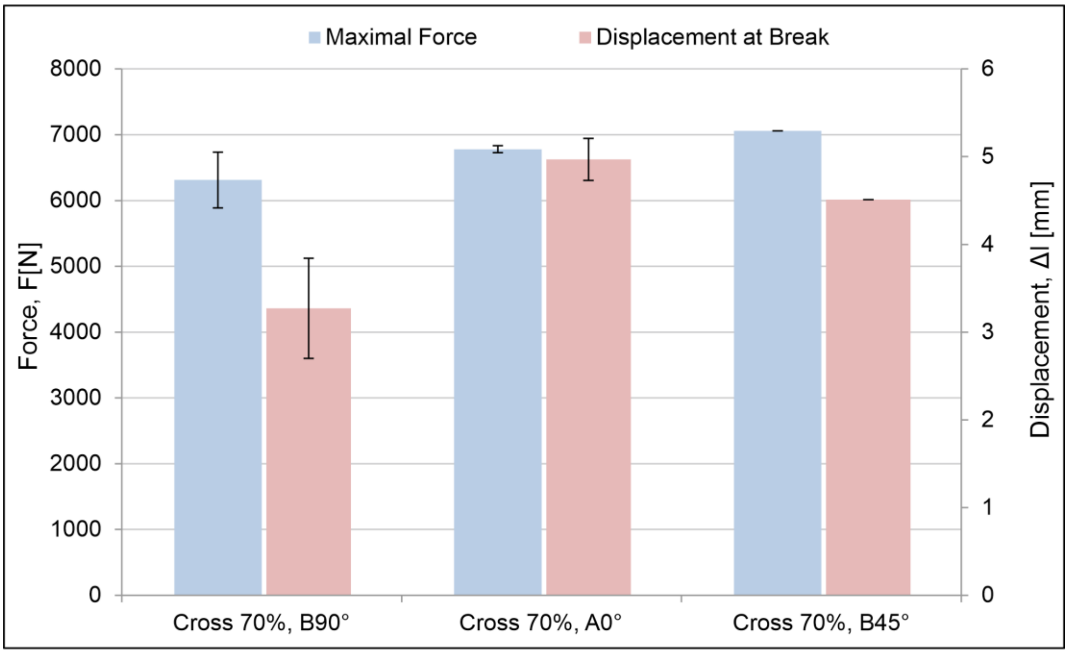

Source: Laboratory of prototype technologies and processes, 2019.

For Cross 70%, once again values for maximal average force increased from B90° to B45°, while A0° was intermediate. As well, values for average displacement at break were higher for A0°, and lower for B90°. As expected, results for Cross 70%, with the highest percentage of volume filled by material, achieved the highest results between all Cross structures, with maximal force a little over 7,000 N, and 5 mm of displacement at break.

All Cross specimens had higher values of average maximal force for B45° orientation. While for average displacement at break A0° orientation had the best results in most percentages, except for Cross 25%.

All BCC specimens were tested in the same three orientations A0°, A45°C-90°, and B90°, regardless of their percentage of volume occupied by material. Graph 10 displays the average values of maximum force and displacement at break for BCC 10% specimens. Their resulting values are compared for different orientations.

Graph 10 - Force and displacement values for BCC 10% specimens.

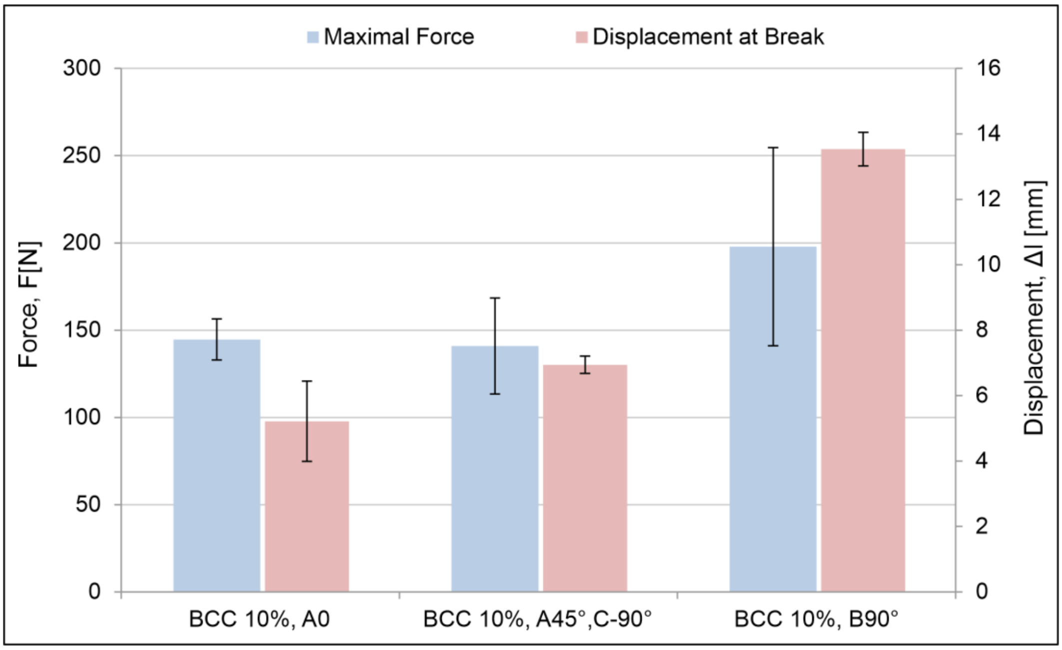

Source: Laboratory of prototype technologies and processes, 2019.

In the case of BCC 10%, the B90° orientation specimens had the highest values for both parameters. Followed by A0° and A45°C-90°, regarding maximal force. The opposite happened for displacement at break results, A45°C-90° specimens had a higher result than A0°.

Graph 11 displays the average values of maximum force and displacement at break for BCC 25% specimens. Their resulting values are compared for the different orientations tested.

Graph 11 - Force and displacement values for BCC 25% specimens.

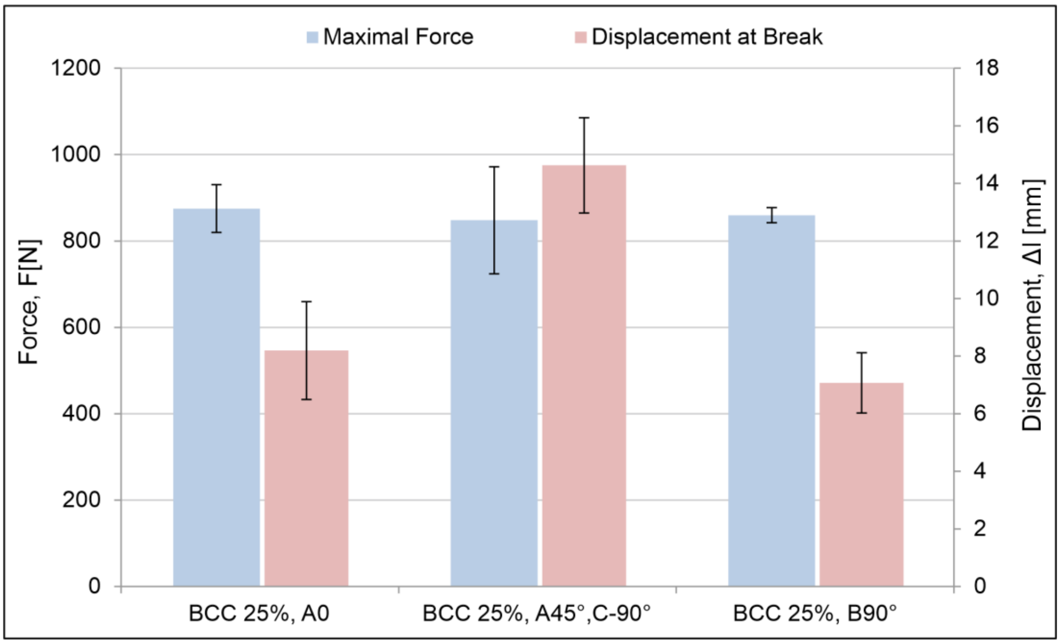

Source: Laboratory of prototype technologies and processes, 2019.

BCC 25% specimens had similar results for maximal average force, with A0° orientation having the highest value. Regarding results for average displacement at break, A45°C-90° orientation had a much higher value than the other two orientations.

Graph 12 displays the average values of maximum force and displacement at break for BCC 50% specimens. Their results are compared for the three orientations tested.

Graph 12 - Force and displacement values for BCC 50% specimens.

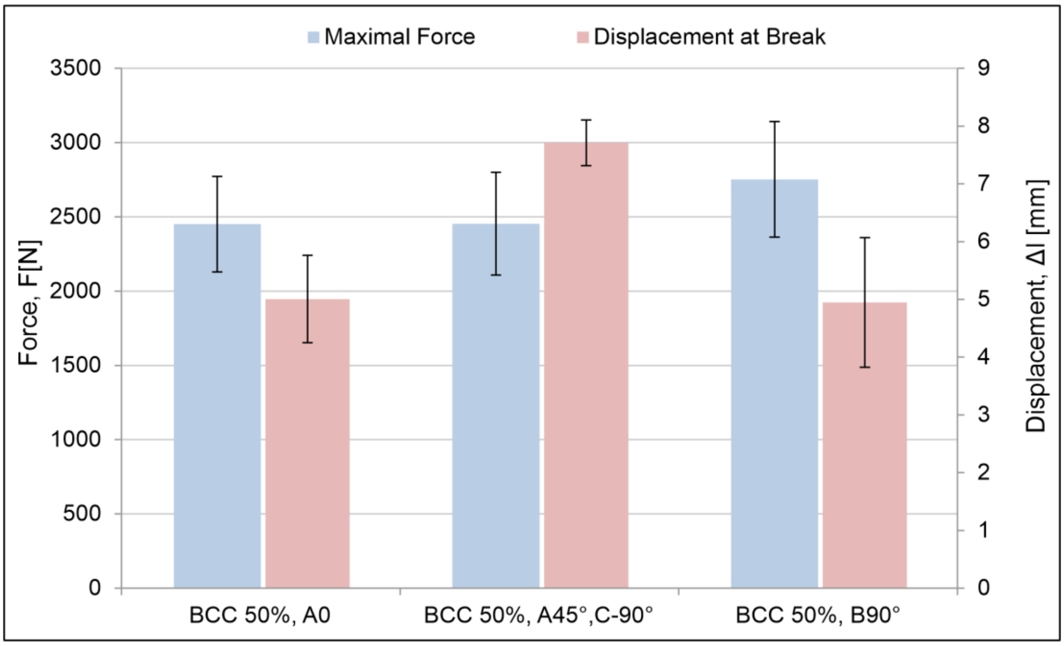

Source: Laboratory of prototype technologies and processes, 2019.

For BCC 50% specimens the B90° orientation had the highest value for average maximal force, but also had the lowest results for displacement at break. In the opposite manner, A45°C-90° specimens had the lowest average results for maximal force, the exact same as A0° specimens, and the highest for displacement at break. While A0° specimens had the intermediate result for displacement at break.

Graph 13 displays the average values of maximum force and displacement at break for BCC 70% specimens. Their results are compared for the different orientations tested.

Graph 13 - Force and displacement values for BCC 70% specimens.

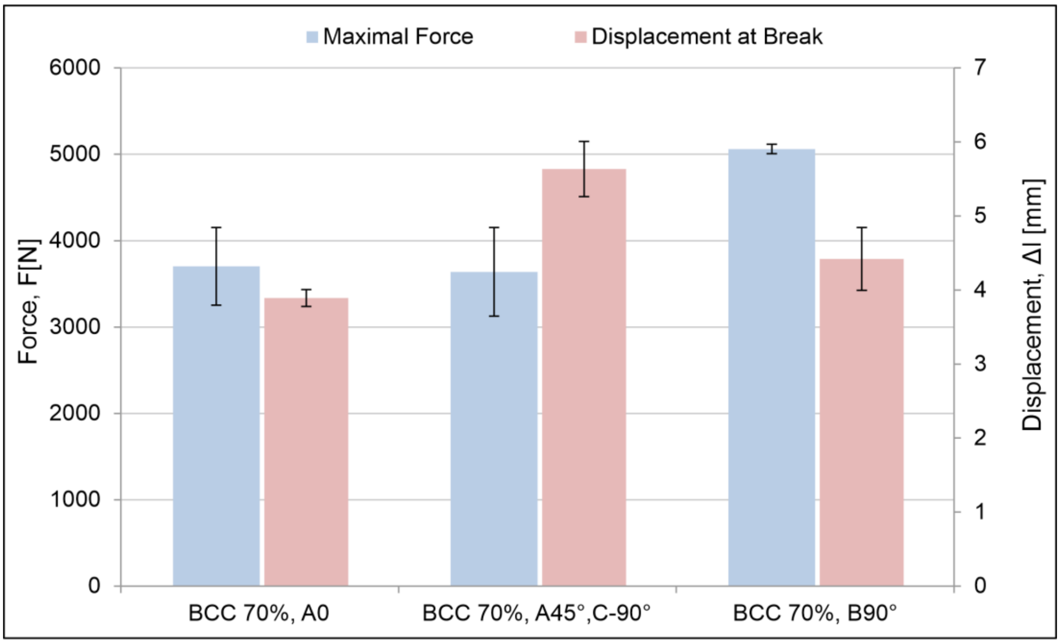

Source: Laboratory of prototype technologies and processes, 2019.

BCC 70% specimens have a similar comparison between results as the one made for BCC 50%. In this case, A45°C-90° specimens had the lowest and highest results for maximal force and displacement at break, respectively. While the B90° orientation had the highest results for force, and intermediate result for displacement. A0° specimens had intermediate average result for maximal force and the lowest for displacement at break.

BCC specimens had in general the highest results for average maximal force in B90° orientation, except for BCC 25%. Likewise, they had the highest results for average displacement at break for A45°C-90°, except in the case of BCC 10% specimens. Once again, results for BCC 70%, the highest percentage of volume filled by material, achieved the highest result for maximal force between all BCC structures, with a value a little over 5,000 N. However, for displacement at break BCC 25% had the highest result, a little over 14 mm, representing an increase of 163% compared to the highest value reached by BCC 70%.

All Octet specimens were tested in two orientations A0° and B45°, with two percentages of volume occupied by material, 25% and 50%. Graph 14 displays the average values of maximum force and displacement at break for Octet 25% specimens. Their resulting values are compared for the two orientations tested.

Graph 14 - Force and displacement values for Octet 25% specimens.

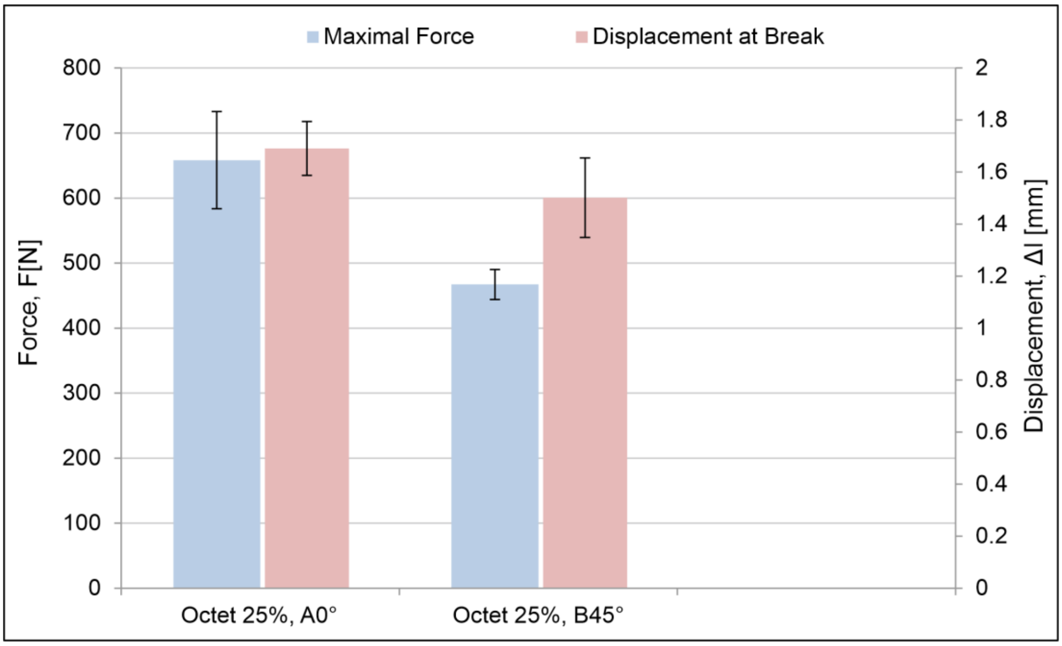

Source: Laboratory of prototype technologies and processes, 2019.

In the case of Octet 25%, specimens in A0° orientation had better results for both maximal force and displacement at break, than B45° orientation.

Graph 15 illustrates the average values of maximum force and displacement at break for Octet 50% specimens. Their resulting values are compared for the two orientations tested.

Graph 15 - Force and displacement values for Octet 50% specimens.

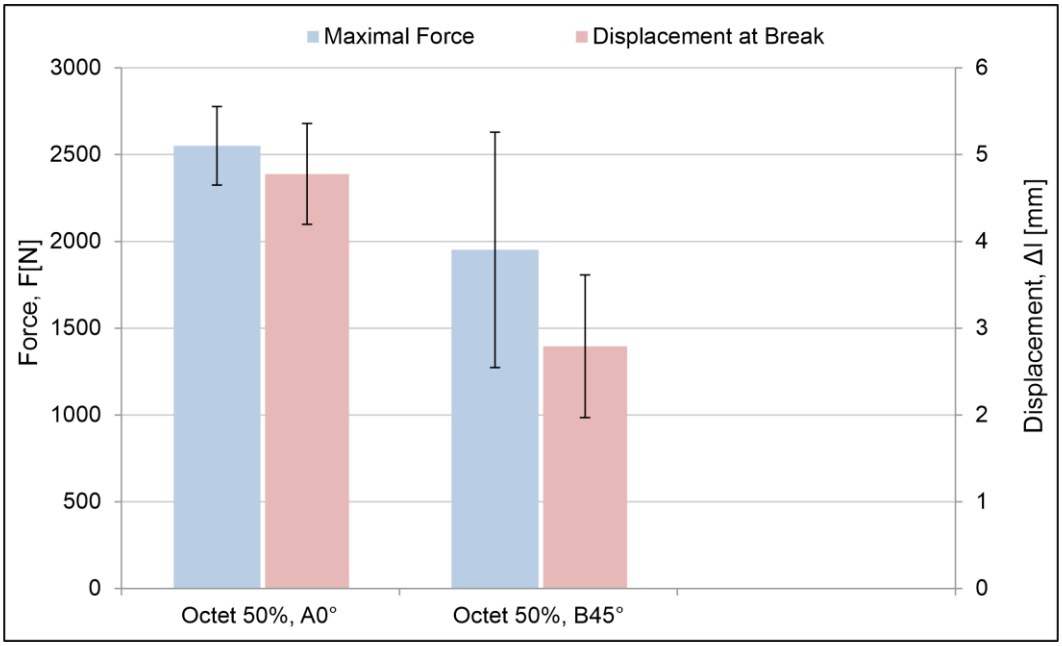

Source: Laboratory of prototype technologies and processes, 2019.

Specimens from Octet 50% had as well better results in A0° orientation for average maximal force and displacement at break, than specimens in B45° orientation. Consequently, all Octet specimens had the highest results for average maximal force and displacement at break in A0° orientation. As expected, Octet 50%, which has the highest percentage of volume filled by material, had the highest results between the two Octet structures, with maximal force a little over 2,500 N, and 4.75 mm of displacement at break.

Graph 16 illustrates the comparison of Cross, BCC and Octet structures, at 25% of the volume occupied by material, and with A0° printing orientation.

Graph 16 - Comparison of structures at 25% and A0° orientation.

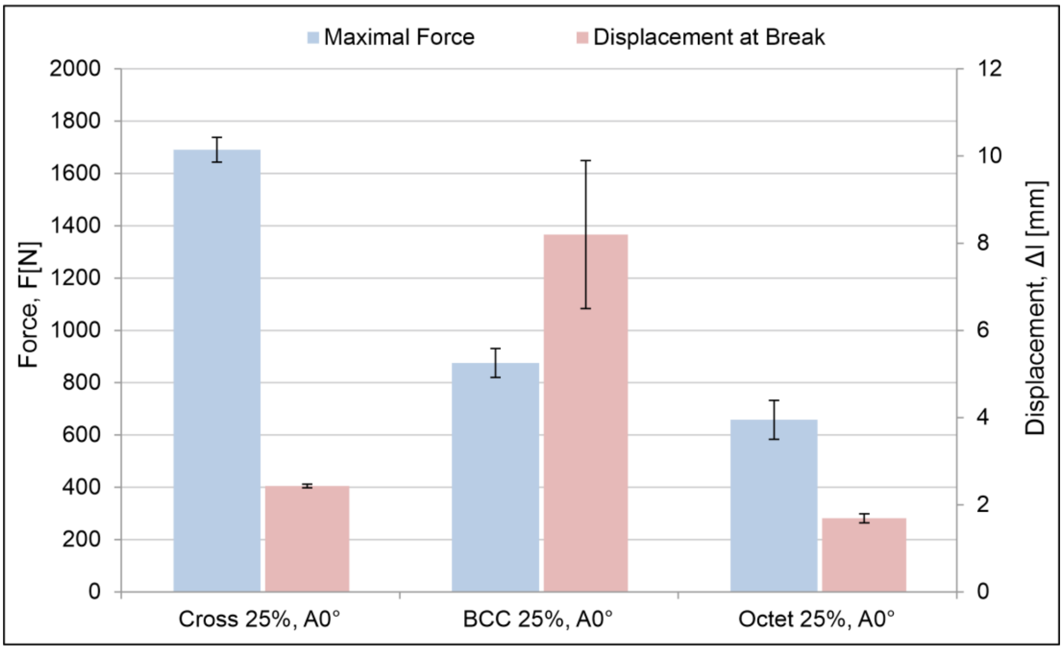

Source: Laboratory of prototype technologies and processes, 2019.

The comparison of structures with 25% of occupied volume indicates that Cross structure have a much higher result for maximal force than the other two structures. Compared with the lowest value of Octet 25%, it shows an increase of 142%. It shows an intermediate result for displacement at break. While BCC 25% had the highest result for displacement at break, and Octet 25% the lowest results for both parameters.

Graph 17 displays the comparison of Cross, BCC and Octet structures, at 50% of the volume occupied by material, and with A0° printing orientation.

Graph 17 - Comparison of structures at 50% and A0° orientation.

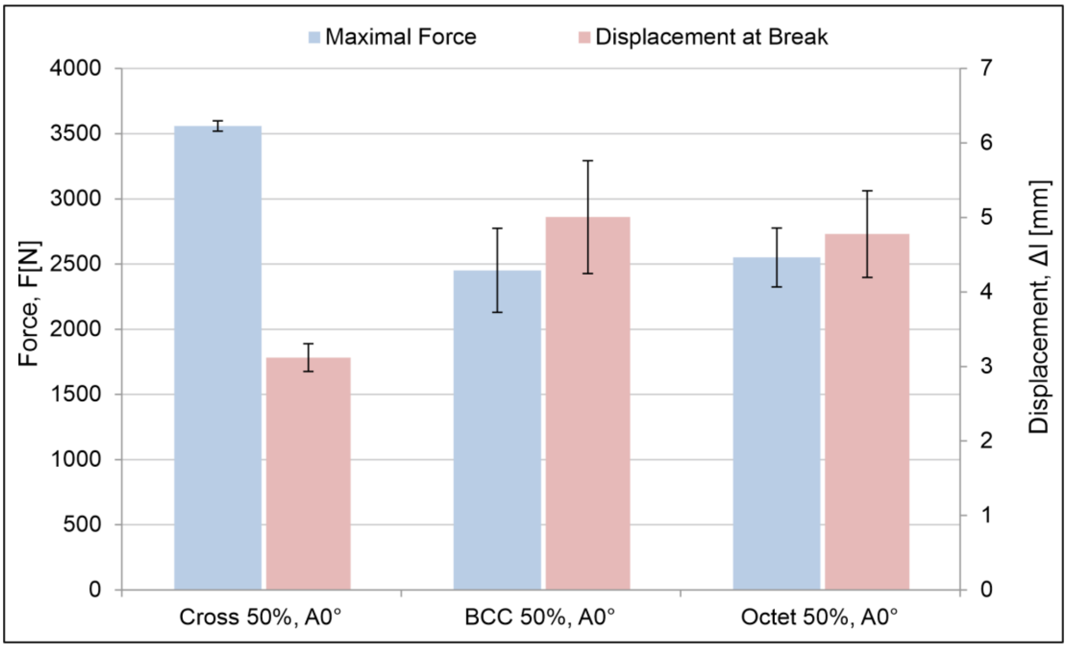

Source: Laboratory of prototype technologies and processes, 2019.

In the case of specimens with 50%, the Cross structure had as well the highest result for maximal force, with an increase of 59%, if compared to the lowest value displayed by BCC 50%. However, it also had the lowest result for displacement at break. While the Octet structure had intermediate results for both parameters. The BCC structure had again the highest value for displacement at break.

The comparison of average maximal force values from graph 16 and 17, enables to observe, as expected, that the larger the percentage of volume occupied by material the higher force is withstood by these lattice structures. Apart from BCC 50%, the same fact can be observed for displacement at break values, where the larger the percentage of volume occupied by material the higher displacement at break values are obtained.

Wang et al. (2019), analysed BCC and Octet (FCC in their study) under compression load, for structures with rod diameter of 0.8 mm. They found that the Octet structure, compared to BCC, had the highest results for all properties analysed in experiment and simulation. In this study, the structures with closest diameter values to 0.8 mm are BCC 10% and Octet 25%, which have diameters of 0.73074 mm and 0.76344 mm, respectively. It is possible to observe that Octet 25% A0° had higher results for maximum force, but lower results for displacement than BCC 10% A0°. However, this comparison only considers rod diameter values, and not the apparent density, since Octet 25% has higher mass and volume values, this outcome is expected for maximum force. Therefore, it is possible to rely on the two comparison made previously between BCC 25% and Octet 25%, and between BCC 50% and Octet 50%, where the volume for both parts are the same. In summary, the Octet structure made with PA12, under tension loading only had higher average maximal force for 50% of occupied volume, whereas regarding average displacement at break, the Octet had lower results for both percentages.

In summary, the Cross structure had the highest result for maximal force, in both percentages analysed, compared to BCC and Octet. While the BCC structure had the highest result for displacement at break in both cases.

5. Conclusions

MJF can produce parts with good mechanical properties, comparable with traditional manufacturing methods. It allows a small series production of final parts, in addition to prototyping.

The printing orientation used for parts influences the resulting mechanical properties, especially regarding strain at break values where the variation was more significant. However, when aiming to obtain stronger parts, the tensile strength, the modulus of elasticity, and the yield strength are properties that should be considered. In that manner, specimens from D3V2 orientation had considerably higher results for these properties, as well as for strain at break and ductility. These results indicate that D3V2 could enable parts with higher strength, and more ductile if needed. Conversely specimens from E orientation displayed inferior mechanical properties, which would lead to more brittle parts with lower tensile strength. Generally, results for printing orientations are corresponding with the ones found in literature, from other studies and HP’s data, and with a few improvements.

The analysis of three lattice structures shows differences in their results of mechanical tests. The Cross structure had the highest average result for maximal force, compared to other structures in 25% and 50% of the volume occupied by material, and in A0° orientation. Regarding displacement at break evaluated in the same situation, the BCC structure had the highest average result. Moreover, as expected for all structures, the larger the percentage of volume occupied by material the higher the force that is withstood by these lattice structures. The same results were observed for displacement at break values, with the exception of BCC 50%.

Considering that MJF is a recent technology it can benefit from more related research, especially regarding lattice structures in which additional geometries can be studied. Furthermore, for any kind of manufactured parts, it is also possible to continue the analysis of resulting mechanical properties, regarding the influence of different mixing proportion of used and new powder.

References

3DPRINTING.COM. HP Launches 3D Printers with Multi Jet Fusion™ Technology. May, 2016. Available at: <https://3dprinting.com/3dprinters/hp-launches-3d-printers-with-multi-jet-fusion-technology>. Accessed at: 12/08/2019.

ARAUJO, L. P. S de. **Análise Da Rigidez De Estruturas Lattice e Avaliação De Seu Uso Como Núcleo De Estruturas Sanduíche.** 2018. 96 f. Trabalho de conclusão de curso - Escola Politécnica, Departamento de engenharia mecânica, Universidade Federal do Rio de Janeiro, Rio de Janeiro, 2018.

ASKELAND, D. R.; FULAY, P. P.; WRIGHT, W. J. **The science and engineering of materials**. Sixth edition. Stanford: Cengage Learning, 2010.

ASKELAND, D. R.; FULAY, P. P; BHATTACHARYA, D. K (Editor). **Essentials of Materials Science and Engineering.** Second edition, SI. Stanford: Cengage Learning, 2009.

ASTM F2792-12a, **Standard Terminology for Additive Manufacturing Technologies** (Withdrawn 2015), ASTM International, West Conshohocken, PA, 2012.

BMW Group. A million printed components in just ten years: BMW Group makes increasing use of 3D printing, November, 2018. Available at: <https://www.press.bmwgroup.com/global/article/detail/T0286895EN/a-million-printed-components-in-just-ten-years:-bmw-group-makes-increasing-use-of-3d-printing?language=en> Accessed at: 30/09/2019.

DOWNLING, N. E. **Mechanical Behaviour of Materials. Engineering Methods for Deformation, Fracture, and Fatigue.** Third edition, New Jersey: Pearson Prentice Hall, 2006.

DUPONT. 1939 Dr. Wallace Carothers discovers Nylon. Available at: <http://www.dupont.com/corporate-functions/our-company/dupont-history.html>. Accessed at: 27/06/2019.

FORBES. Wohlers Report 2018: 3D Printer Industry Tops $7 Billion. June, 2018. Available at: <https://www.forbes.com/sites/tjmccue/2018/06/04/wohlers-report-2018-3d-printer-industry-rises-21-percent-to-over-7-billion/?fbclid=IwAR1fQNZNIuJJuUGWTyo3pjJ_wFcE_ZJhYooGZRGdCEAYbPuwTYjzH9xTlDA#38ecd9202d1a>. Accessed at: 20/10/2019.

GIBSON, I.; ROSEN, D.; STUCKER, B. **Additive Manufacturing technologies**: **3D Printing, Rapid Prototyping, and Direct Digital Manufacturing**. Second edition. New York: Springer, 2015.

GORGULUARSLAN, R. M.; PARK, S.; ROSEN, D. W.; CHOI, S. A Multilevel Upscaling Method for Material Characterization of Additively Manufactured Part Under Uncertainties. **Journal of Mechanical Design**, Volume 137, 2015.

HP DEVELOPMENT COMPANY, L.P. HP 3D Applications, 2019. Available at: <https://www8.hp.com/us/en/printers/3d-printers/3dapplications.html>. Accessed at: 30/09/2019.

HP DEVELOPMENT COMPANY, L.P. HP Accelerates 3D Printing Mass Production with New Customers, Applications, and Partners, November, 2018. Available at: <https://press.ext.hp.com/us/en/press-releases/2018/hp-continues-accelerating-3d-printing-industry-to-mass-productio.html> Accessed at: 30/09/2019.

HP DEVELOPMENT COMPANY, L.P. HP Jet Fusion 3D Printing Solutions. Reinventing Prototyping and Manufacturing, November 2017. Available at: <http://www8.hp.com/h20195/v2/GetPDF.aspx/4AA6-4894EEP.pdf>. Accessed at: 12/08/2019.

HP DEVELOPMENT COMPANY, L.P. HP 3D High Reusability PA 12, February 2019. Available at: <http://www8.hp.com/h20195/v2/GetDocument.aspx?docname=4AA6-4895ENA>. Accessed at: 12/08/2019.

HP DEVELOPMENT COMPANY, L.P. Jet Fusion 500/300 series, 2019. Available at: <https://www8.hp.com/us/en/printers/3d-printers/products/multi-jet-fusion-500-300.html>. Accessed at: 30/09/2019.

HP DEVELOPMENT COMPANY, L.P. Technical Guideline for Material Development with HP 3D Open Materials Platform, January 2018. Available at: <http://www8.hp.com/h20195/v2/GetDocument.aspx?docname=4AA6-8315ENW&jumpid=va_1wkf34rz78>. Accessed at: 30/09/2019.

ISO 527-2:2012, **Plastics — Determination of tensile properties — Part 2: Test conditions for moulding and extrusion plastics**, 2012.

Laboratory of prototype technologies and processes. Centre for nanomaterials, Advanced technologies and Innovation. Technical University of Liberec, 2019.

MCKINSEY GLOBAL INSTITUTE. **Disruptive technologies: Advances that will transform life, business, and the global economy.** May 2013.

MOLITCH-HOU, M. Overview of additive manufacturing process. In: ZHANG, J.; JUNG, Y. **Additive Manufacturing: Materials, Processes, Quantifications and Applications.** First edition. Cambridge: Butterworth-Heinemann, 2018.

O'CONNOR, H. J.; DICKSON, A. N.; DOWLING, D. P. Evaluation of the mechanical performance of polymer parts fabricated using a production scale multi jet fusion printing process. **Additive Manufacturing**, volume 22, pages 381-387, 2018.

PALMA, T.; BEHESHTI, A.; DAMASUS, P.; DAVAMI, K.; MUNTHER, M.; SALARI, S. Multiscale mechanical and tribological characterizations of additively manufactured polyamide 12 parts with different print orientations. **Journal of Manufacturing Processes**, Volume 40, pages 76-83, 2019.

RASHED, M. G.; ASHRAF, M.; MINES, R. A. W.; HAZELL, P. J. Metallic microlattice materials: A current state of the art on manufacturing, mechanical properties and applications. **Materials & Design**, Volume 95, pages 518-533, 2016.

RIEDELBAUCH, J.; RIETZEL, D.; WITT, G. Analysis of material aging and the influence on the mechanical properties of polyamide 12 in the Multi Jet Fusion process. **Additive Manufacturing**, Volume 27, pages 259-266, 2019.

ROHDE-LIEBENAU, H. U. W. Nylon 12. In: MARK, J. E. **Polymer Data Handbook**. Oxford University Press, Inc., 1999. pages 225-229.

SCHMID, M; WEGENER, K. Thermal and molecular properties of polymer powders for Selective Laser Sintering (SLS). **AIP Conference Proceedings 1779**, 100003 (2016).

SOUZA, S. A. de. **Ensaios mecânicos de materiais metálicos. Fundamentos teóricos e práticos.** 5ª edição. São Paulo: Edgard Blucher, 1982.

WANG, Y.; JIN, N.; WANG, F.; ZHANG, B.; CHENG, H.; ZHANG, H. Failure and energy absorption characteristics of four lattice structures under dynamic loading. **Materials & Design**, Volume 169, 2019.

WOLFGANG, G.; RUESTEM, D. **Nylon-12-Preparation, Properties, and Applications. Industrial & Engineering Chemistry**, 1970.

Appendix

Appendix A - Lattice structures

Images of all developed structures, Cross, BCC and Octet, in theirs respectives percentages of volume occupied by material. As well as the tensile test specimen used.

Figure A1 - Cross structure with 10%, 25%, 50%, and 70% of volume fill

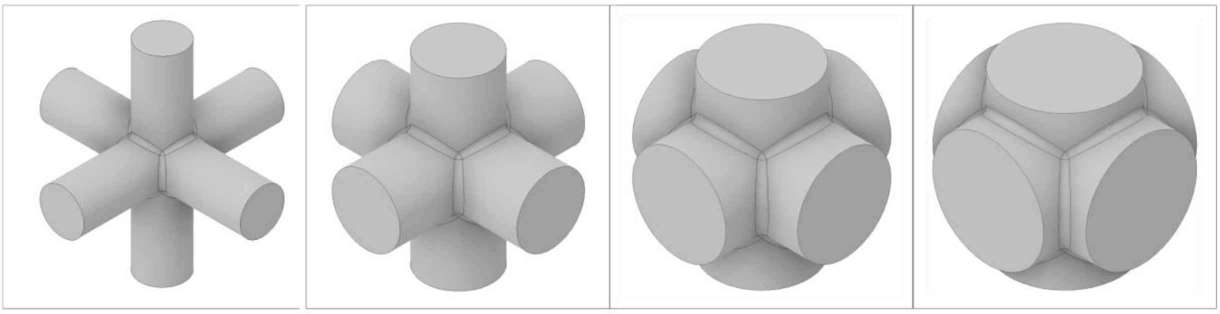

Source: author.

Figure A2 - BCC structure with 10%, 25%, 50%, and 70% of volume fill

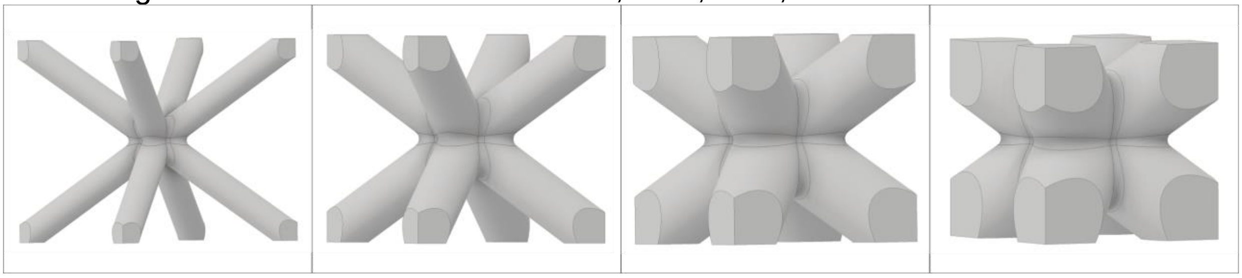

Source: author.

Figure A3 - Octet-truss structure with 10%, 25% and 50% of volume fill

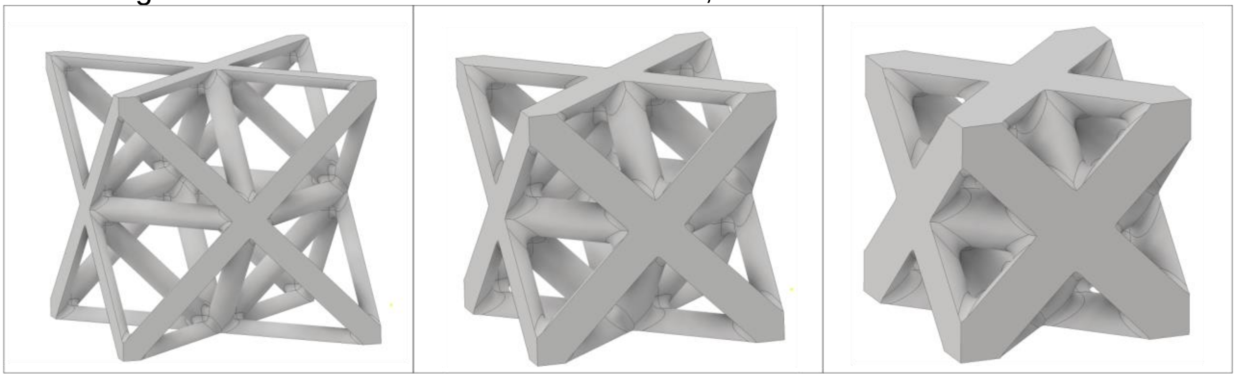

Source: author.

Figure A4 - Tensile test specimen used for lattice structures.

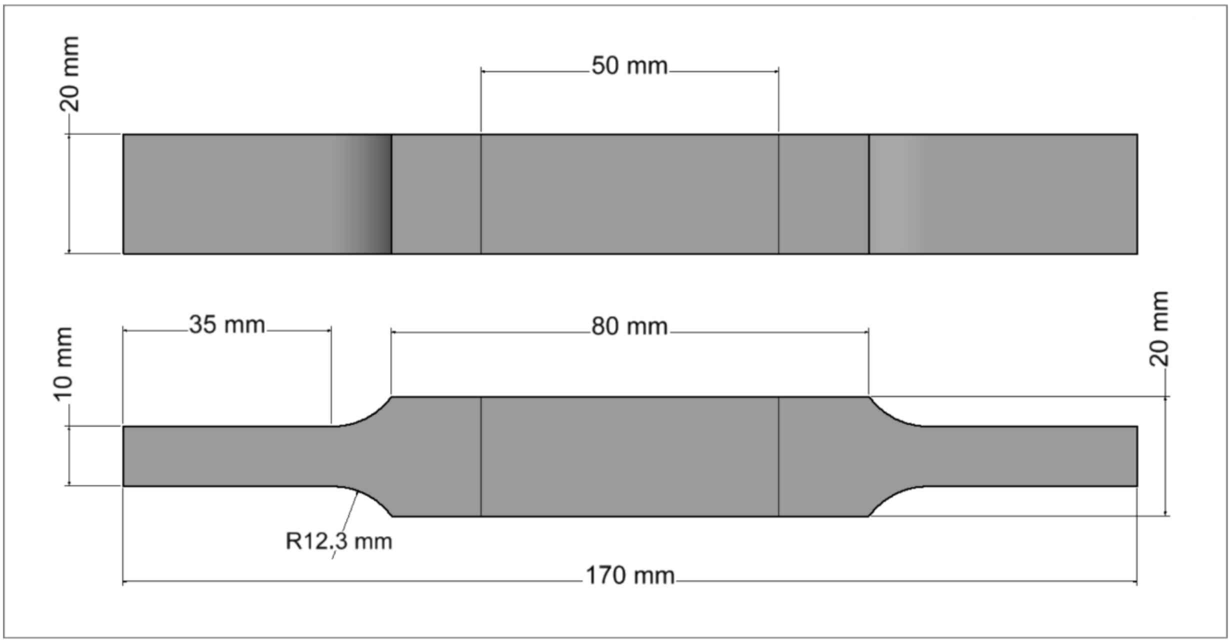

Source: author.

Appendix B - Engineering stress-strain curves for solid parts

Images of 28 engineering stress-strain curves for remaining 13 orientations of solid tensile specimens.

Figure B1 - Engineering stress-strain curves for A1V2 specimens.

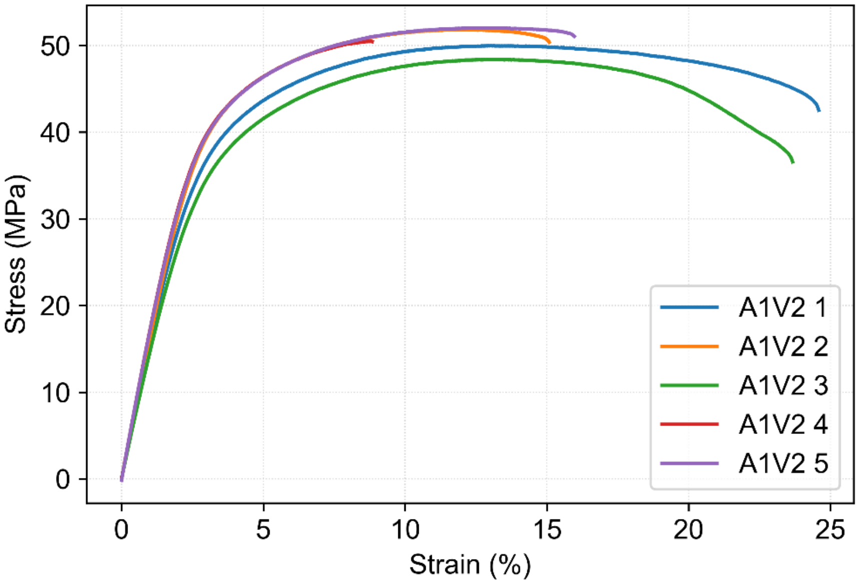

Source: author.

Figure B2 - Engineering stress-strain curves for A2V1 specimens.

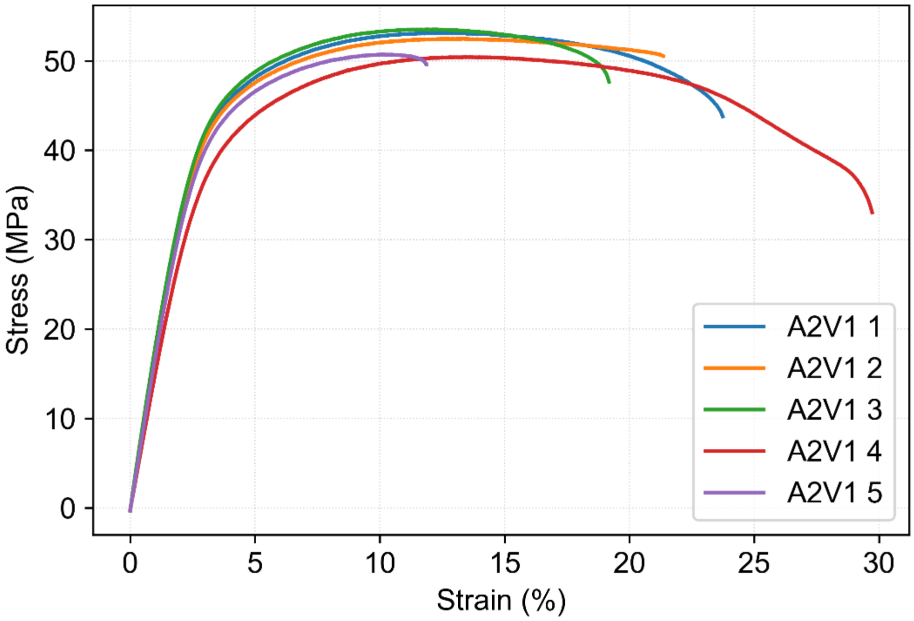

Source: author.

Figure B3 - Engineering stress-strain curves for A2V2 specimens.

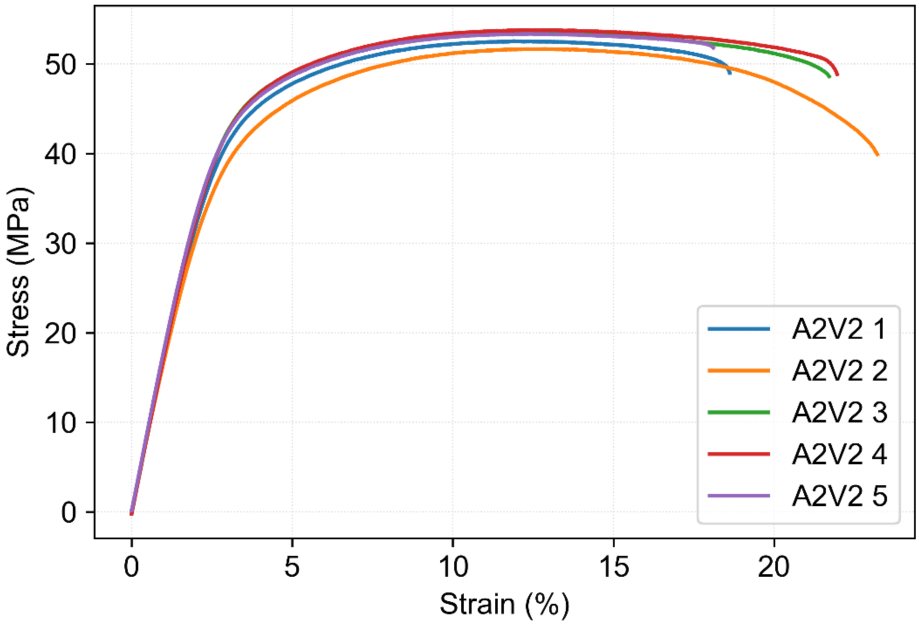

Source: author.

Figure B4 - Engineering stress-strain curves for A3V1 specimens.

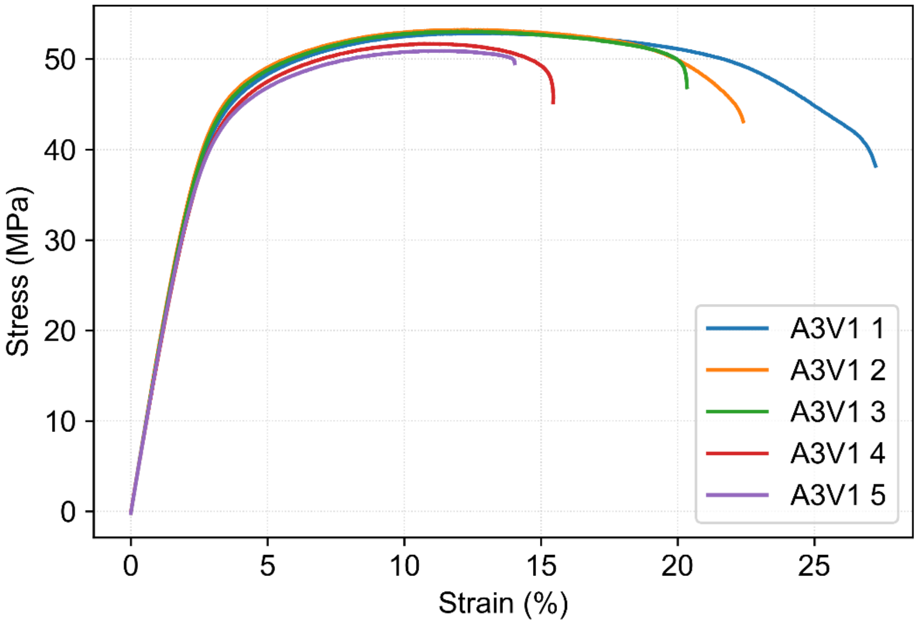

Source: author.

Figure B5 - Engineering stress-strain curves for A3V2 specimens.

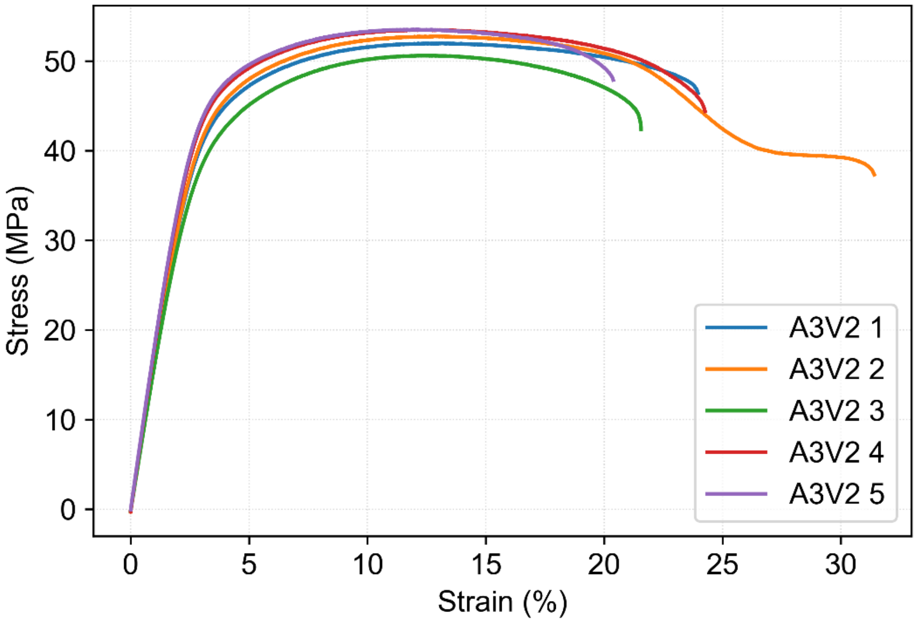

Source: author.

Figure B6 - Engineering stress-strain curves for B1V1 specimens.

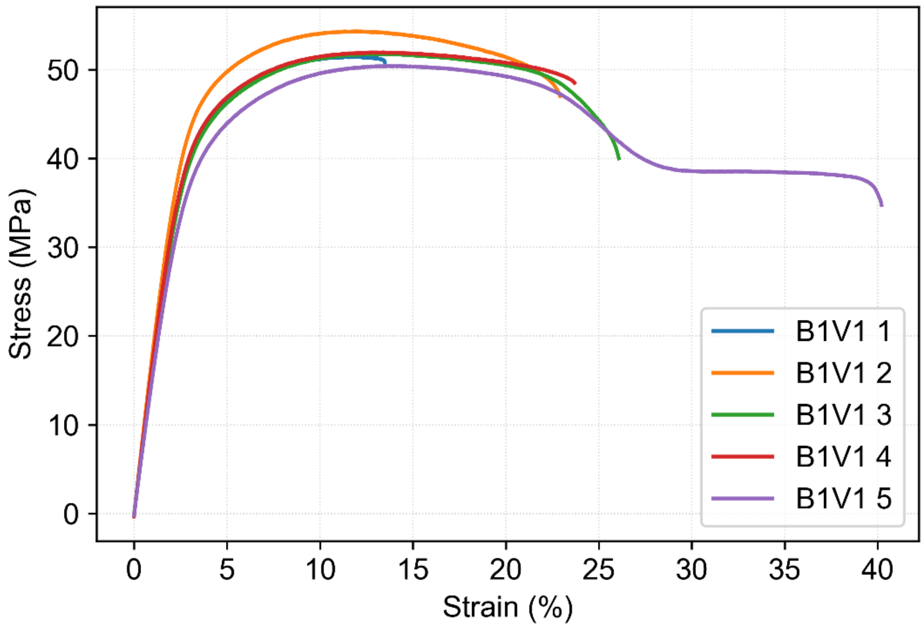

Source: author.

Figure B7 - Engineering stress-strain curves for B1V2 specimens.

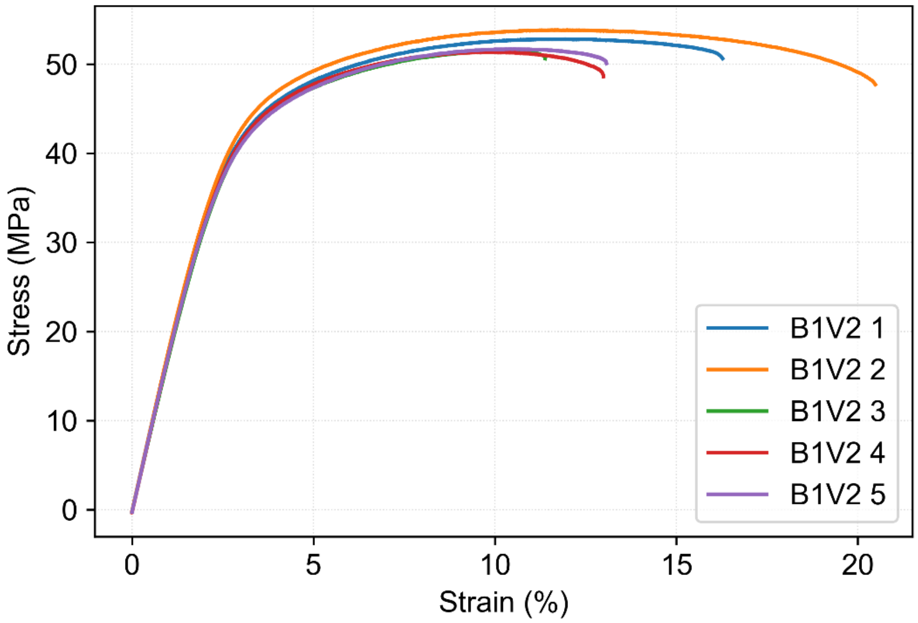

Source: author.

Figure B8 - Engineering stress-strain curves for B2V1 specimens.

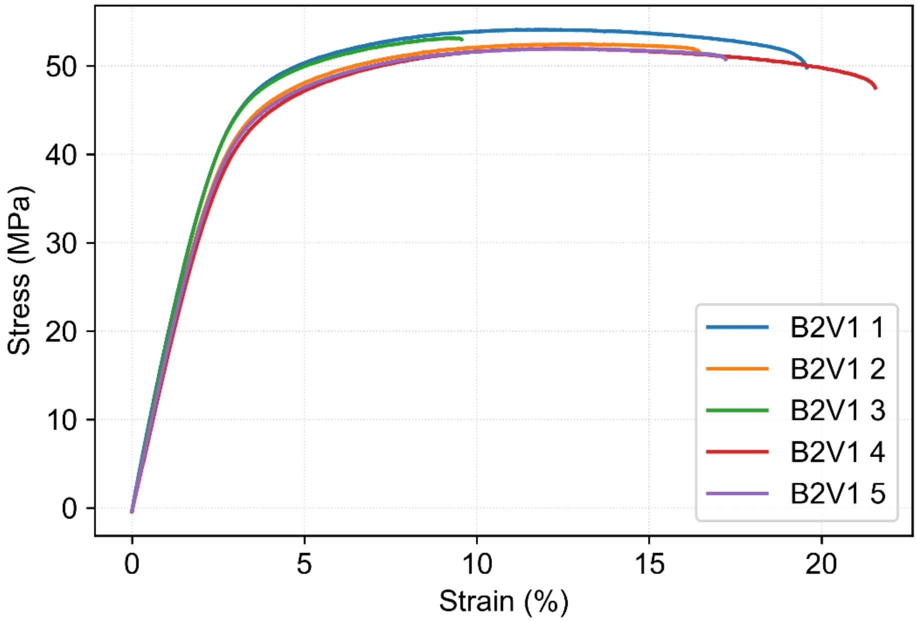

Source: author.

Figure B9 - Engineering stress-strain curves for B2V2 specimens.

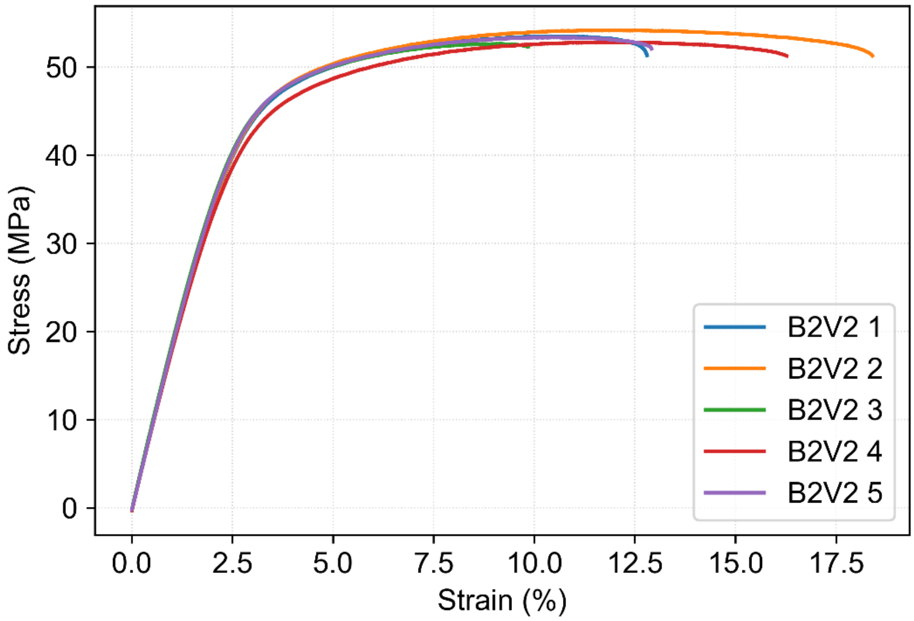

Source: author.

Figure B10 - Engineering stress-strain curves for B3V1 specimens.

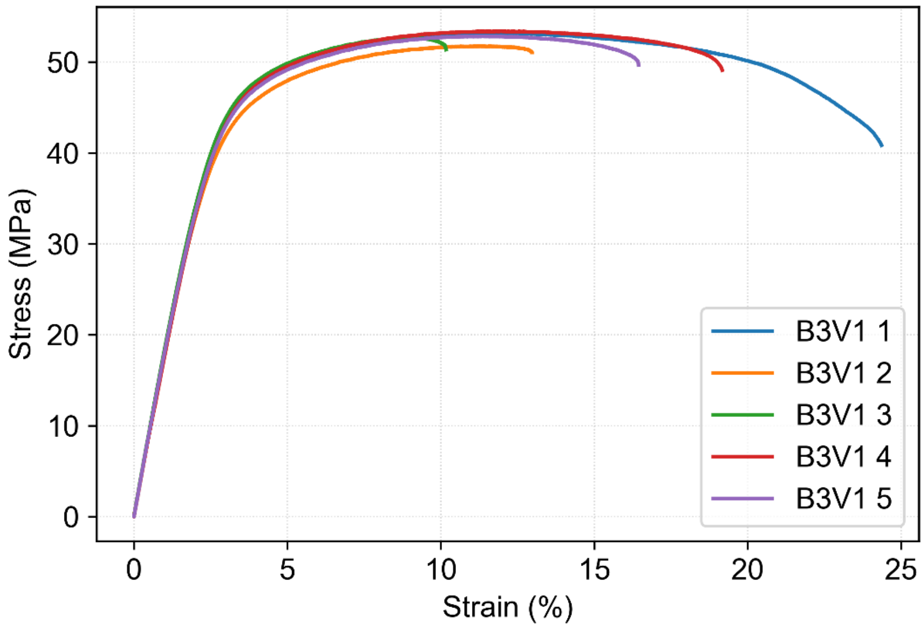

Source: author.

Figure B11 - Engineering stress-strain curves for B3V2 specimens.

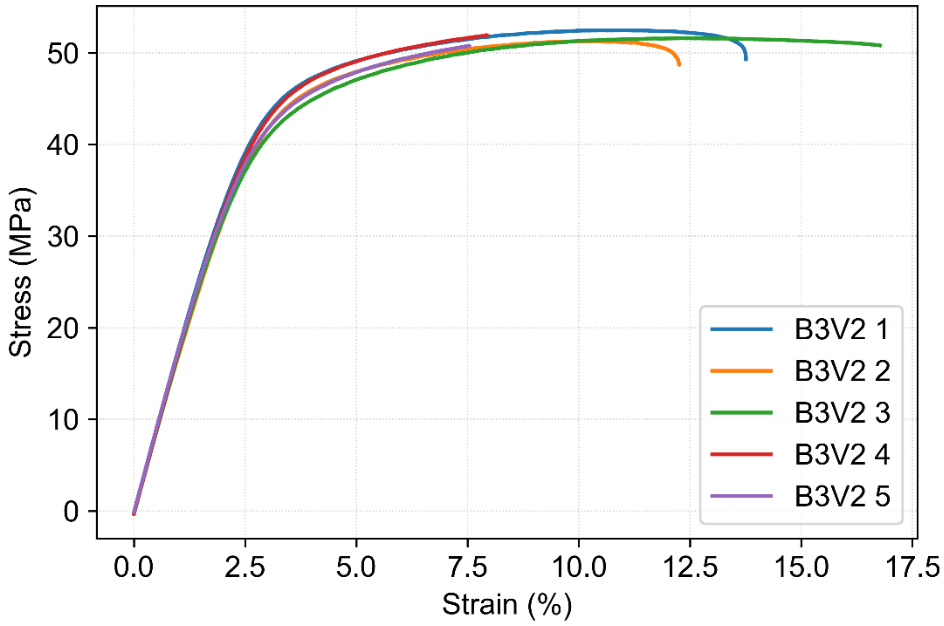

Source: author.

Figure B12 - Engineering stress-strain curves for C1V1 specimens.

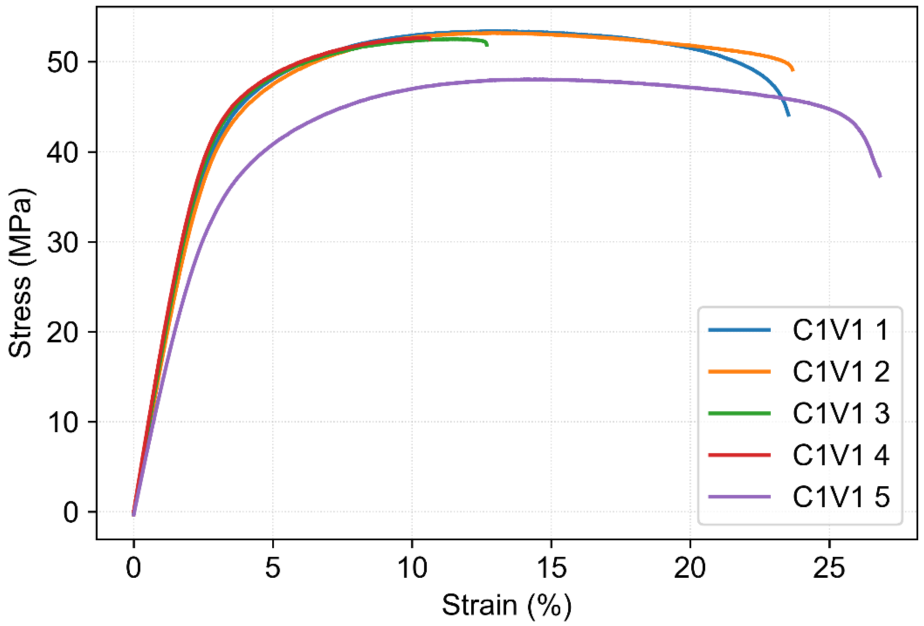

Source: author.

Figure B13 - Engineering stress-strain curves for C1V2 specimens.

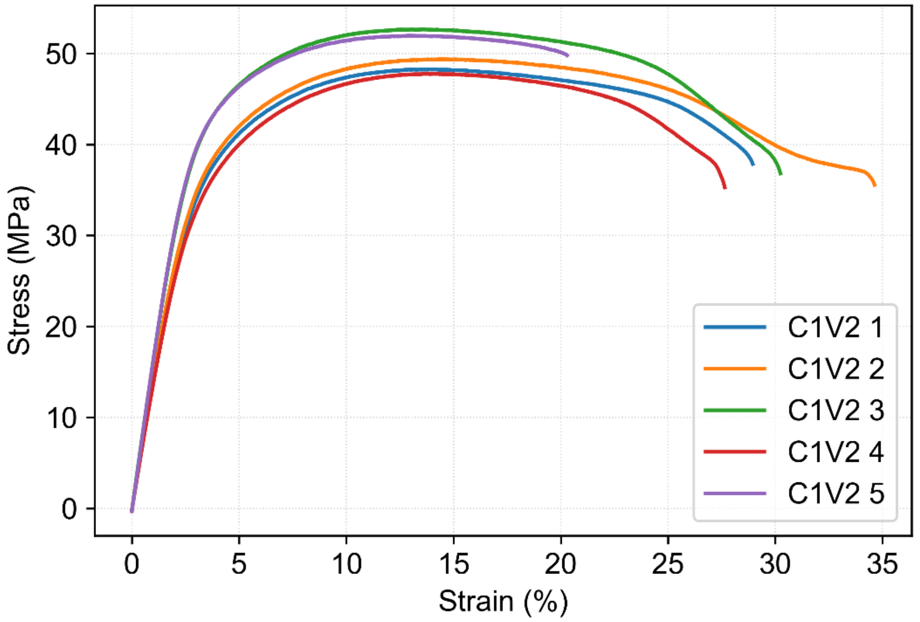

Source: author.

Figure B14 - Engineering stress-strain curves for C2V1 specimens.

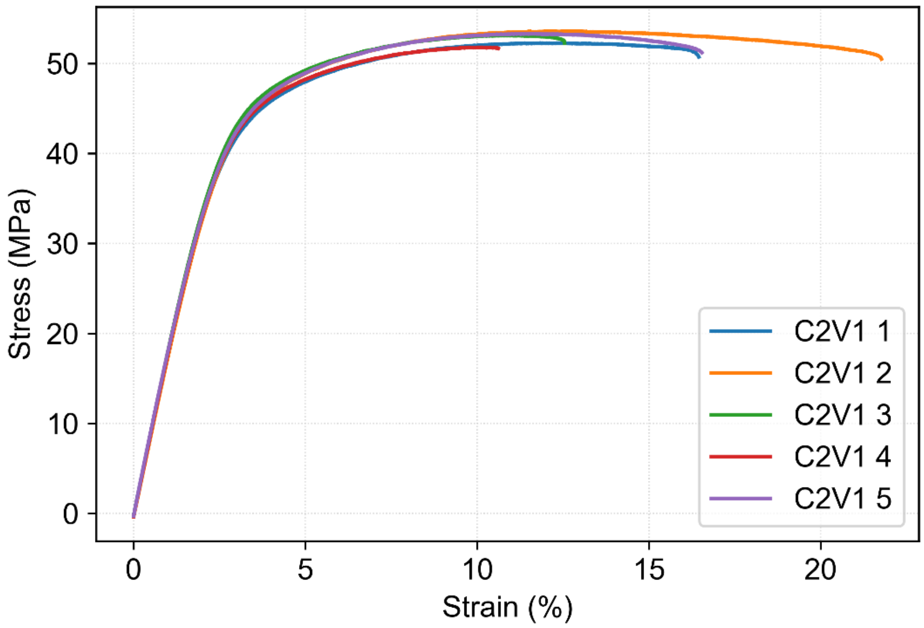

Source: author.

Figure B15 - Engineering stress-strain curves for C2V2 specimens.

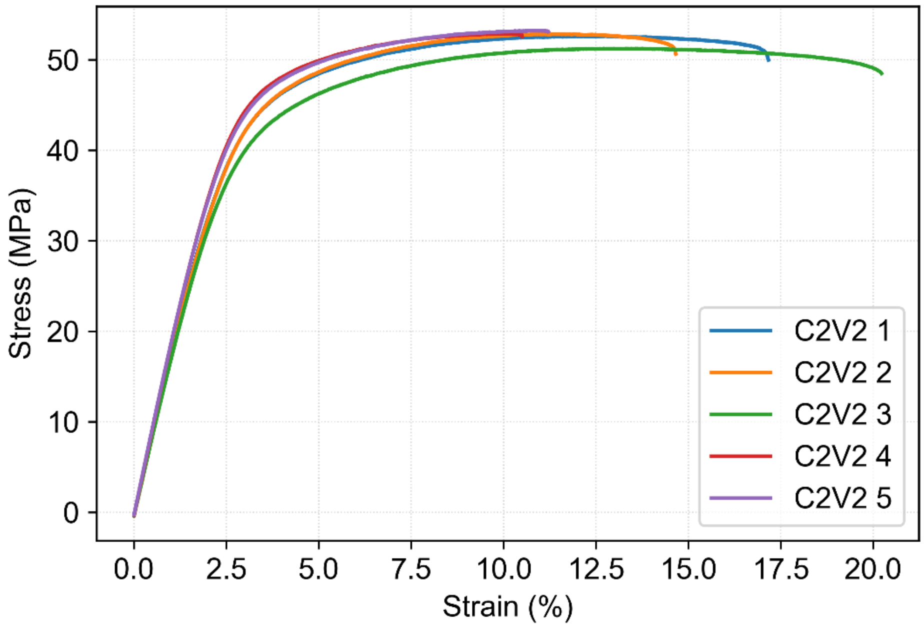

Source: author.

Figure B16 - Engineering stress-strain curves for C3V1 specimens.

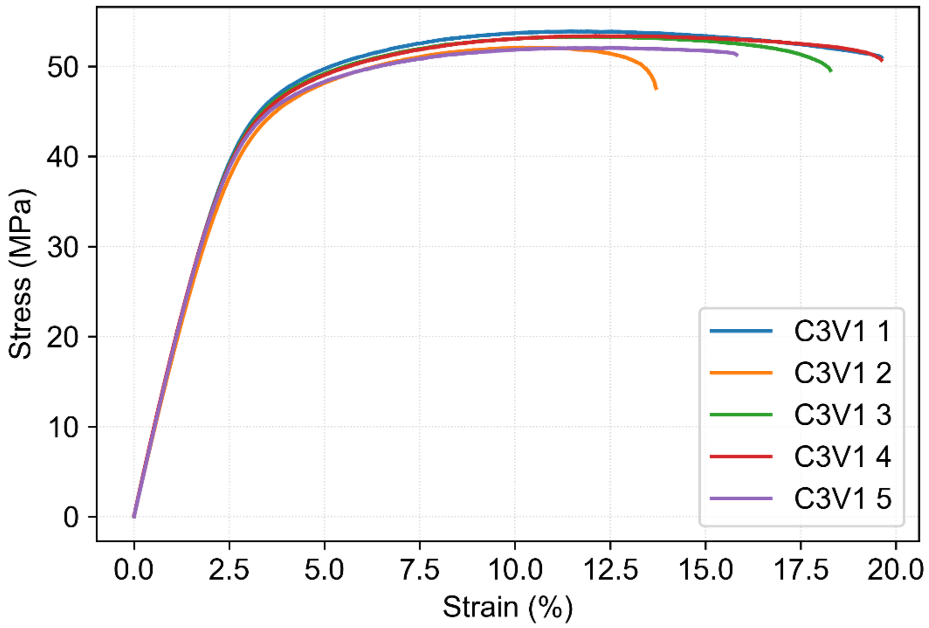

Source: author.

Figure B17 - Engineering stress-strain curves for C3V2 specimens.

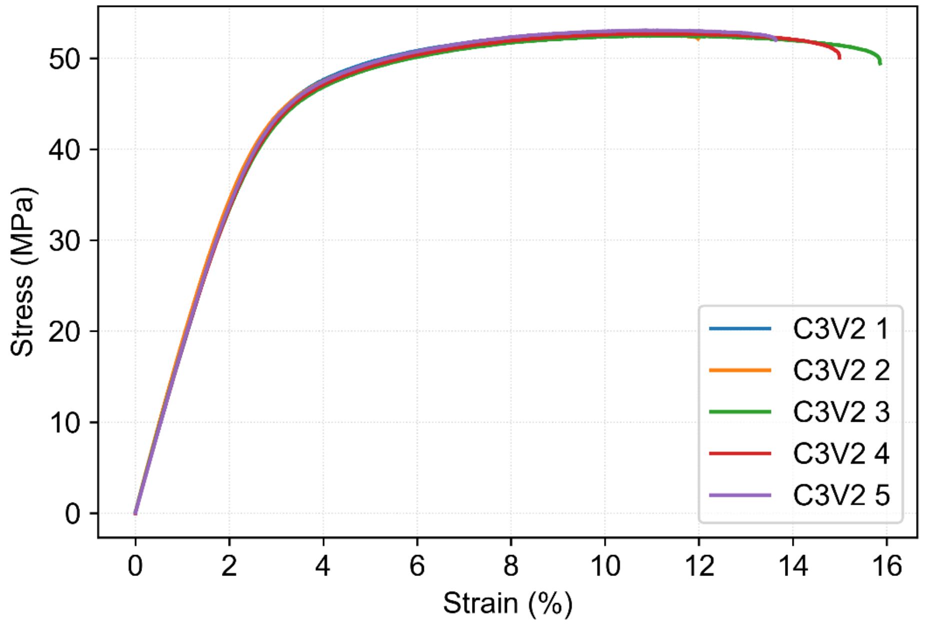

Source: author.

Figure B18 - Engineering stress-strain curves for D1V1 specimens.

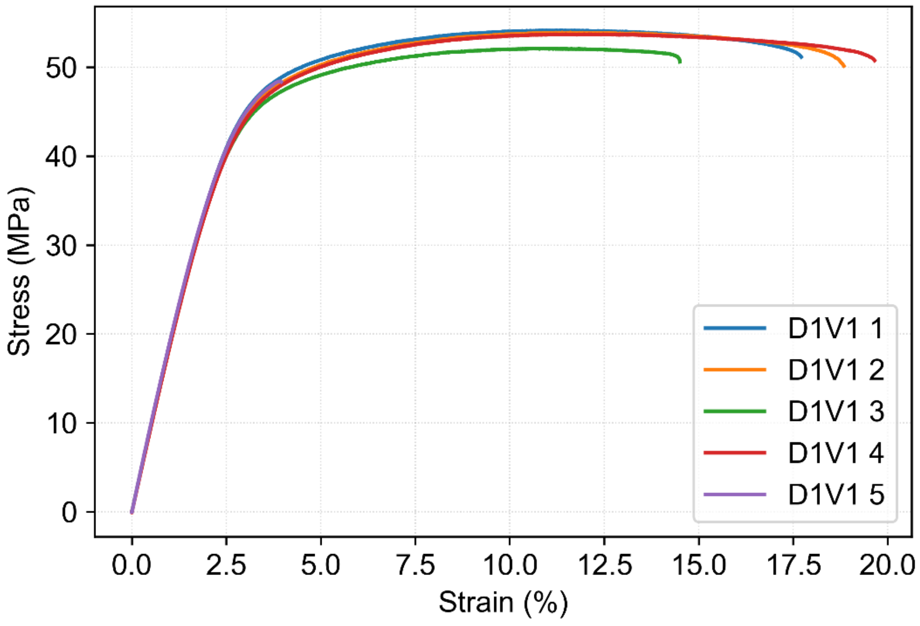

Source: author.

Figure B19 - Engineering stress-strain curves for D1V2 specimens.

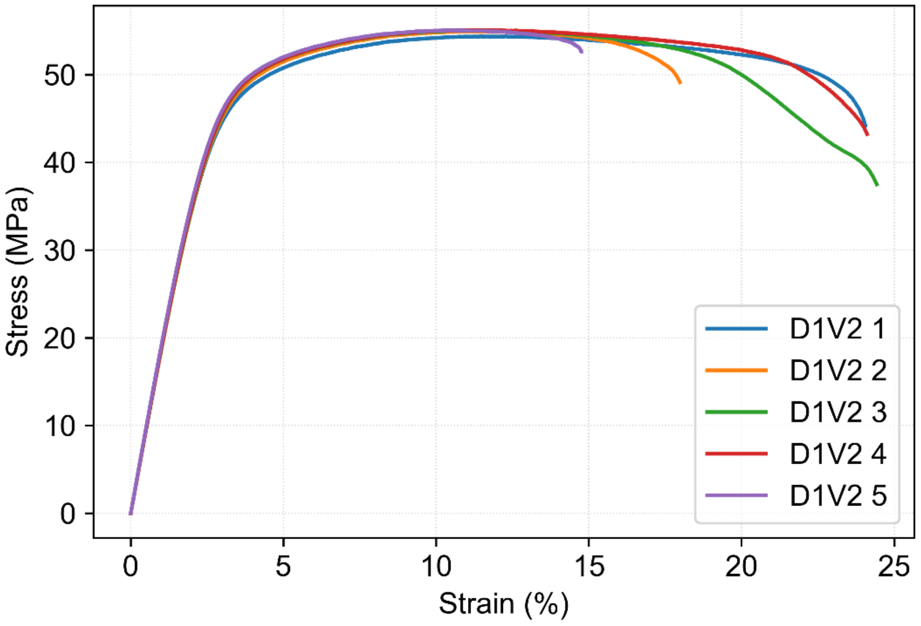

Source: author.

Figure B20 - Engineering stress-strain curves for D2V1 specimens.

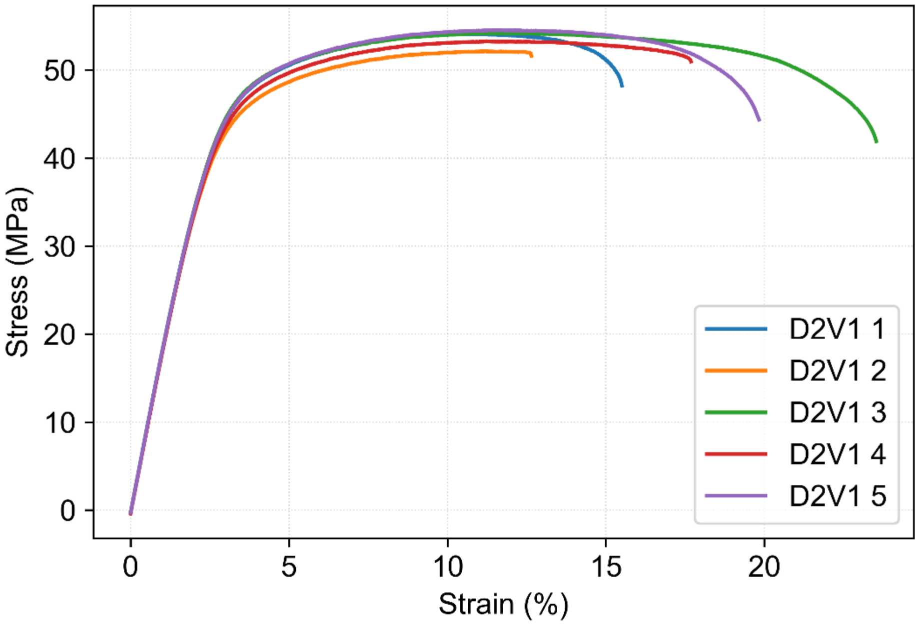

Source: author.

Figure B21 - Engineering stress-strain curves for D2V2 specimens.

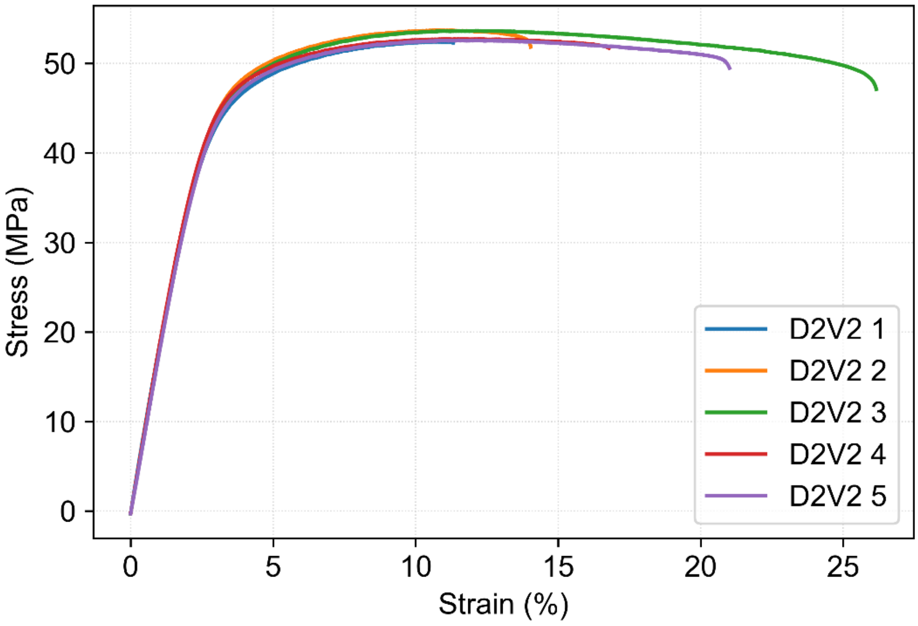

Source: author.

Figure B22 - Engineering stress-strain curves for D3V1 specimens.

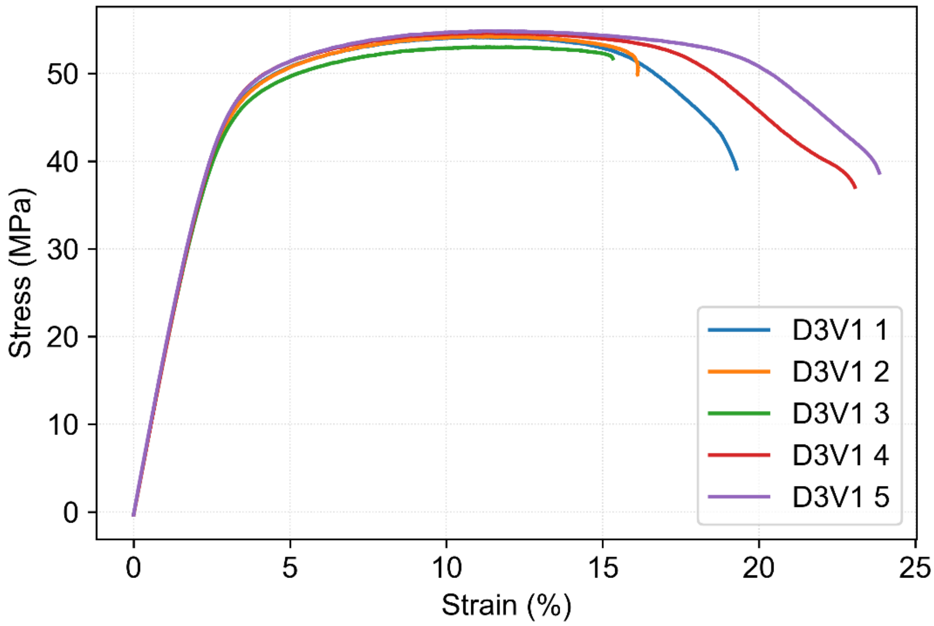

Source: author.

Figure B23 - Engineering stress-strain curves for E1V1 specimens.

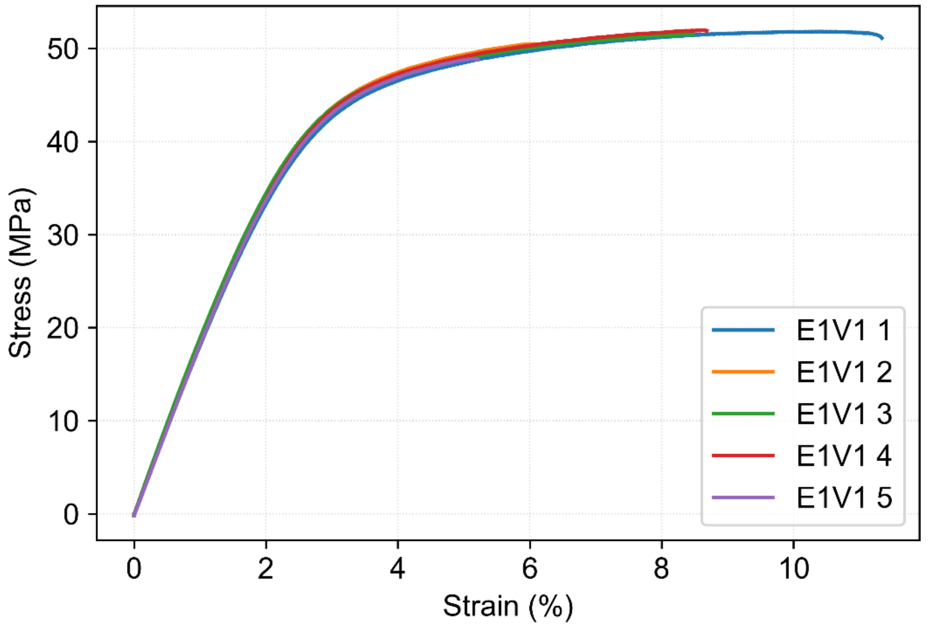

Source: author.

Figure B24 - Engineering stress-strain curves for E1V2 specimens.

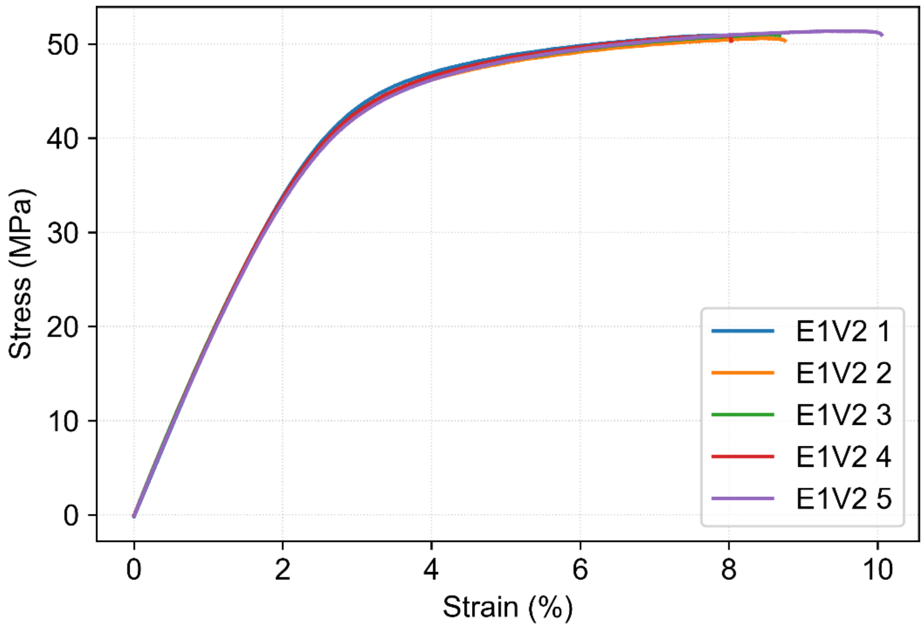

Source: author.

Figure B25 - Engineering stress-strain curves for E2V1 specimens.

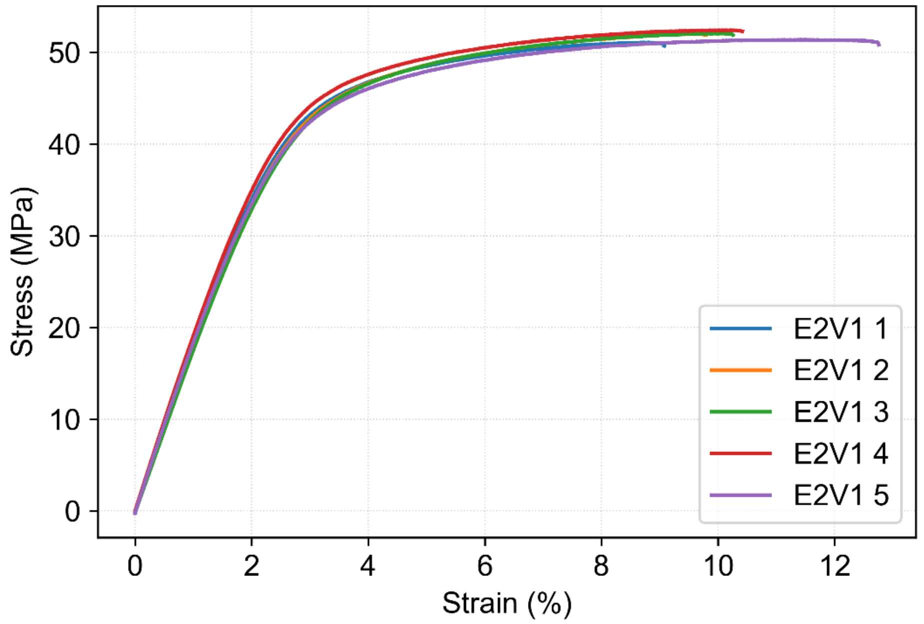

Source: author.

Figure B26 - Engineering stress-strain curves for E2V2 specimens.

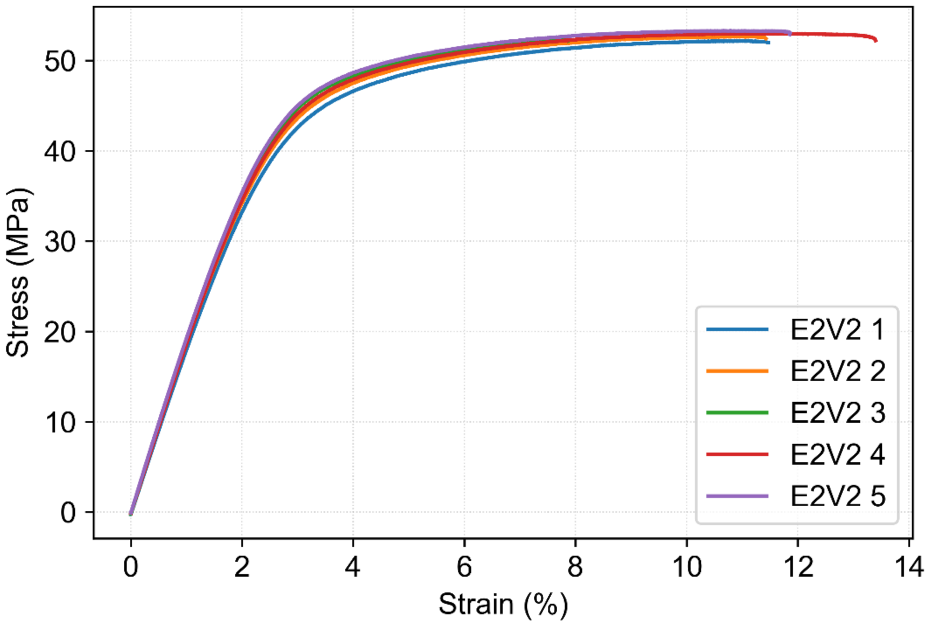

Source: author.

Figure B27 - Engineering stress-strain curves for E3V1 specimens.

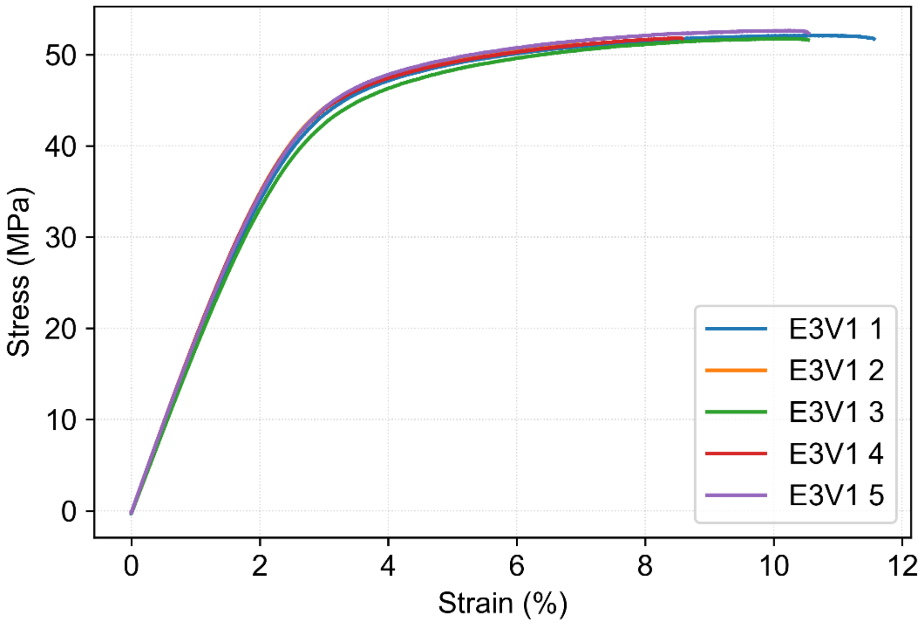

Source: author.

Figure B28 - Engineering stress-strain curves for E3V2 specimens.

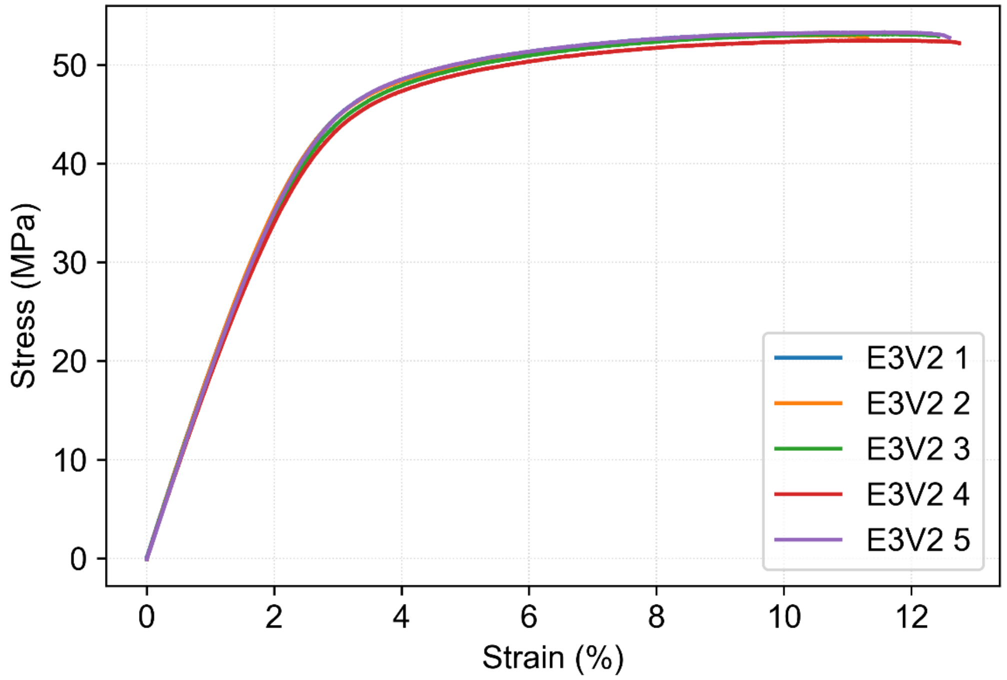

Source: author.

Appendix C - Force-displacement curves for lattice structure parts

Images of force-displacement curves for lattice structure tensile specimens, with four different percentage of volume occupied by material, and tested in four possible orientations.

Figure C1 - Force-displacement curves for Cross 10% A0° specimens.

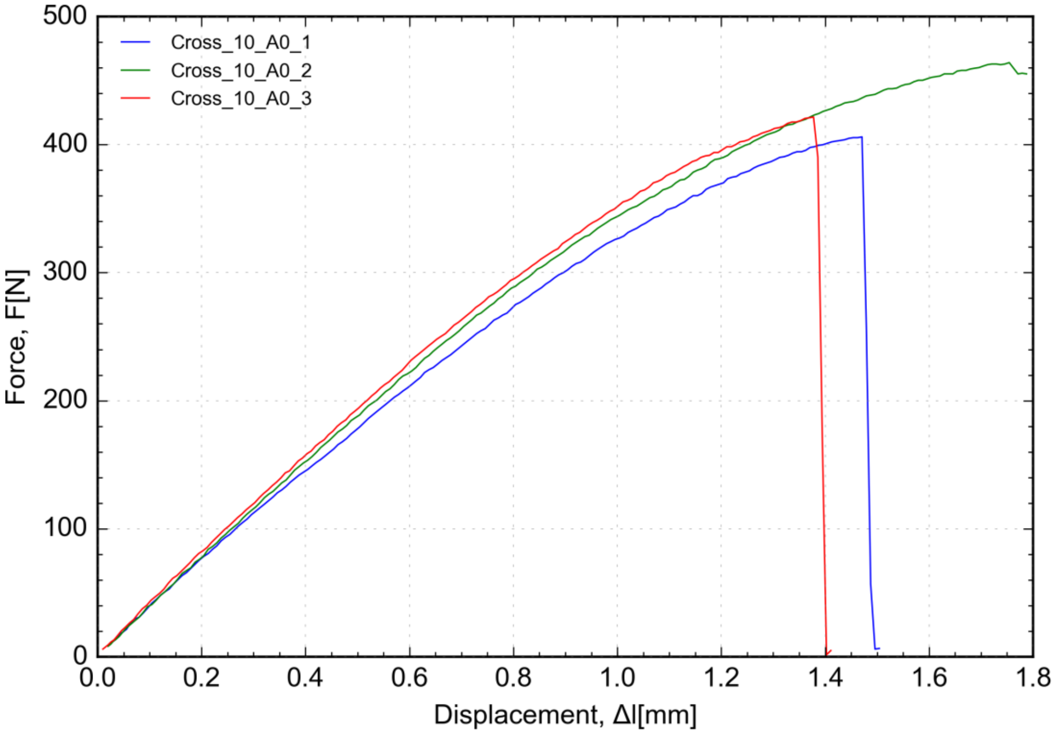

Source: Laboratory of prototype technologies and processes, 2019.

Figure C2 - Force-displacement curve for Cross 10% B45° specimen.

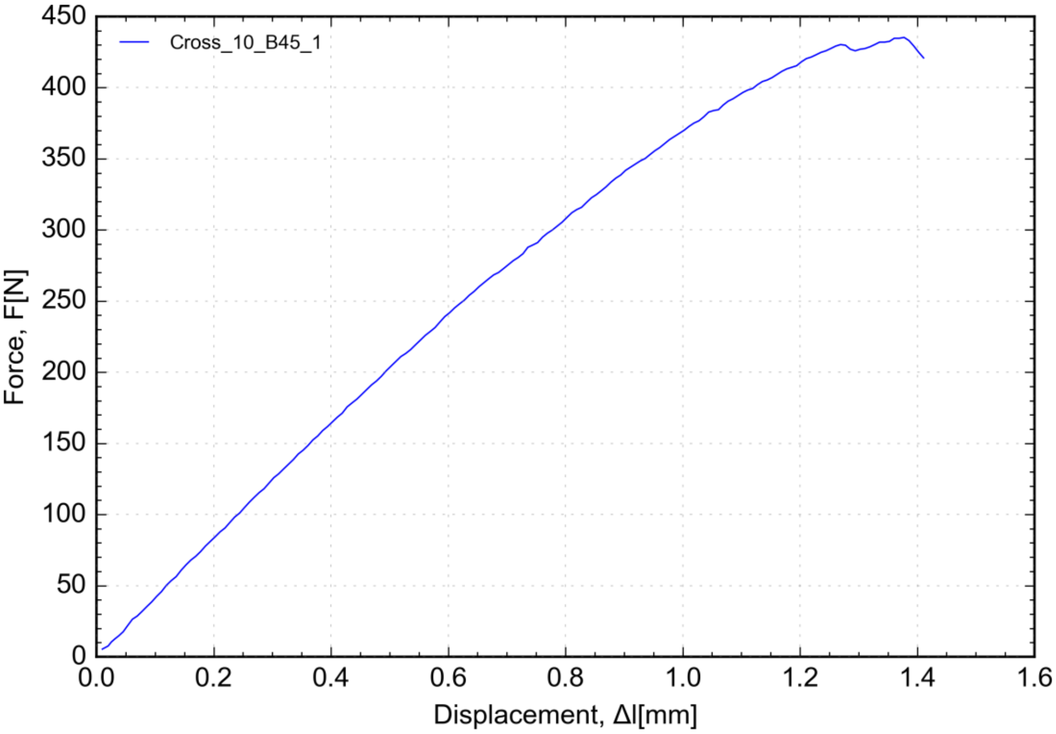

Source: Laboratory of prototype technologies and processes, 2019.

Figure C3 - Force-displacement curves for Cross 10% B90° specimens.

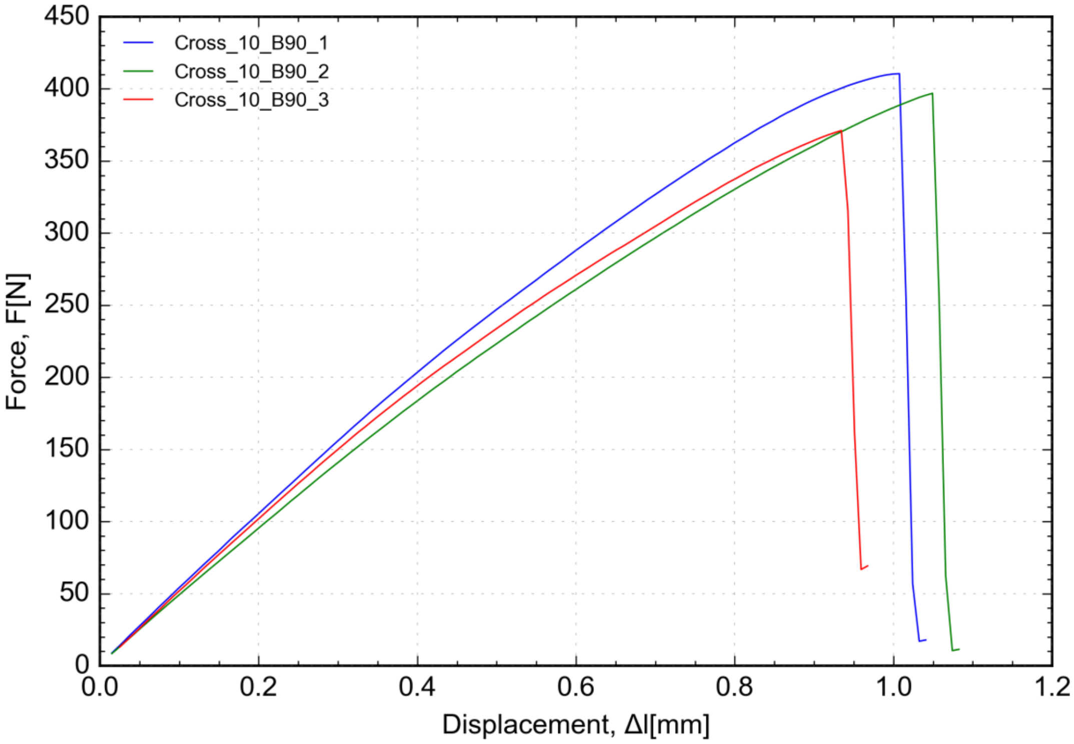

Source: Laboratory of prototype technologies and processes, 2019.

Figure C4 - Force-displacement curves for Cross 25% A0° specimens.

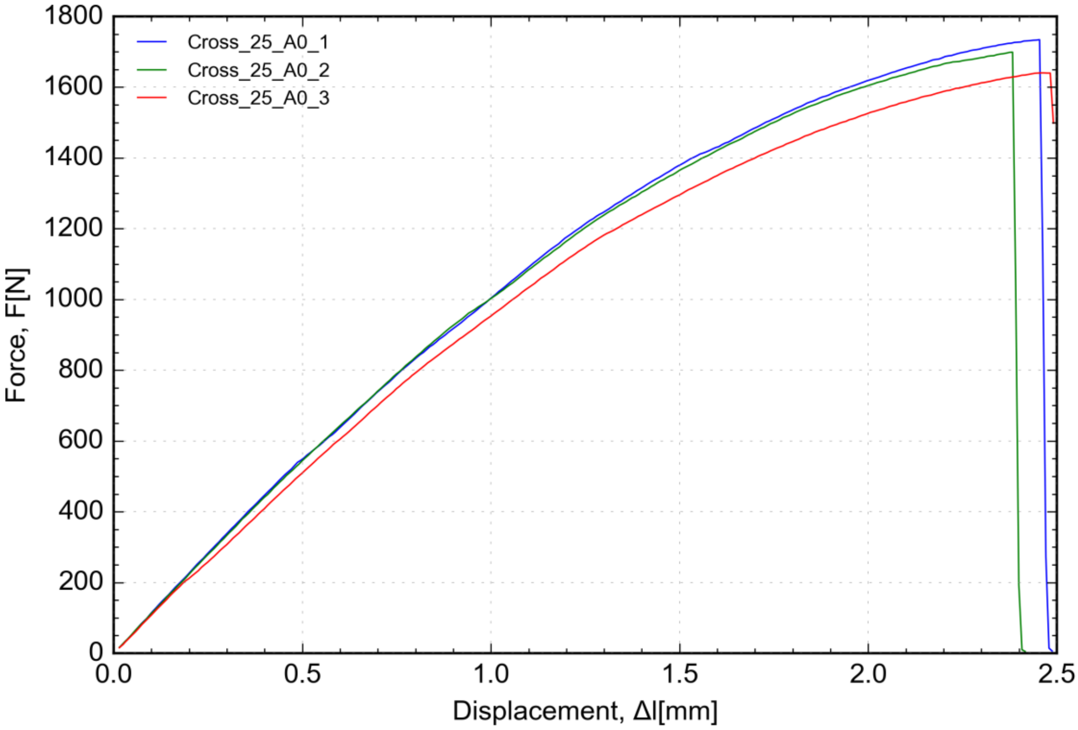

Source: Laboratory of prototype technologies and processes, 2019.

Figure C5- Force-displacement curve for Cross 25% B45° specimen.

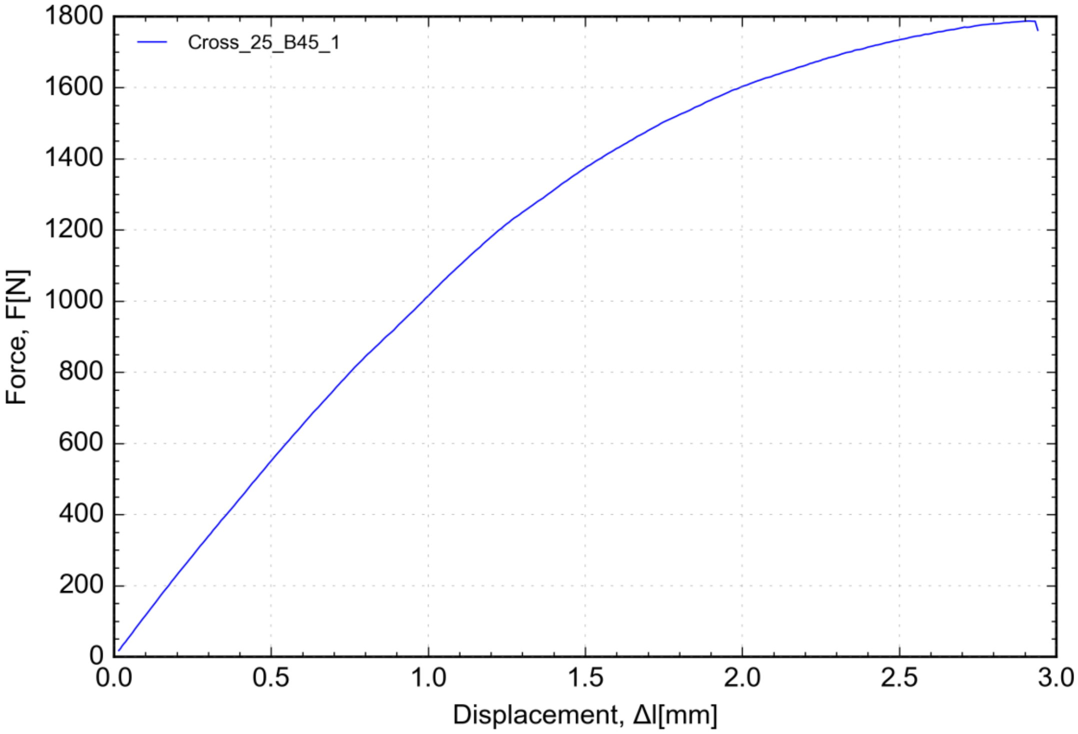

Source: Laboratory of prototype technologies and processes, 2019.

Figure C6 - Force-displacement curves for Cross 25% B90° specimens.

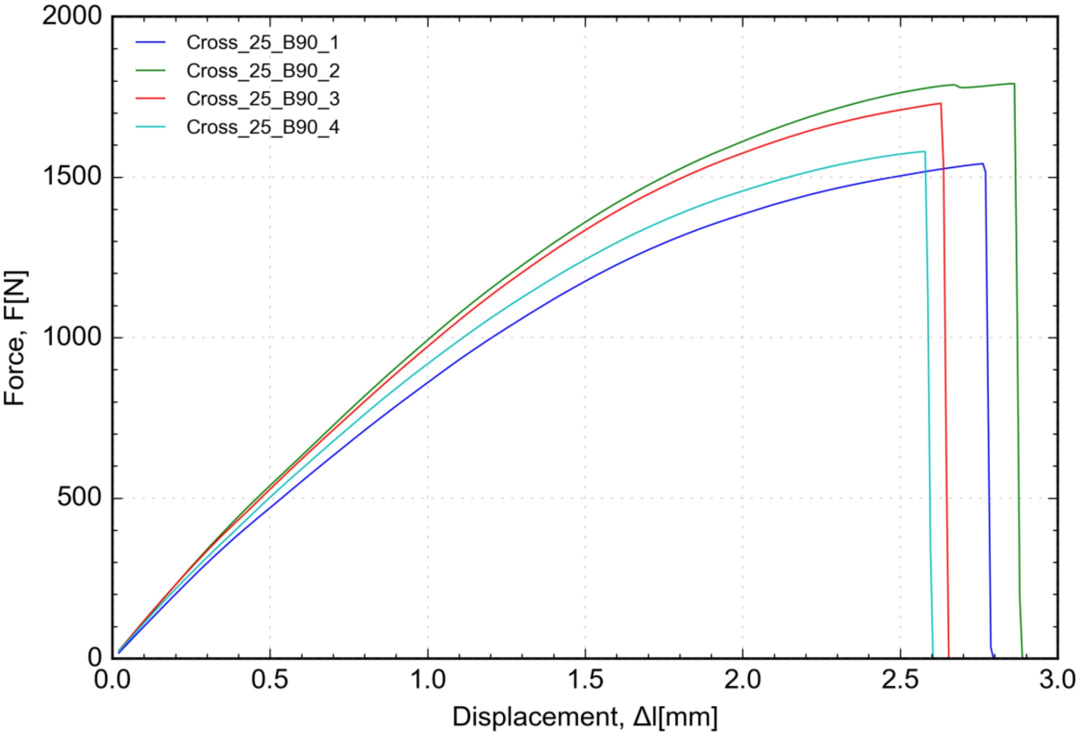

Source: Laboratory of prototype technologies and processes, 2019.

Figure C7 - Force-displacement curves for Cross 50% A0° specimens.

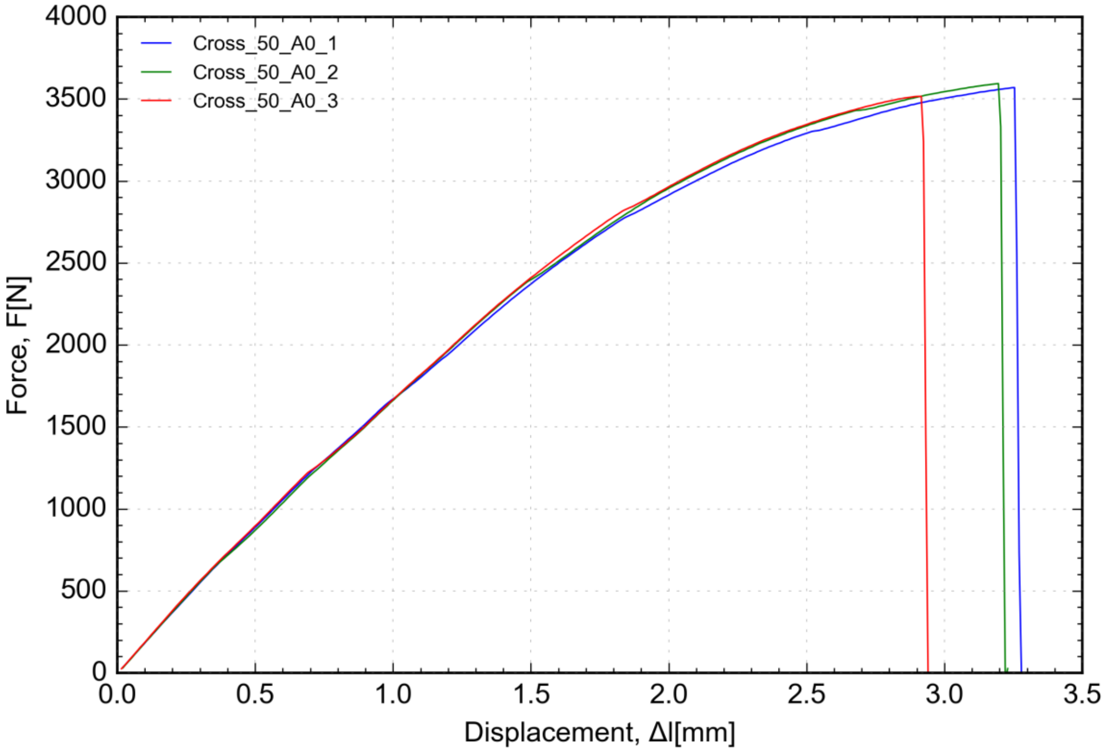

Source: Laboratory of prototype technologies and processes, 2019.

Figure C8 - Force-displacement curve for Cross 50% B45° specimens.

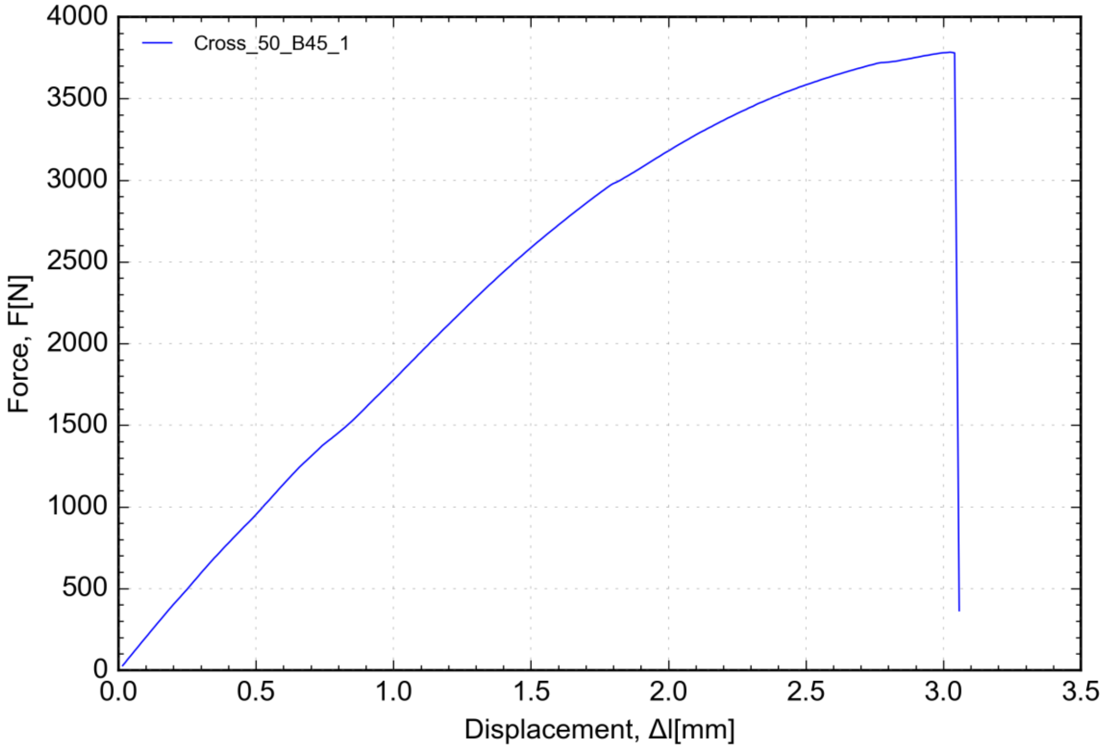

Source: Laboratory of prototype technologies and processes, 2019.

Figure C9 - Force-displacement curves for Cross 50% B90° specimens.

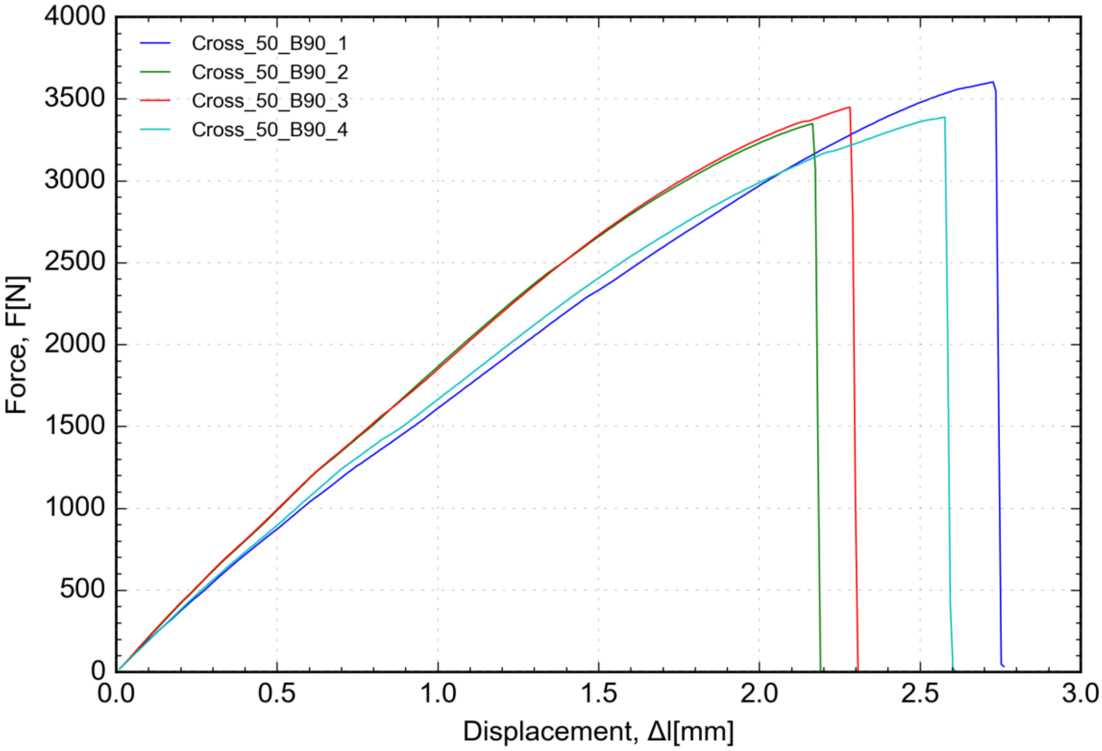

Source: Laboratory of prototype technologies and processes, 2019.

Figure C10 - Force-displacement curves for Cross 70% A0° specimens.

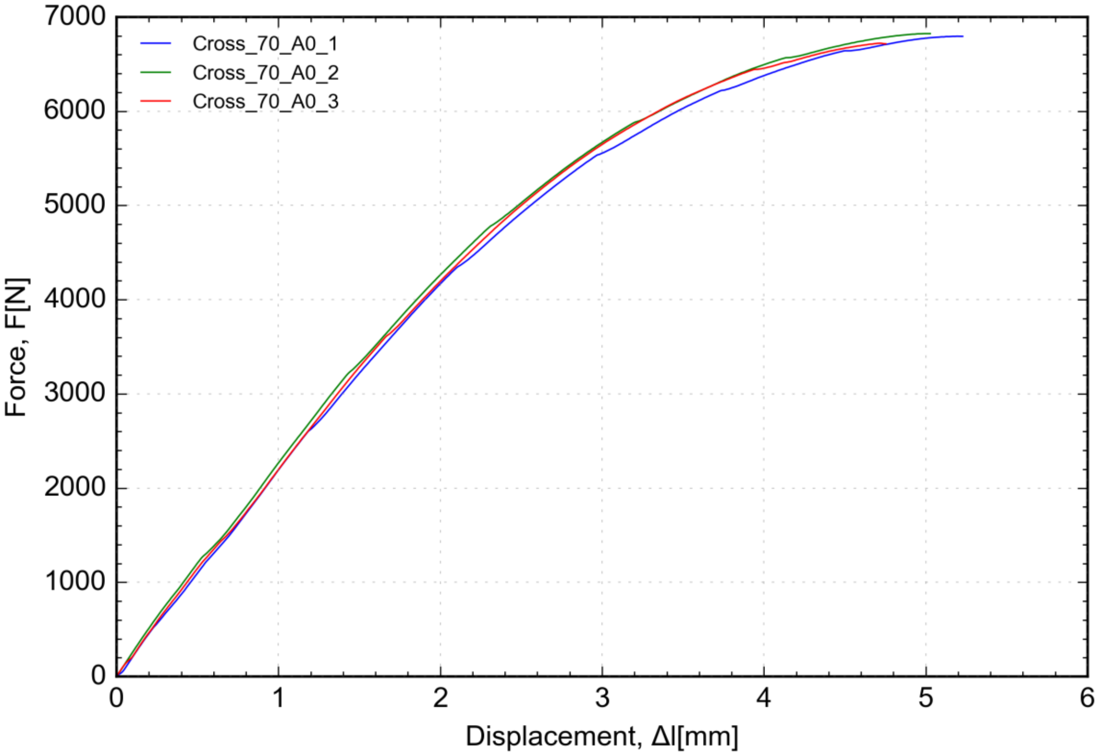

Source: Laboratory of prototype technologies and processes, 2019.

Figure C11 - Force-displacement curve for Cross 70% B45° specimen.

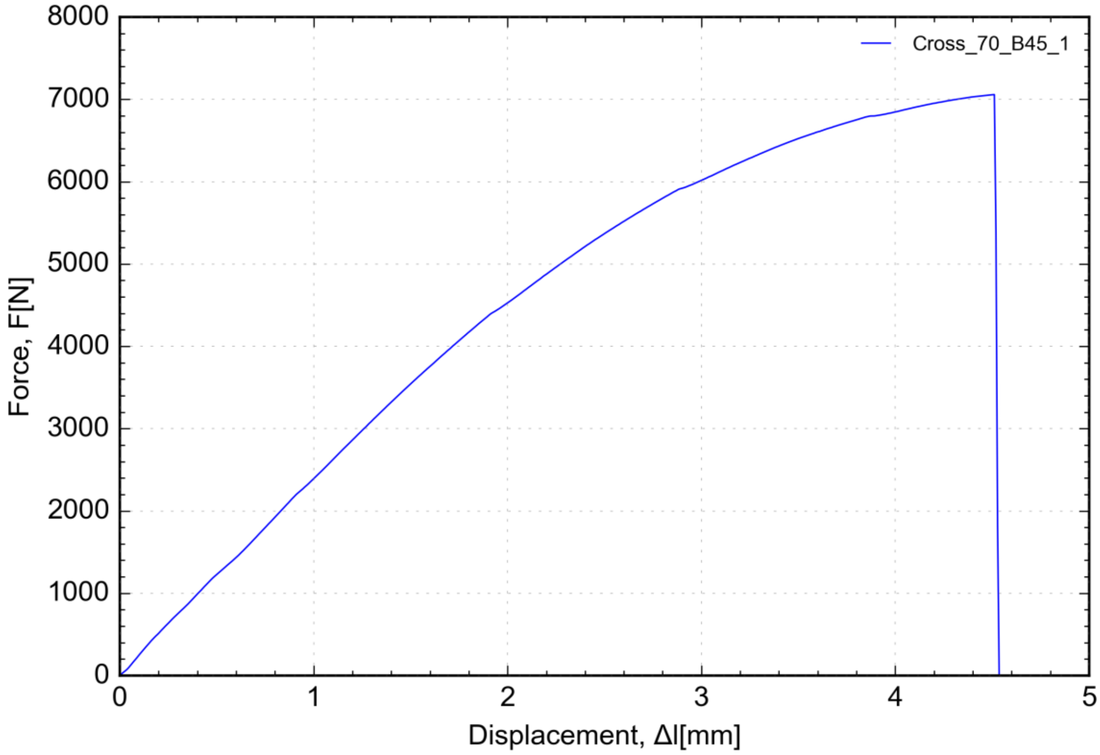

Source: Laboratory of prototype technologies and processes, 2019.

Figure C12 - Force-displacement curves for Cross 70% B90° specimens.

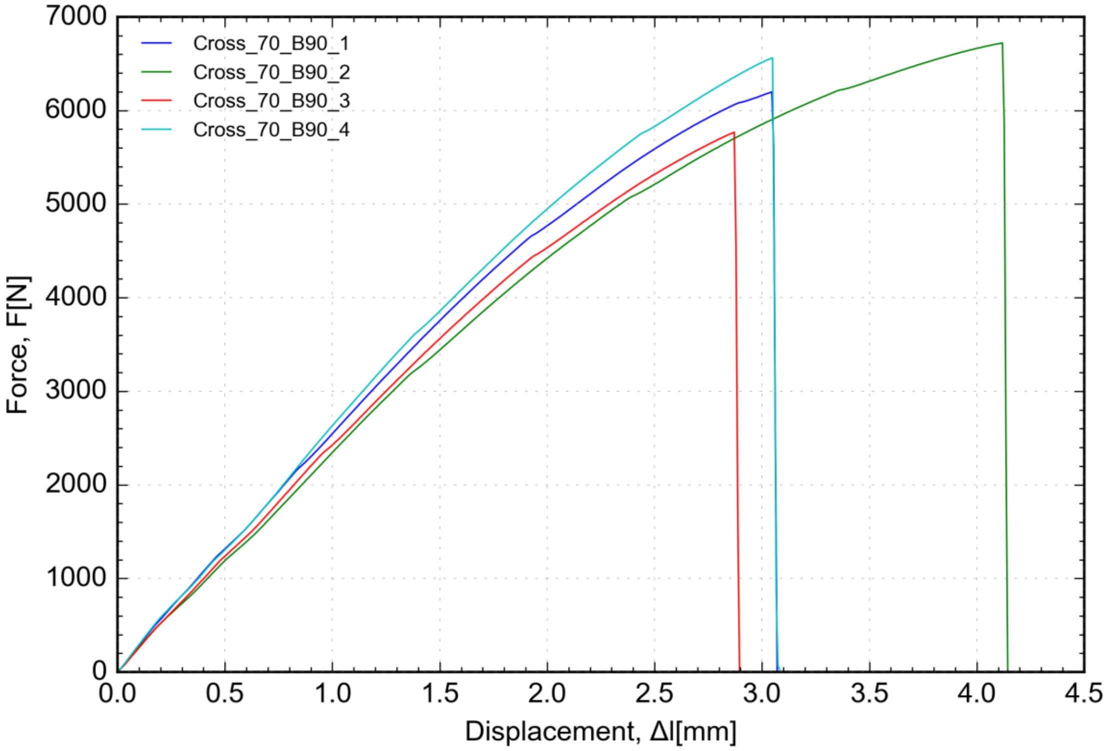

Source: Laboratory of prototype technologies and processes, 2019.

Figure C13 - Force-displacement curves for BCC 10% A0° specimens.

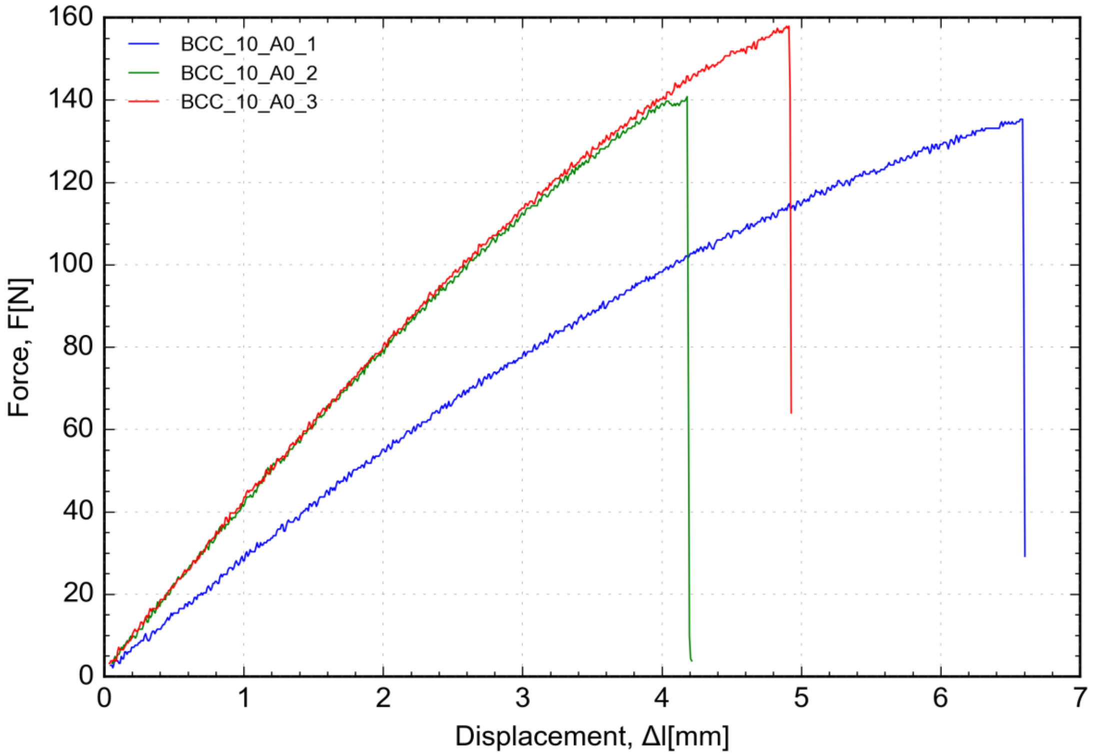

Source: Laboratory of prototype technologies and processes, 2019.

Figure C14 - Force-displacement curves for BCC 10% A45°C-90° specimens.

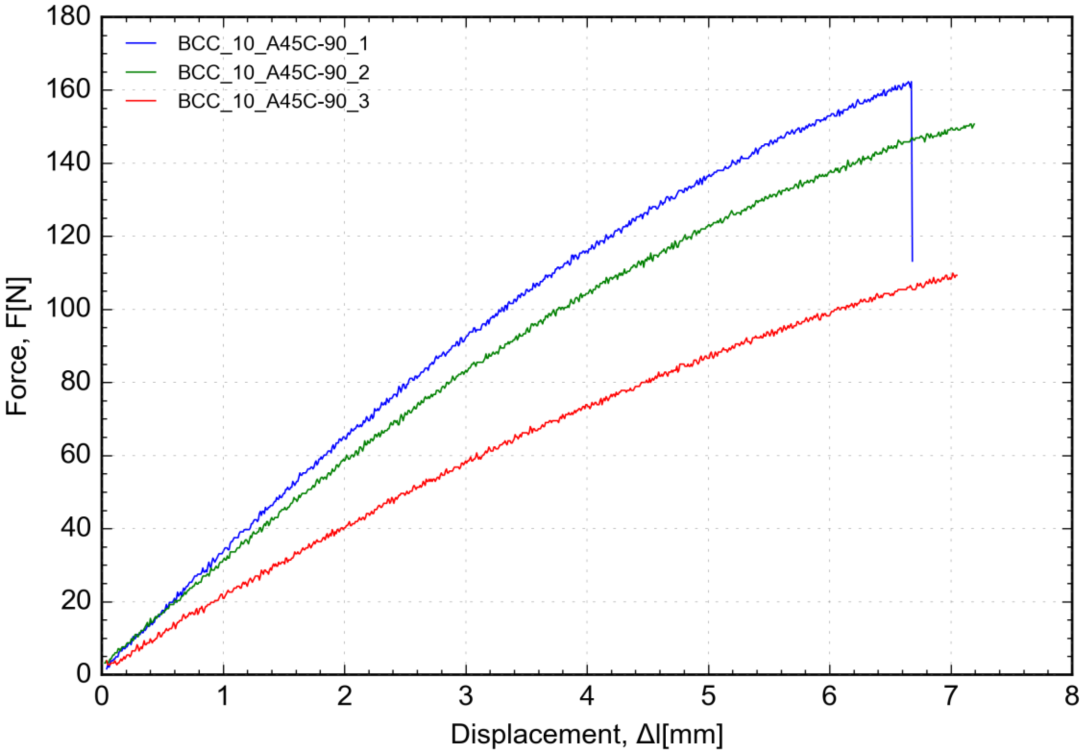

Source: Laboratory of prototype technologies and processes, 2019.

Figure C15 - Force-displacement curves for BCC 10% B90° specimens.

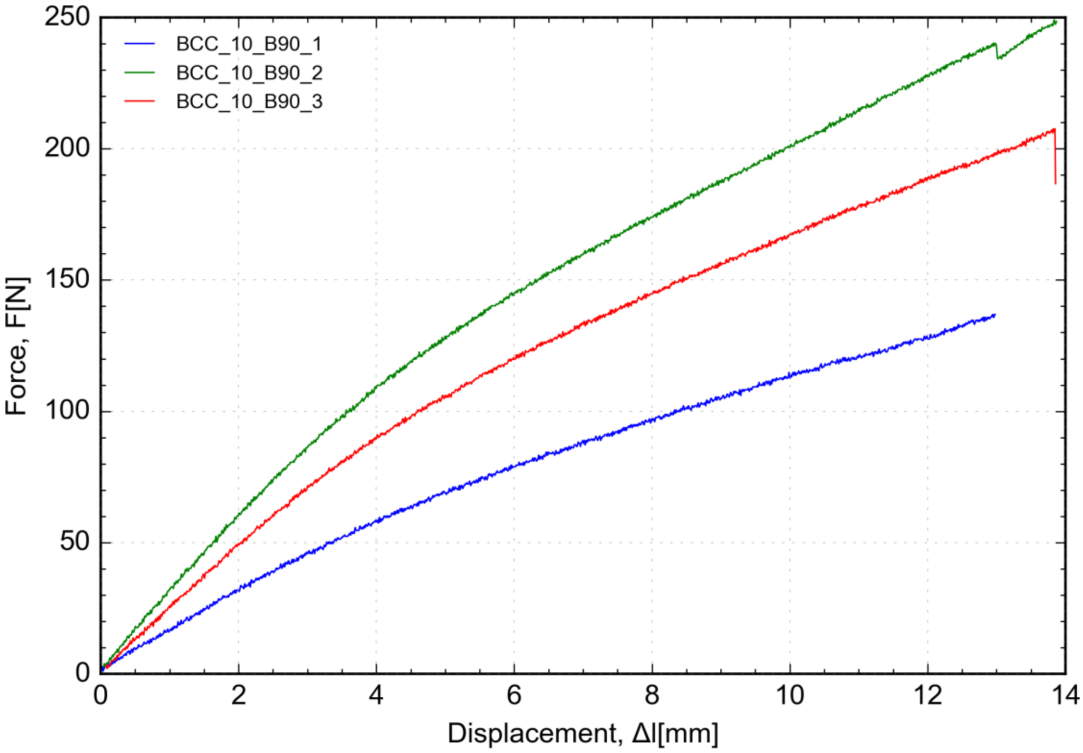

Source: Laboratory of prototype technologies and processes, 2019.

Figure C16 - Force-displacement curves for BCC 25% A0° specimens.

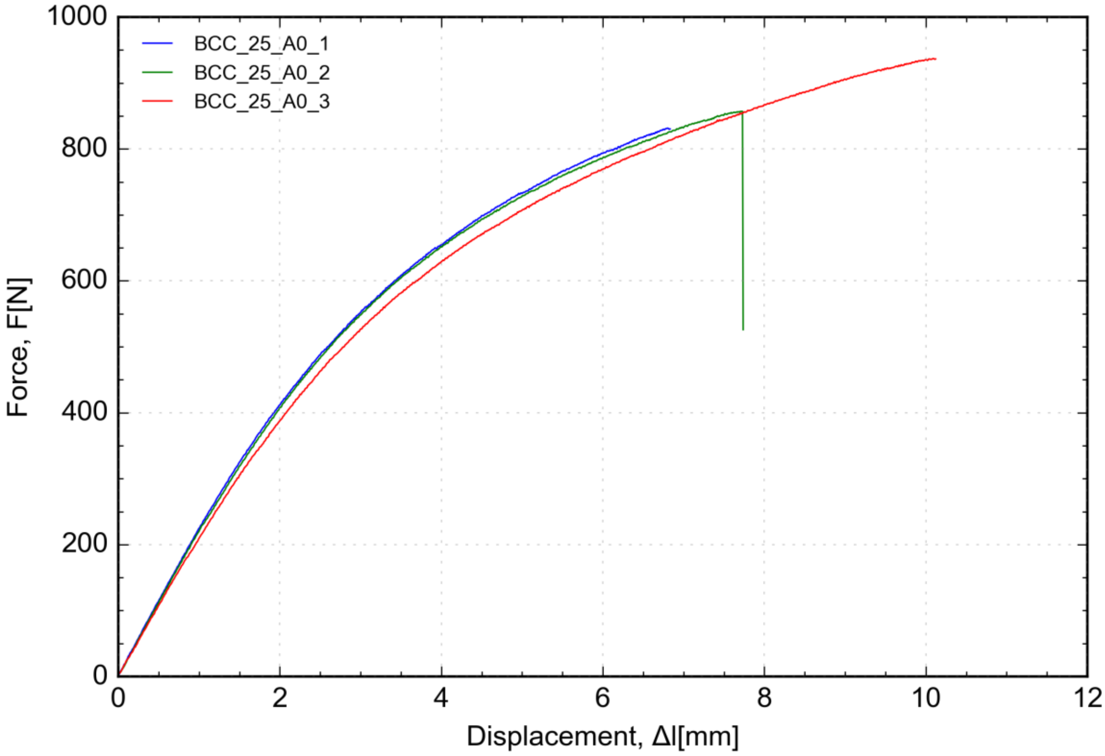

Source: Laboratory of prototype technologies and processes, 2019.

Figure C17 - Force-displacement curves for BCC 25% A45°C-90° specimens.

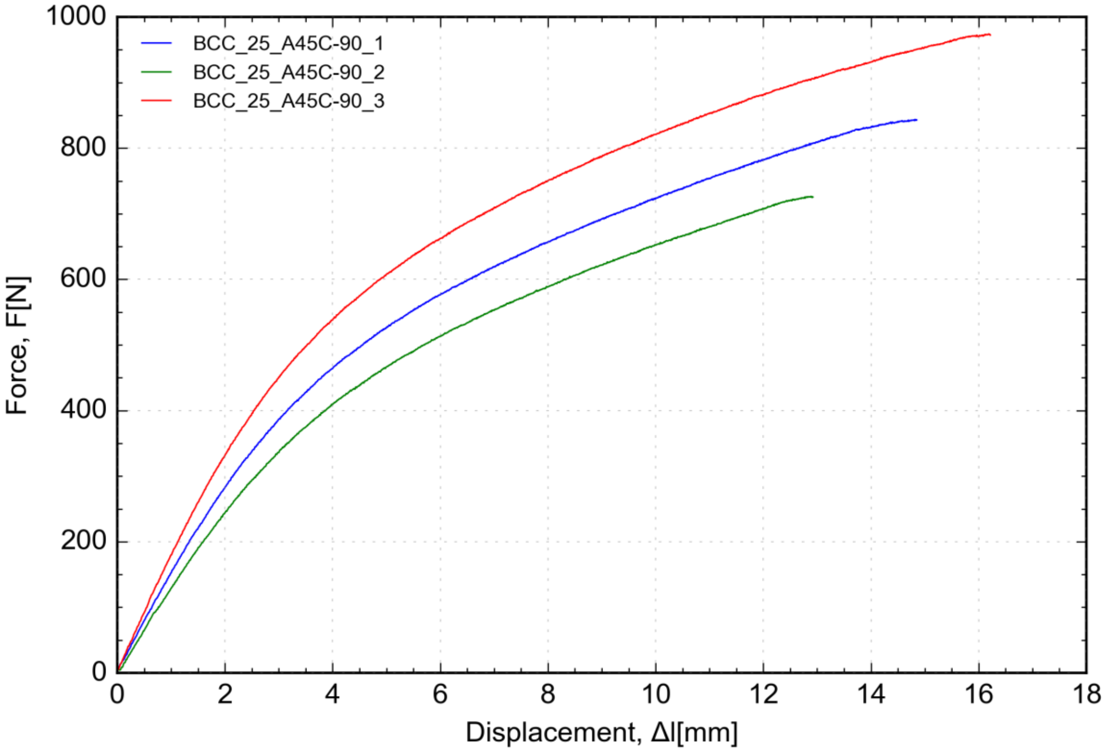

Source: Laboratory of prototype technologies and processes, 2019.

Figure C18 - Force-displacement curves for BCC 25% B90° specimens.

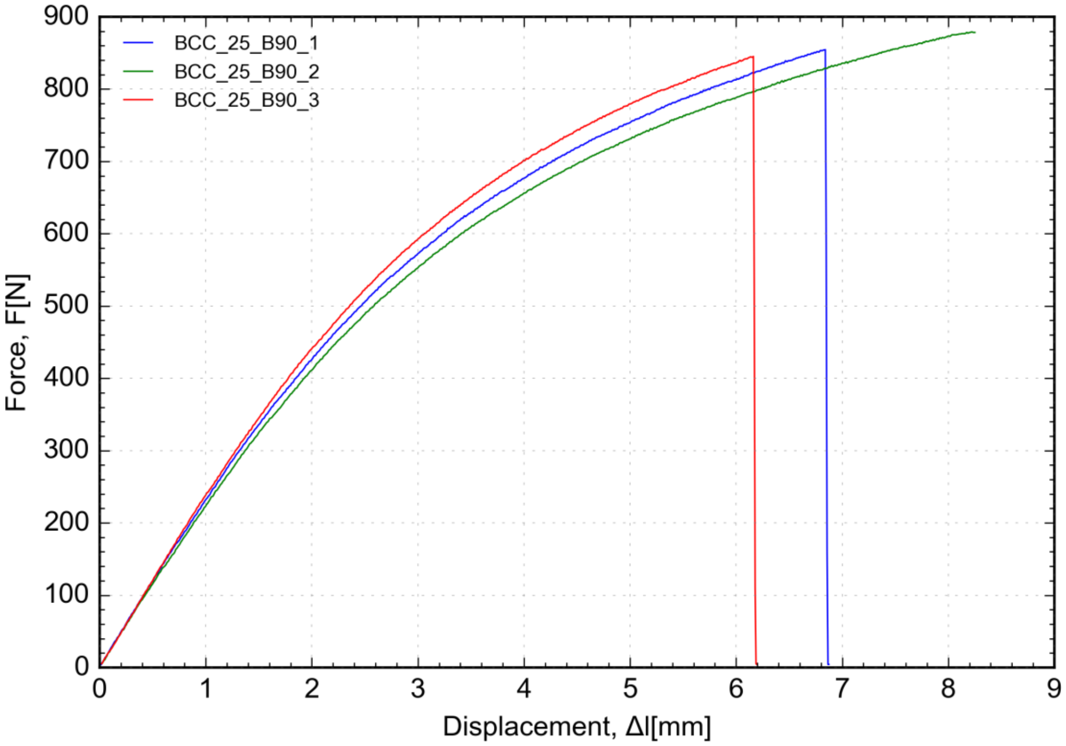

Source: Laboratory of prototype technologies and processes, 2019.

Figure C19 - Force-displacement curves for BCC 50% A0° specimens.

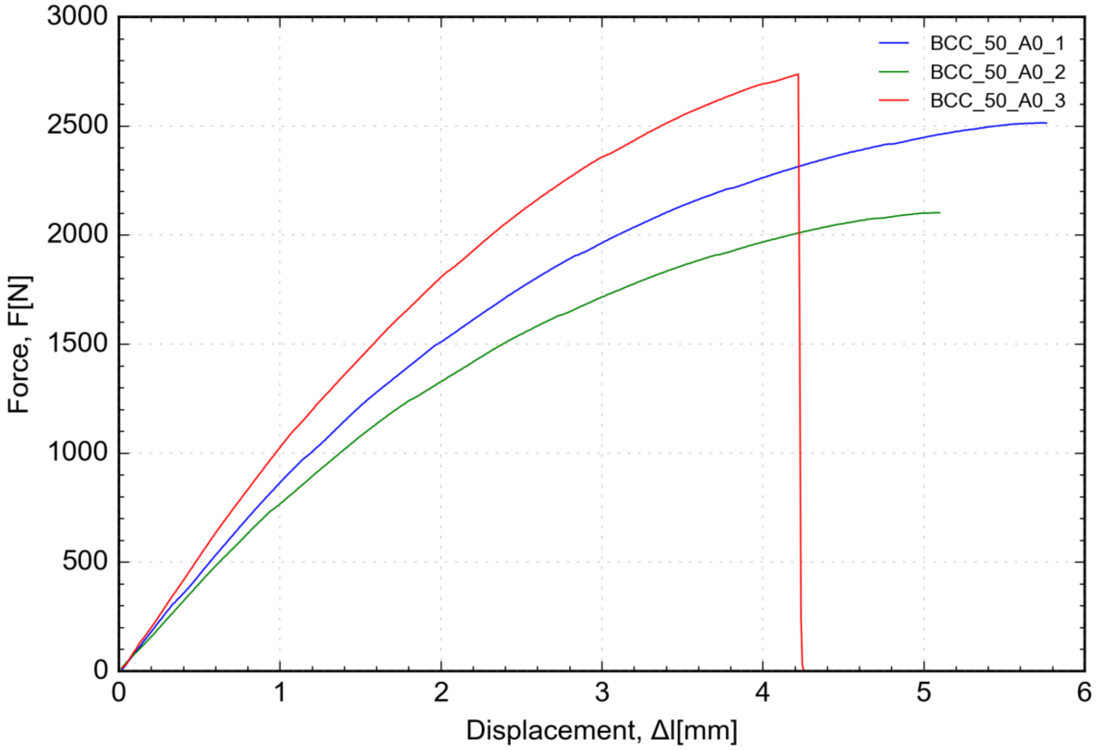

Source: Laboratory of prototype technologies and processes, 2019.

Figure C20 - Force-displacement curves for BCC 50% A45°C-90° specimens.

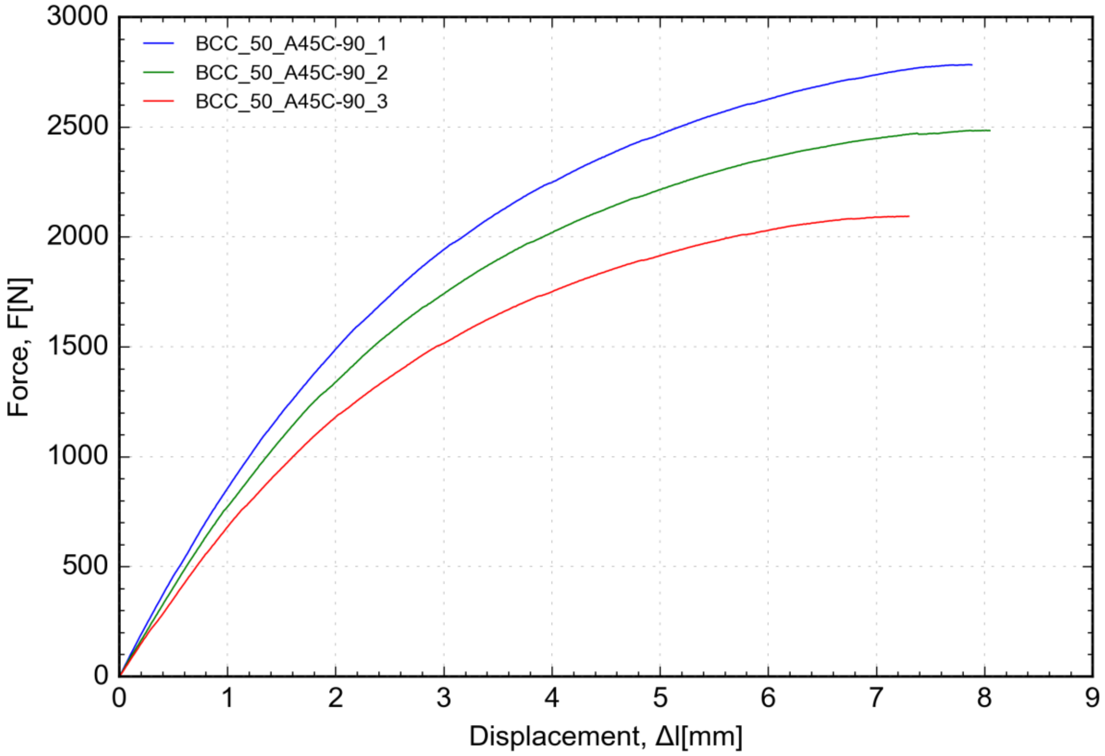

Source: Laboratory of prototype technologies and processes, 2019.

Figure C21 - Force-displacement curves for BCC 50% B90° specimens.

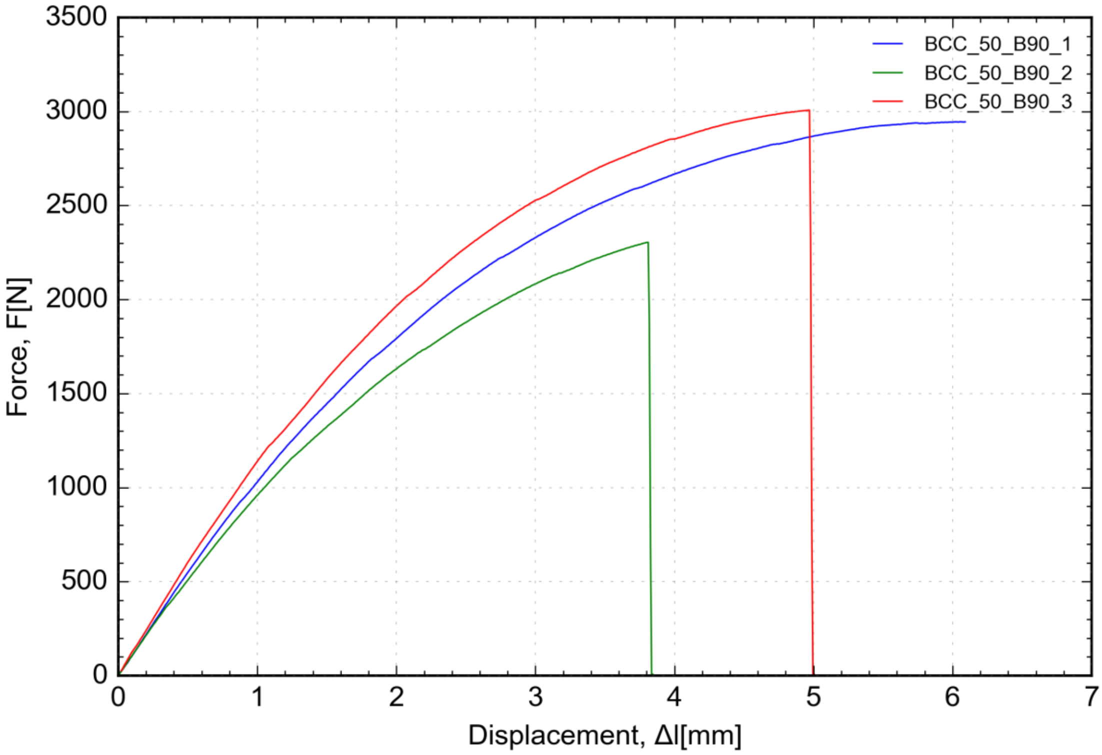

Source: Laboratory of prototype technologies and processes, 2019.

Figure C22 - Force-displacement curves for BCC 70% A0° specimens.

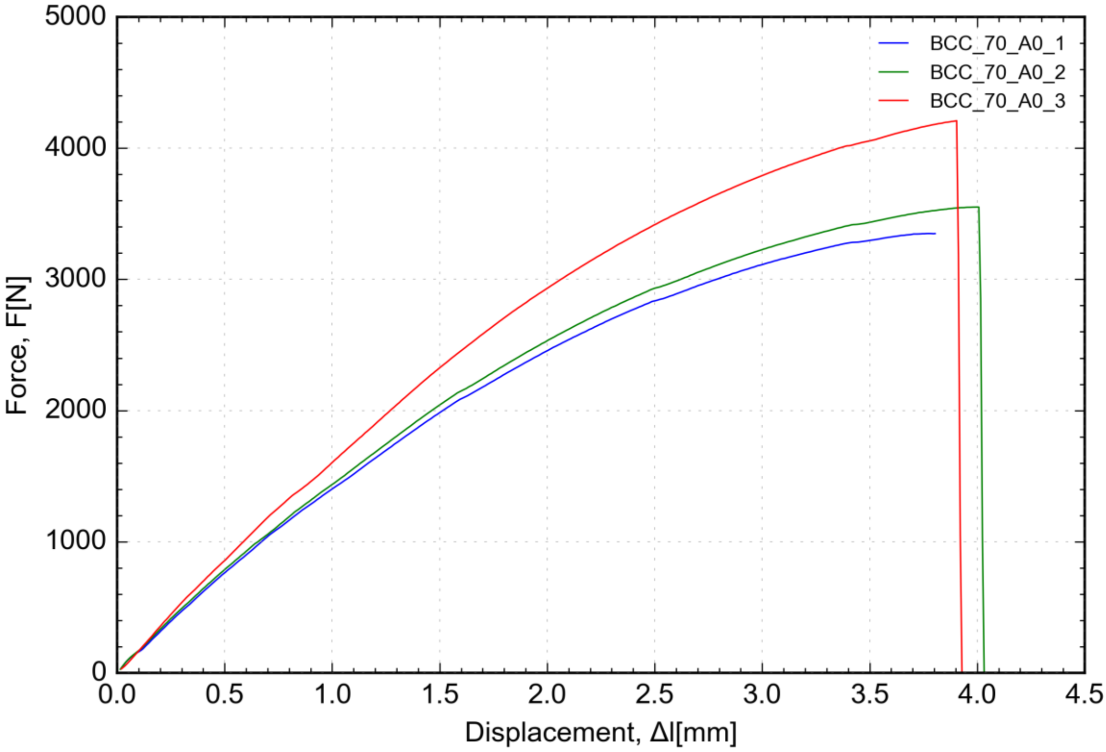

Source: Laboratory of prototype technologies and processes, 2019.

Figure C23 - Force-displacement curves for BCC 70% A45°C-90° specimens.

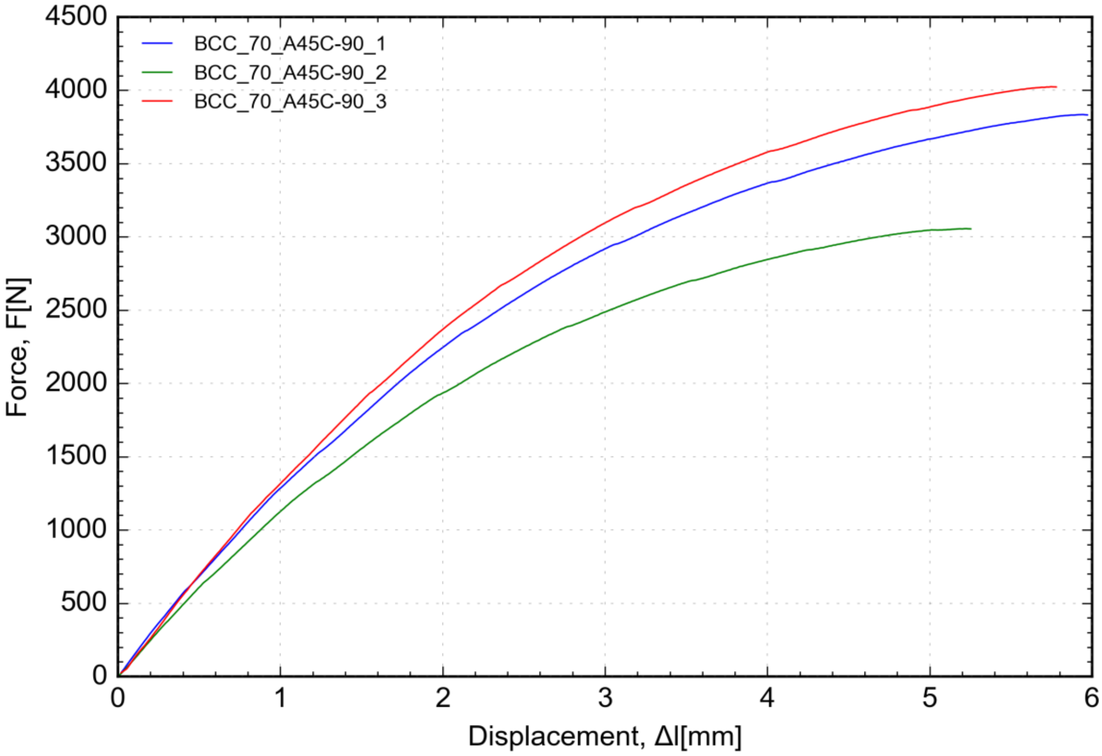

Source: Laboratory of prototype technologies and processes, 2019.

Figure C23 - Force-displacement curves for BCC 70% B90° specimens.

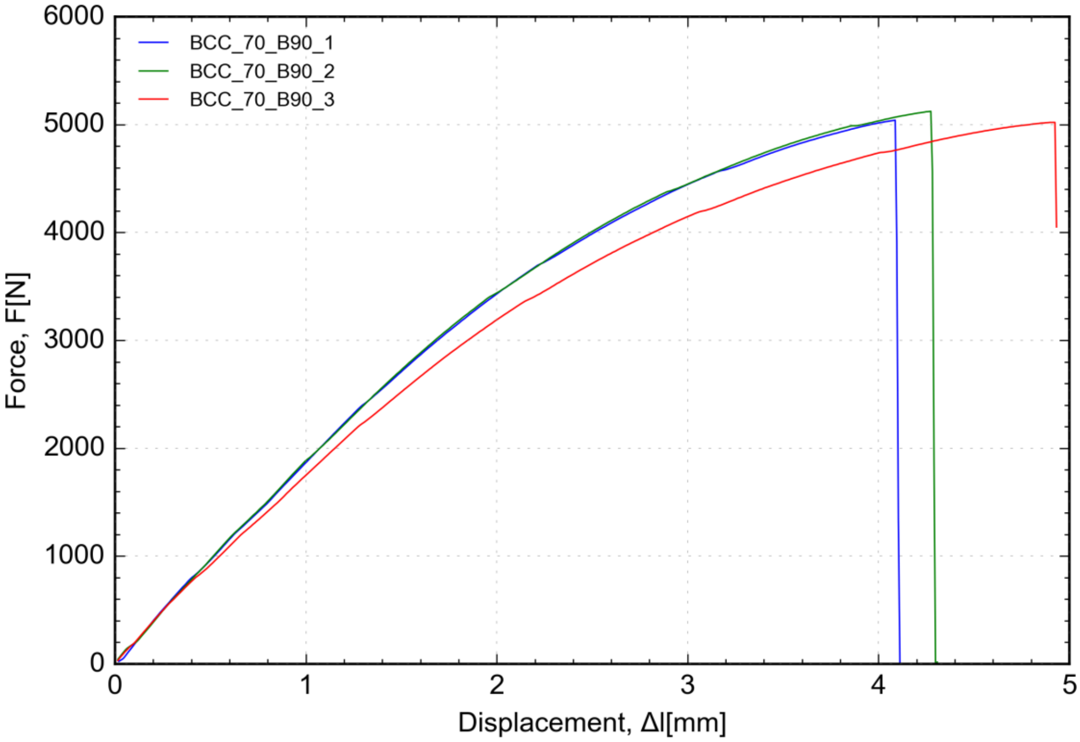

Source: Laboratory of prototype technologies and processes, 2019.

Figure C24 - Force-displacement curves for Octet-truss 25% A0° specimens.

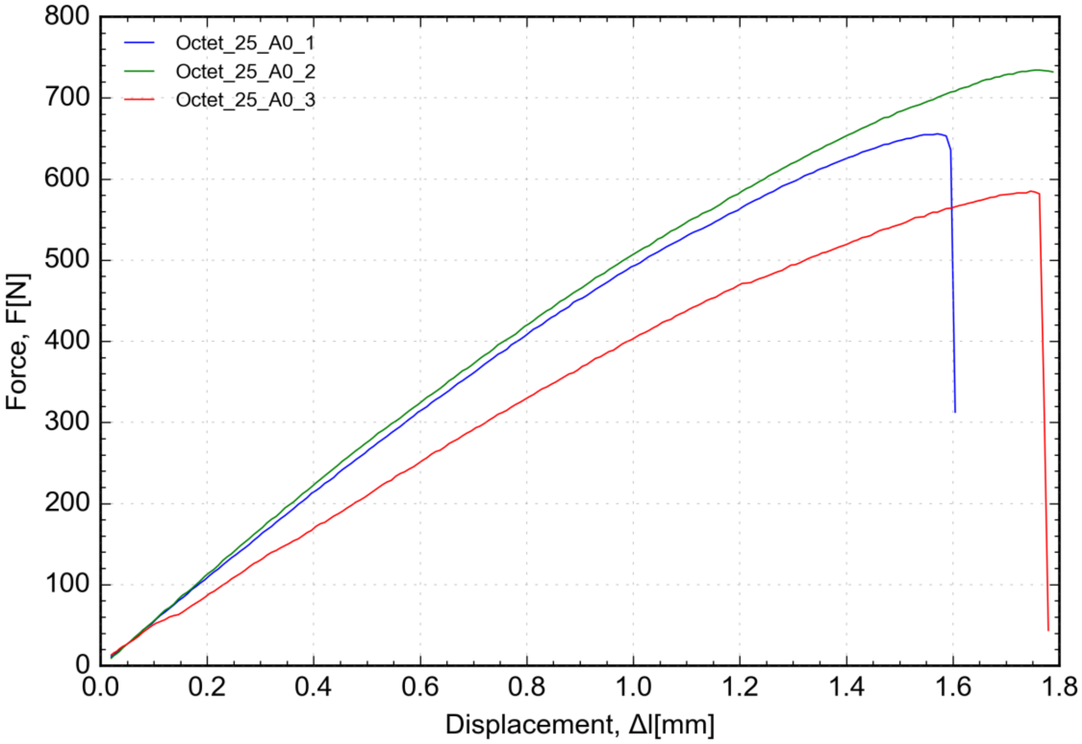

Source: Laboratory of prototype technologies and processes, 2019.

Figure C25 - Force-displacement curves for Octet-truss 25% B45° specimens.

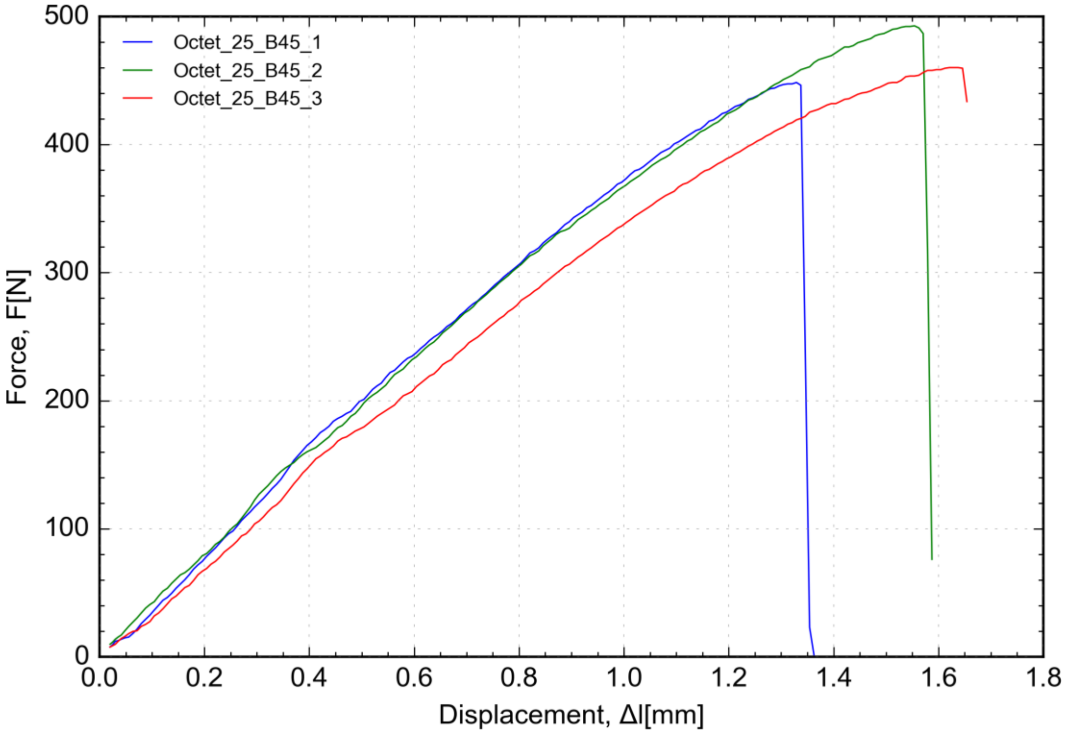

Source: Laboratory of prototype technologies and processes, 2019.

Figure C26 - Force-displacement curves for Octet-truss 50% A0° specimens.

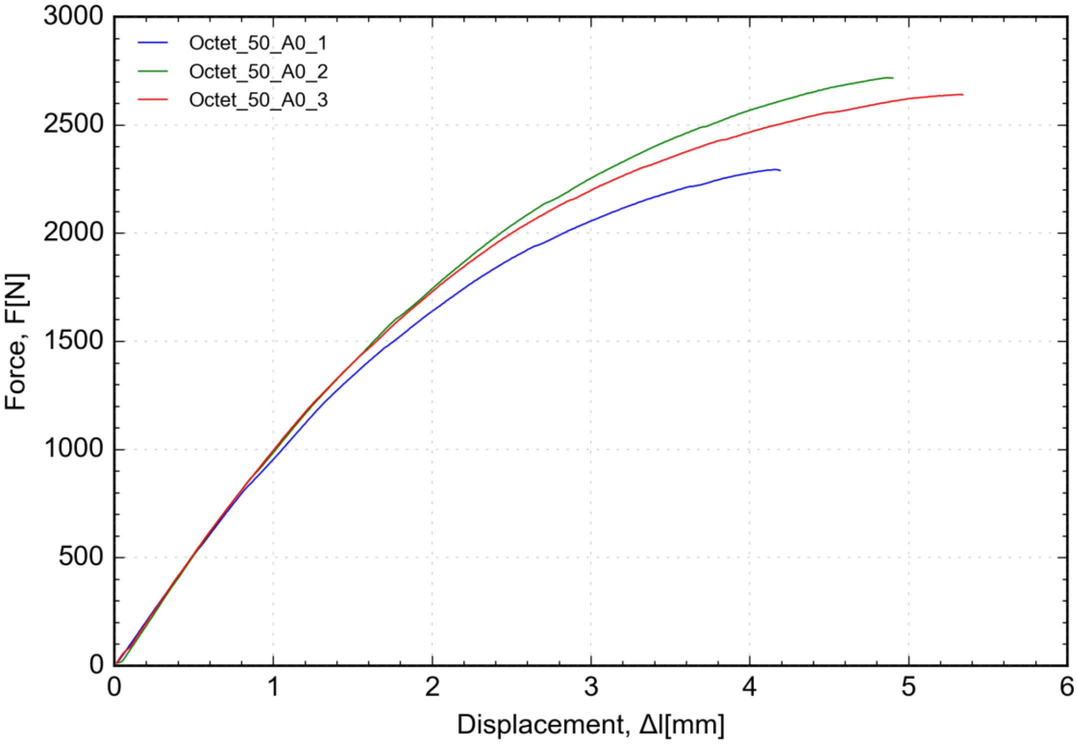

Source: Laboratory of prototype technologies and processes, 2019.

Figure C27 - Force-displacement curves for Octet-truss 50% B45° specimens.

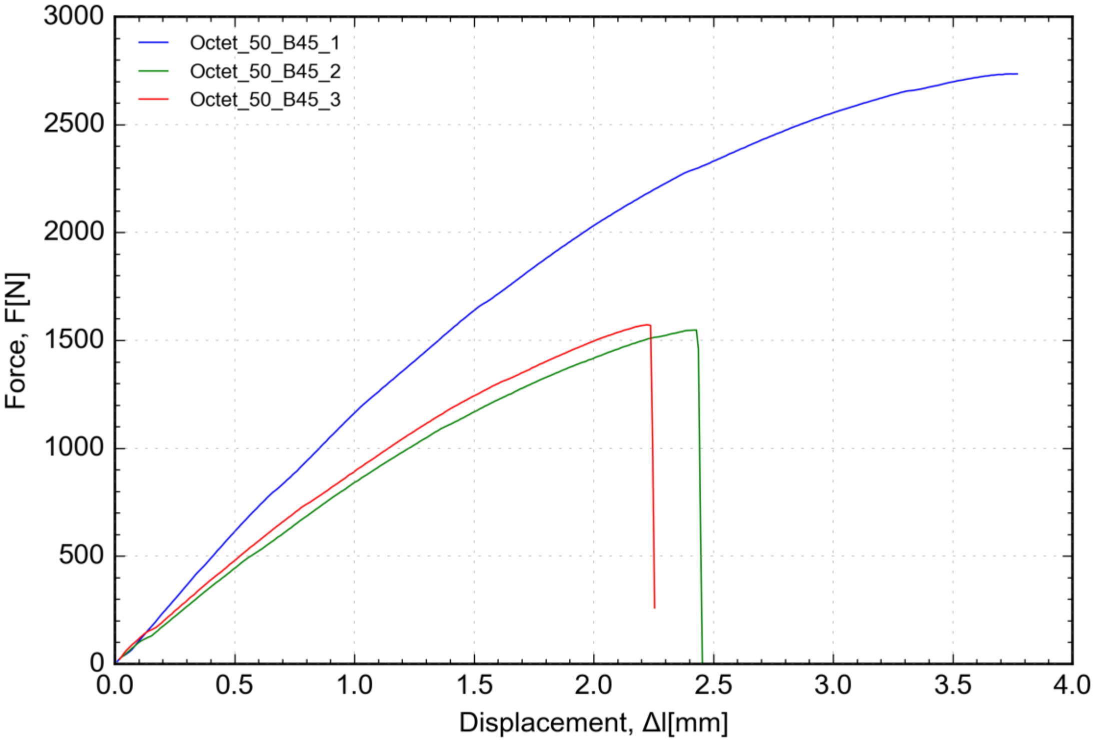

Source: Laboratory of prototype technologies and processes, 2019.